



Terms and Conditions of Use of Digitised Theses from Trinity College Library Dublin

Copyright statement

All material supplied by Trinity College Library is protected by copyright (under the Copyright and Related Rights Act, 2000 as amended) and other relevant Intellectual Property Rights. By accessing and using a Digitised Thesis from Trinity College Library you acknowledge that all Intellectual Property Rights in any Works supplied are the sole and exclusive property of the copyright and/or other IPR holder. Specific copyright holders may not be explicitly identified. Use of materials from other sources within a thesis should not be construed as a claim over them.

A non-exclusive, non-transferable licence is hereby granted to those using or reproducing, in whole or in part, the material for valid purposes, providing the copyright owners are acknowledged using the normal conventions. Where specific permission to use material is required, this is identified and such permission must be sought from the copyright holder or agency cited.

Liability statement

By using a Digitised Thesis, I accept that Trinity College Dublin bears no legal responsibility for the accuracy, legality or comprehensiveness of materials contained within the thesis, and that Trinity College Dublin accepts no liability for indirect, consequential, or incidental, damages or losses arising from use of the thesis for whatever reason. Information located in a thesis may be subject to specific use constraints, details of which may not be explicitly described. It is the responsibility of potential and actual users to be aware of such constraints and to abide by them. By making use of material from a digitised thesis, you accept these copyright and disclaimer provisions. Where it is brought to the attention of Trinity College Library that there may be a breach of copyright or other restraint, it is the policy to withdraw or take down access to a thesis while the issue is being resolved.

Access Agreement

By using a Digitised Thesis from Trinity College Library you are bound by the following Terms & Conditions. Please read them carefully.

I have read and I understand the following statement: All material supplied via a Digitised Thesis from Trinity College Library is protected by copyright and other intellectual property rights, and duplication or sale of all or part of any of a thesis is not permitted, except that material may be duplicated by you for your research use or for educational purposes in electronic or print form providing the copyright owners are acknowledged using the normal conventions. You must obtain permission for any other use. Electronic or print copies may not be offered, whether for sale or otherwise to anyone. This copy has been supplied on the understanding that it is copyright material and that no quotation from the thesis may be published without proper acknowledgement.

**STM study of the (001) and (110)
surfaces of magnetite**

A thesis submitted to the University of Dublin, Trinity College,
in application for the degree of Doctor in Philosophy

by

Sergio F. Ceballos

Physics Department
Trinity College Dublin

September 2004

ST. JOHN'S COLLEGE
DUBLIN

TRINITY COLLEGE
05 MAY 2005
LIBRARY DUBLIN

Thesis
7623

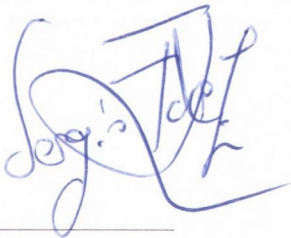
Declaration

This thesis is submitted by the undersigned for the degree of Doctor in Philosophy at the University of Dublin.

It has not been submitted as an exercise for a degree at any other university.

Apart from the advice, assistance and joint effort mentioned in the acknowledgements and in the text, this thesis is entirely my own work.

I agree that the library may lend or copy this thesis freely on request.



Sergio F. Ceballos

September 2004

Acknowledgements

Firstly, I would like to thank my supervisor Prof. I.V. Shvets giving me the opportunity to work in the Nanomag Group for the last four years. He introduced me to the field of surface science, nanotechnology and Scanning Tunneling Microscopy, always providing excellent guidance during my studies. Without his support, encouragement, enthusiasm and determination, this work would not have been possible.

I would also like to thank other members of the group. Dr. Shane Murphy who has been extremely supportive and helpful since the first day we met. Thanks for introducing me to UHV techniques as well as STM probing, fabrication and characterisation. A special acknowledgement goes to Dr. Guido Mariotto from whom I learnt the difficult art of transferring tips and samples inside a UHV chamber. I would like to thank him not only for his patience and encouragement over the course of my Ph.D, but also for the endless squash games, which helped make the working days easier. Dr. Roman Kantor, Dmitry Kashanin and Vivian Williams for those laboratory moments during my first 2 years. Ken Jordan for all the long scientific discussions, "spanglish" corrections and travelling experiences to conferences. He is optimistic, encouraging and has always shown a positive attitude towards work over the last 3 years. Thanks to Guissepe Manai for his computer assistance and coffee breaks. Alex Cazacu "Camicazu" for the endless metaphysical conversations about love, beauty and life. Dr. Nikolai Berdunov who introduced me to magnetite (111) surface. Sumesh Sofin and Dr. Sunil Arora for the fabrication of magnetite thin films for my studies. Dr. Yang Zhou for her help on XRD MnNi characterization. Marie Kinsella for her effective work, support and advice on several occasions. Other members of the

group who have moved on other directions such as Dr. Maina Karsanova for the AGFM/VSM characterization of MnNi samples. Anselm Gademann who could fix anything computer related and William Signac for his friendship and dinner parties. I also have to mention other "extra-official" members such as Gregory Cabailh who shared with me the amazing story of the "funny" trick and the unforgettable trip through the "Valley of silence".

The group could not operated without the efforts and background support of other members of the Physics Department namely John Kelly, Mick Reilly, Ken Concannon, Joe McCauley, Pat Flanagan, James Kavanagh, Kevin Thompson and all the secretarial staff, Michelle Duffy, Susan Priest and Elaine O'Malley.

Thanks to my friends in Santander, Luis, Jose, David and specially Rafa for still being part of my life. Friends in Ireland, Marie for those lovely meals and "frustrating" clubbing nights we have shared together. Mr. McSweeney for being a good friend and letting me stay in his house for a cheap rent in "Sarajevo". Matt for mutual support in tough moments. Thanks to Ana who showed me Ireland 10 years ago. Special mention to Patrick Gaffney, for his his excellent friendship, exceptional advice and the good times during the thousand "nites" out in Dublin.

I would like to thank my family who have coped with me being away from them, always being patience, encouraging and understanding. Maria Jose, my Godmother, for all those "protective" times together in Madrid. Miguel Angel, my uncle, who always made me smile. Finally, I would like to dedicate this thesis to mum and dad for their constant loving care and support.

Abstract

In this thesis the surface of single crystals and thin films of magnetite (001) and (110) have been studied by scanning tunneling microscopy (STM), scanning tunneling spectroscopy (STS), Auger electron spectroscopy (AES) and low-energy electron diffraction (LEED). The use of STM tips made of magnetic materials is highlighted in this work. A novel technique has been developed by the author in order to provide STM tips made of paramagnetic, ferromagnetic and antiferromagnetic materials. Special emphasis has been placed on the study and characterization of tips made of antiferromagnetic MnNi alloy. Chemical and magnetic characterization has been performed by AES, X-ray diffraction (XRD), alternating gradient force magnetometer (AGFM) and transmission electron microscope (TEM). Scanning electron microscope (SEM) has also been employed for characterization of the tips. The potential of the MnNi tips for SP-STM measurements has been confirmed by STS/STM studies of Mn/Fe(001), a test sample whose magnetic properties are well known. These tips are routinely used by the group for SP-STM experiments on magnetite.

A detailed analysis of the nature and topography of contaminant free and contaminated magnetite (001) single crystals and thin films is given. It has been demonstrated how the surface topography of a contaminated and clean surface of magnetite (001) is intimately related to the preparation conditions, with the O/Fe ratio playing a crucial role in determining the surface terminations of magnetite.

The (001) plane of magnetite can be viewed as a stacking sequence of two alternating layers. The A-layer contains tetrahedrally coordinated Fe^{3+} ions, while the B-layer is composed of octahedrally coordinated Fe^{2+} and Fe^{3+}

ions surrounded by oxygen ions. A $(\sqrt{2} \times \sqrt{2})R45^\circ$ surface reconstruction has been observed on a clean magnetite (001) surface. A high exposure of the surface to oxygen during preparation leads to an octahedral terminated surface. On the other hand, the light exposure of the surface to a hydrogen atmosphere leads to a co-existence of tetrahedral and octahedral terminated surfaces. A combined tetrahedral and octahedral termination has been rarely observed in the past.

Continuous annealing of the single crystals and magnetite thin films leads to a contaminated (001) magnetite surface. The typical contaminants found were calcium and potassium. Self assembled patterns of rows and nanotrenches on the surface are observed and explained in terms of the formation of a $\text{Ca}_{1-x}\text{Fe}_{2+x}\text{O}_4$ -like and $\text{Mg}_{1-x}\text{Fe}_{2+x}\text{O}_4$ -like phases. A range of different surface reconstructions have been observed with increase of the annealing time, related to a variation of the local [O/Fe] stoichiometry ratio at the surface and the concentration of contaminants. $p(1 \times 1)$, $p(1 \times 2)$, $p(1 \times 3)$ and $p(1 \times 4)$ superlattices have been found on the Fe_3O_4 (001) surface.

Finally, the non-polar surface of a single crystal and thin film of magnetite (110) has also been investigated. Nanostructures have been observed on the surface when annealing the crystal and thin film at a temperature of 1100 ± 50 K. Despite the fact that the surface is non-polar, under certain preparation conditions a (1×3) surface reconstruction is observed. It has been attributed to the change of [O/Fe] stoichiometry ratio and the presence of Ca and Mg at the surface.

Publications

1. Journals

C. Daul, S. Fernandez-Ceballos, I. Ciofini, C. Rauzy and C. Schlapfer. "A novel Density Functional Study of the Ground State Properties of a Localized Trinuclear Copper (II,II,III) Mixed-Valence System". *Chem. Eur. J.*, 4392-4401 8 19 (2002)

S. F. Ceballos, G. Mariotto, S. Murphy, I.V. Shvets. "Fabrication of magnetic STM probes and their application to studies of the Fe_3O_4 (001) surface". *Surf. Sci.*, 131-140 523 (2003)

G. Mariotto, S. F. Ceballos, S. Murphy, and I. Shvets. "Scanning Tunneling microscopy studies of the Fe_3O_4 (001) surface using antiferromagnetic probes". *J. Appl. Phys.*, 93 10 (2003)

S.F. Ceballos., G. Mariotto, K. Jordan, S. Murphy and I. Shvets. "An atomic scale study of the Fe_3O_4 (001) surface". *Surf. Sci.*, 548 106-116 (2004)

G. Mariotto, S. F. Ceballos, S. Murphy and I. Shvets. "Alkaline and alkaline-earth metals self-assembled nano-patterns on the Fe_3O_4 (001) surface". *Phys. Rev. B* 70, 035417 (2004)

G. Mariotto, S. Murphy, N. Berdunov, S. F. Ceballos and I. Shvets. "Influence of Ca and K on the reconstruction of Fe_3O_4 (001) surface". *Surf. Sci.* 564 79-86 (2004)

K. Jordan, G. Mariotto, S. F. Ceballos, S. Murphy and I. Shvets. "Spin Polarised scanning tunneling microscopy of Fe_3O_4 (001) charged ordered surface". *Submitted: Surf. Sci.*, Aug (2004)

K. Jordan, G. Mariotto, S. F. Ceballos, S. Murphy and I. Shvets. "Atomic scale SPSTM imaging of the Fe_3O_4 (001) surface using antiferromagnetic tips". *Accepted: J. Mag. Mag. Mat.*, Sep (2004)

S. Murphy, S. F. Ceballos, G. Mariotto, N. Berdunov, K. Jordan, and I. Shvets. "Atomic scale spin-dependent scanning tunneling microscopy using antiferromagnetic STM tips". *In press: J. Microsc. R. Tech.*, Sep (2004)

S.F. Ceballos, K. Jordan, G. Mariotto, N. Berdunov, S. Murphy and I.V. Shvets. "Surface studies of magnetite (110)". *In preparation*

2. Conference Proceedings

S. F. Ceballos, K. Jordan, S. Murphy, C. Seoighe, and I. V. Shvets. "Contaminants Induced Onset of Nanostripes and Nanotrenches on the Fe_3O_4 (001) Surface". *AIP Conf. Proc.*, 696, 879 (2003)

G. Mariotto, K. Jordan, S. F. Ceballos, S. Murphy, C. Seoighe, and I. V. Shvets. "Charge Ordering on the $(\sqrt{2} \times \sqrt{2})R45^\circ$ Reconstructed Fe_3O_4 (001) Surface". *AIP Conf. Proc.*, 696, 873 (2003)

N. Berdunov, G. Mariotto, S. Murphy, S. F. Ceballos, K. Jordan, and I.

V. Shvets. "Polaronic Superlattice Formed on Oxidised Magnetite (111) Surface". *AIP Conf. Proc.*, 696, 865 (2003)

S. F. Ceballos, G. Mariotto, N. Berdunov, S. Murphy, K. Jordan, and I. V. Shvets. "Fabrication of Magnetic Probes for Spin-Polarized STM Studies of the Fe_3O_4 (001) and (111) Surfaces" *AIP Conf. Proc.*, 696, 298 (2003)

S.F. Ceballos, N. Berdunov, G. Mariotto, S. Murphy and I.V. Shvets. "Spin-Polarised tunnelling effects observed on the magnetite (001) and (111) surfaces". *NMMA 03*, Kluwer Academic Publishers, NATO Science Series. Nov 03

List of abbreviations

1D - one dimensional

2D - two dimensional

3D - three dimensional

AES - Auger electron spectroscopy

AGFM - Alternating gradient force magnetometer

CMA - cylindrical mirror analyser

DLA - diffusion limited aggregation

DOS - density of states

e-beam - electron beam

ECG - electrostatic centre of gravity

HT - high-temperature

L - Langmuir

LBL - layer-by-layer

LDOS - local density of states

LEED - low energy electron diffraction

LT - low-temperature

LTSTM - low-temperature scanning tunneling microscopy

MBE - molecular beam epitaxy

ML - monolayer

RT - room temperature

RTSTM - room-temperature scanning tunneling microscopy

SPM - scanning probe microscopy

SPSTM - spin polarised scanning tunneling microscopy

STM - scanning tunneling microscopy

STS - scanning tunneling spectroscopy

TEM - transmission electron microscope

TMR - tunneling magneto resistance

TPD - temperature programmed desorption

TSP - titanium sublimation pump

UHV - ultra high vacuum

XRD - x-ray diffraction

List of Figures

2.1	Schematic diagram of the process of Auger emission in a solid	5
2.2	Schematic representation of a STM tunneling junction	8
2.3	The multidisciplinary nature of iron oxide research	15
2.4	Phase diagram for the Fe – O system.	17
2.5	Unit cell of Fe_3O_4	18
2.6	The (001) <i>B</i> -terminated surface of Fe_3O_4	20
2.7	The (001) <i>A</i> -terminated surface of Fe_3O_4	21
2.8	Fe_3O_4 (110) <i>A</i> and <i>B</i> terminated surface	22
2.9	Representation of the charge neutrality of magnetite (001) . .	25
3.1	Top view of the UHV system	32
3.2	Schematic of the resistive heater	35
3.3	Schematic illustration of the e-beam heater	36
3.4	Schematic illustration of a STM head	40
3.5	Schematic of four-grid optics in LEED mode	42
3.6	Schematic of LEED screen geometry	43
4.1	electrochemical set up	47
4.2	etching process	48
4.3	MnNi structure and magnetic order	51
4.4	X-ray diffraction spectrum	52

4.5	MnNi SEM images	54
4.6	General magnetic behaviour for magnetic materials	56
4.7	magnetisation versus external magnetic field for a MnNi sam- ple(etched/not etched)	57
4.8	X-ray diffraction spectra comparison	59
4.9	AES analysis of a MnNi sample 1	62
4.10	AES analysis of a MnNi sample 2	63
4.11	Magnetic contrast with a MnNi probe	67
4.12	magnetisation orientation schematic for Fe/W and MnNi tips .	68
4.13	SEM image of a Cr tip	71
4.14	SEM image of a Ni tip	72
4.15	SEM image of a $\text{Fe}_3\text{O}_4(001)$ surface taken with a MnNi tip . .	73
5.1	AES and LEED of a clean $\text{Fe}_3\text{O}_4(001)$ surface	79
5.2	STM image, B-termination surface	80
5.3	STM image, B-termination surface, Zoom-in	81
5.4	STM image, A- B- coexisting terminations	84
5.5	STM image, Zoom-in on A-terminations	85
6.1	Surface reconstructions on magnetite (001) surface	92
6.2	AES spectrum of low level of contaminants Fe_3O_4 (001) surface	93
6.3	Onset of formation of trenches	94
6.4	Onset of formation of trenches. Zoom-in	96
6.5	The onset of formation of p (1×3) superlattice by contaminants	97
6.6	AES/LEED for a contaminated magnetite (001) surface	99
6.7	Different surface rearrangements on the surface	100
6.8	p(1×2) surface reconstruction.	102
6.9	p(1×2) schematic model	103

6.10	AES and LEED for a $p(1 \times 3)$ surface reconstruction	106
6.11	$p(1 \times 3)$ STM surface reconstruction.	107
6.12	$p(1 \times 3)$ STM surface reconstruction. Zoom-in	108
6.13	$p(1 \times 3)$ schematic model	109
6.14	LEED pattern for a $p(1 \times 4)$ surface reconstruction	111
6.15	STM image, $p(1 \times 4)$ surface reconstruction	113
6.16	Models proposed for a $p(1 \times 4)$ surface reconstruction	115
6.17	STM image of Fe_3O_4 thin film annealed at low temperature.	118
6.18	AES data for a 70 nm contaminated magnetite thin film	119
6.19	STM image for rounded terrace formation	120
6.20	I/V curves for a contaminated magnetite 70 nm thin film	121
6.21	STM image of a $p(1 \times 1)$ reconstruction	122
7.1	LEED pattern for magnetite (110)	127
7.2	LEED pattern of a magnetite (110) surface with fractional order spots	129
7.3	STM image of a magnetite (110) terraced surface	130
7.4	STM image of a magnetite (110) nanostructured surface	131
7.5	STM image of a magnetite thin film (110)	133
7.6	Ball model for magnetite (110) nanostructures	135
7.7	I/V curves for magnetite (110) surface	137
A.1	AES spectrum for a $p(1 \times 3)$ surface reconstruction	145
B.1	Lattice parameters calculation of a $p(1 \times 3)$ LEED pattern	149
C.1	Classification of surfaces according to Tasker	151
C.2	Representation of a crystalline compound cut along a polar direction	151

List of Tables

2.1	Properties of iron oxides	16
6.1	The ionic radii	91

Contents

1	Introduction	1
2	Background	4
2.1	Introduction to experimental techniques	4
2.1.1	Auger Electron Spectroscopy (AES)	4
2.1.2	Scanning Tunneling Microscopy (STM)	6
2.1.3	Scanning tunneling spectroscopy (STS)	10
2.1.4	Low Energy Electron Diffraction (LEED)	12
2.2	Magnetite: Fe ₃ O ₄	14
2.2.1	Introduction	14
2.2.2	The surface of Fe ₃ O ₄ (001)	19
2.2.3	The surface of magnetite (110)	19
2.2.4	Autocompensated surfaces	23
2.2.5	Literature review	26
3	Experimental details	31
3.1	The ultrahigh vacuum set up	31
3.2	The preparation chamber	33
3.2.1	The resistive heater	34
3.2.2	The e-beam heater	36

3.2.3	The ion gun	37
3.2.4	Sample Characterization: Auger Electron Spectroscopy	38
3.3	The room-temperature STM	39
3.3.1	Four-grid LEED	41
4	STM tips	44
4.1	Introduction	44
4.2	Tip fabrication procedure	46
4.3	MnNi tips	50
4.3.1	MnNi alloy	50
4.3.2	Tip preparation	50
4.3.3	MnNi tips characterization	53
4.3.4	Magnetic contrast: Scanning tunneling spectroscopy (STS)	64
4.4	Cr tips	69
4.5	Other tips	70
4.6	STM results on magnetite (001) taken with a MnNi tip	70
4.7	Conclusions	74
5	The Clean Fe₃O₄ (001) surface	76
5.1	Introduction	76
5.2	Sample preparation	77
5.3	Surface preparation	77
5.4	STM results and discussion	78
5.4.1	B- termination surface	78
5.4.2	Co-existing A- and B- terminations	82
5.5	Conclusions	87

6	The Contaminated Fe₃O₄(001) surface	88
6.1	Introduction	88
6.2	Sample preparation	89
6.3	Contaminated Fe ₃ O ₄ (001) surface	90
6.3.1	Breaking of long range ($\sqrt{2} \times \sqrt{2}$)R45° order by the presence of contaminants	93
6.3.2	p(1 × 2) reconstruction	98
6.3.3	p(1 × 3) reconstruction	104
6.3.4	p(1 × 4) surface reconstruction	110
6.4	p(1 × 1)	122
6.5	Conclusions	123
7	Surface studies of Fe₃O₄ (110)	125
7.1	Introduction	125
7.2	Sample preparation	126
7.3	Results and discussion	126
7.3.1	Formation of nanostructures	126
7.3.2	Discussion	132
7.4	Conclusions	138
8	Summary	139
8.1	Conclusions	139
8.2	Further work	141
8.2.1	Further characterisation of MnNi probes	141
8.2.2	Further characterisation of Fe ₃ O ₄	142
A	AES calculations	144
B	LEED calculations	147

CONTENTS

XVIII

C Polar and non-polar surfaces

150

Chapter 1

Introduction

Metal-oxide surfaces have recently drawn increasing attention due to their important technological applications, *i.e.* corrosion, catalysis and microelectronics. Iron oxides have also attracted much interest, in particular Fe_3O_4 , commonly known as magnetite, as it is predicted to be half a metallic ferromagnet [1].

Fe_3O_4 (001) and (110) artificial and natural single crystal and thin film surfaces are the focus of the study presented here. Magnetite is one of the few oxides with very high, almost metallic conductivity, which is due to Fe ions of different valence states being located at identical crystallographic positions. At room temperature, the electrical conductivity of Fe_3O_4 is about $200 \Omega^{-1} \text{cm}^{-1}$ [2]. Magnetite is also predicted to be a half-metallic ferrimagnet [1, 3], meaning that in the spin-up sub-band it is a metal and in the spin-down sub-band it is an insulator. At a temperature of 120 K bulk magnetite exhibits a metal-insulator transition, known as the Verwey transition [2, 4], at which its conductivity decreases by two orders of magnitude [5, 6]. The change of conductivity is accompanied by a change in its crystallographic structure, whose symmetry is lowered from cubic to monoclinic. The surfaces

of magnetite show a highly complex behavior which is due to many factors such as, the stoichiometry; i.e. the ratio of the Fe to O ions on the top most layer [7–9].

A detailed investigation of probes made of magnetic materials for Scanning Tunneling Microscope (STM) and Spin polarised STM (SP-STM) application is performed in this study. Aspects such as fabrication, geometry and composition are studied. A reproducible technique for the fabrication of STM tips from a range of magnetic materials has been developed. The tips are formed by electrochemical etching in an aqueous solution (NaOH, HCl), using polymer tubing to physically restrict the active etching region. Tips, with apexes in the 50-100 nm range, have been produced from polycrystalline MnNi, Cr, Fe and Ni. Atomic resolution STM images have been achieved on the Fe_3O_4 (001) surface, using MnNi tips.

The preparation procedure of the surface of magnetite (001) to obtain a contaminant-free surface is studied in detail, with a view towards spin-polarised measurements. Due to the continuous presence of contaminants on the surface of the single crystals of magnetite (001) studied, the SP-STM project was not fully pursued; the contaminated magnetite surface was investigated instead. Contaminants such as Ca and K are commonly present in natural and artificial magnetite single crystals. They diffuse from the bulk to the surface when preparing the crystal due to an extensive annealing. From a fundamental research point of view contaminants on the surface of magnetite are not highly interesting, but their potential within the area of nanoscale self-assembly is discussed. The surfaces of magnetite (001) and (110) are studied by STM, STS, AES and LEED. A series of $(\sqrt{2} \times \sqrt{2})R45^\circ$, $p(1 \times 1)$, $p(1 \times 2)$, $p(1 \times 3)$ and $p(1 \times 4)$ surface reconstructions have been observed on the surface of magnetite (001) with increasing concentrations of

Ca and K. A detailed investigation of the self-assembly of impurities onto the surface is given at a nano- and atomic- scale on both surfaces.

The results obtained by the author in this study are a contribution to the characterisation of magnetic probes suitable for SP-STM studies and to the nanoscale self-assembly of nanostructures by controlled diffusion of contaminants onto the surface.

Chapter 2

Background

2.1 Introduction to experimental techniques

2.1.1 Auger Electron Spectroscopy (AES)

Auger Electron Spectroscopy (AES) represents one of the most important chemical surface analysis tools for conducting samples. The method is based on the excitation of so-called "Auger electrons". AES is based on the use of primary electrons with typical energies between 3 and 30 keV and the possibility to focus and scan the primary electron beam in the nanometer and micrometer range analyzing the top-most atomic layers of matter. Figure 2.1 shows the sequence of events following ionisation of a core level. For this example the K level is shown as being ionised by an incident electron, whose energy E_p must obviously be greater than the binding energy E_K of an electron in K. Following the creation of a hole in the level K, the atom relaxes by filling the hole via a transition from an outer level, in this example shown as L_1 . As a result of that transition the energy difference ($E_K - E_{L_1}$) becomes available as excess energy, and this excess energy can be used by

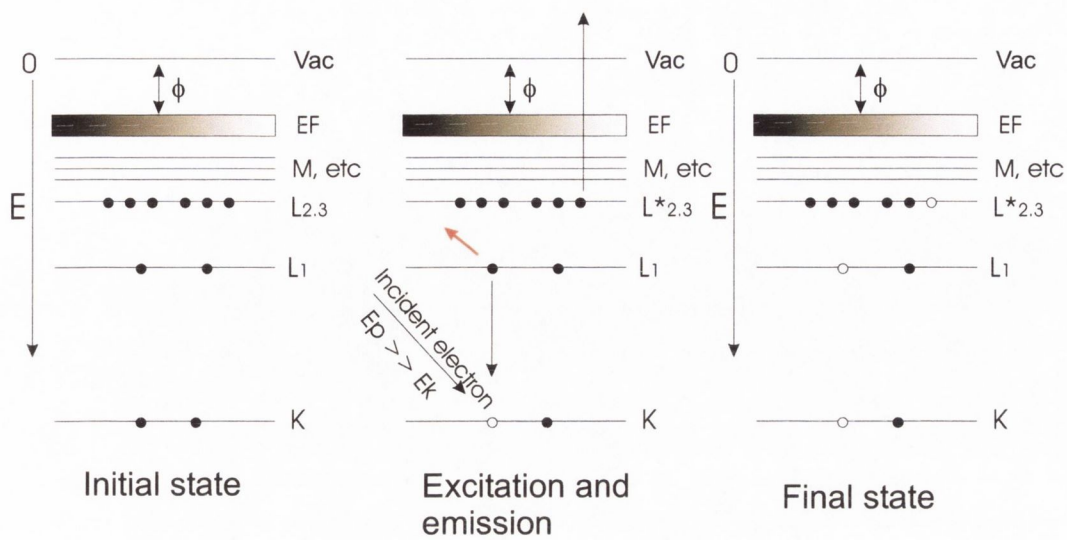


Figure 2.1: The ground state is shown on the left. In the center an incident electron of energy E_p has created a hole in the core level K by ionisation. The hole in the K shell is filled by an electron from L_1 , releasing an amount of energy ($E_K - E_{L1}$), which can appear as a photon or can be given up to another electron. The double ionised final state is shown on the right. Reproduced from [10].

the atom in either of two ways.

It can appear as a characteristic X-ray photon at that energy or it can be given to another electron either in the same level or in a more shallow level, whereupon the second electron is ejected. The first process is that of X-ray fluorescence and the second that of Auger emission. The Auger transition depicted in figure 2.1 would be named as $KL_1L_{2,3}$. The electrons taking part in the Auger process might also originate in the valence band of the solid, in which case the convention writes the transitions as, for example $KL_{2,3}V$ if one electron comes from the valence band and, for example, KVV if both do. The emitted Auger electrons are part of the secondary energy electron spectrum

obtained under electron bombardment with a characteristic energy allowing one to identify the emitting elements. Auger electrons render information essentially on the elemental composition of the first 2-10 atomic layers [11].

2.1.2 Scanning Tunneling Microscopy (STM)

Comprehensive reviews of the theory and operating principles of scanning tunneling microscopy (STM) and spectroscopy (STS) are given in dedicated texts by Chen and Wiesendanger [12, 13]. The fundamental theory of STM is modelled on the quantum-mechanical description of an electron with energy E travelling in a 1D potential $U(z)$ of the form shown in figure 2.2(a). This electron is described by a wavefunction $\psi(z)$, which satisfies the Schrödinger equation:

$$-\frac{\hbar^2}{2m} \frac{d^2}{dz^2} \psi(z) + U(z)\psi(z) = E\psi(z) \quad (2.1)$$

where m is the electron mass and $\hbar = h/2\pi$ (where h is Planck's constant). In the classically allowed region where $E > U(z)$, this equation has solutions of the form:

$$\psi(z) = \psi(0)e^{\pm ikz}, \quad k = \frac{\sqrt{2m(E - U)}}{\hbar} \quad (2.2)$$

where the electron can move in either the positive or negative direction. In the classically forbidden *barrier* region where $E < U(z)$, the Schrödinger equation has the solution:

$$\psi(z) = \psi(0)e^{-\kappa z}, \quad \kappa = \frac{\sqrt{2m(U - E)}}{\hbar} \quad (2.3)$$

The κ term describes the decay of the electron wavefunction within the barrier region. For a finite potential $U(z)$, there is a non-zero probability P of finding the electron at a position z inside the barrier region, which is given by:

$$P \propto |\psi(0)|^2 e^{-2\kappa z} \quad (2.4)$$

Consequently, if the width of the tunnel barrier is sufficiently narrow, there is a finite probability that the electron can tunnel through the barrier region.

In the tip-vacuum-sample configuration of an STM junction (figure 2.2(b)), the height of the tunnel barrier is determined by the *work function* ϕ of the tip and sample (assumed to be identical for convenience), which is the minimum energy required to remove an electron from the metal to vacuum. An electron at the tip or sample surface, with Fermi energy $E_F = -\phi$ eV, will have the greatest opportunity to tunnel through the barrier, since by definition the *Fermi level* denotes the upper limit of electron occupancy in the metal. In the absence of an externally applied bias, the electron can tunnel through the barrier in either direction so that there is no net tunnel current. By applying an external voltage V , electrons in the sample within the energy range $E_F - eV \leq E \leq E_F$ have an opportunity to tunnel through the barrier. If $eV \ll \phi$, then only electron states very near to the Fermi level are probed. The probability for an electron in the n th states to tunnel through a barrier of width W is given by:

$$P \propto |\psi_n(0)|^2 e^{-2\kappa W}, \quad \kappa = \frac{\sqrt{2m\phi}}{\hbar} \quad (2.5)$$

Taking all the possible states in the energy range $E_F - eV \leq E \leq E_F$ into account, the tunnel current is:

$$I_t \propto \sum_{E=E_F-eV}^{E_F} |\psi(0)|^2 e^{-2\kappa W} \quad (2.6)$$

If V is small enough that the density of electronic states does not vary significantly within it, the latter sum can be conveniently written in terms of the *local density of states* (LDOS). At the Fermi level, at a location z and energy E , the LDOS $\rho_s(z, E)$ of the sample is defined as:

$$\rho_s(z, E_F) = \frac{1}{\epsilon} \sum_{E_n=E-\epsilon}^E |\psi(z)|^2, \quad (2.7)$$

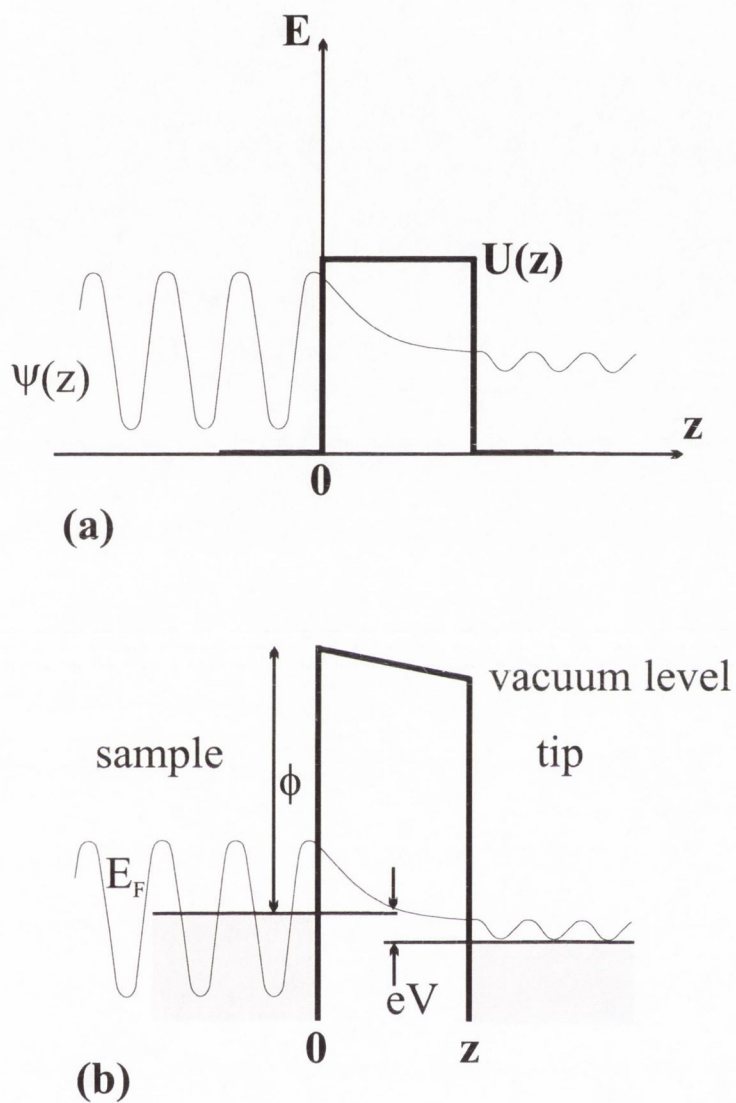


Figure 2.2: Schematic representations of (a) an electron described by the wavefunction $\psi(z)$ travelling in a one-dimensional potential $U(z)$ and (b) a STM junction under an applied bias V .

for a sufficiently small ϵ . The LDOS is the number of electrons per unit volume per unit energy, at a given point in space and at a given energy. The tunneling current can be conveniently written in terms of the LDOS of the sample at $z=0$ and $E = E_F$:

$$I_t \propto V \rho_s(0, E_F) e^{-2\kappa W} \quad (2.8)$$

It is clear from this equation that: (1) the tunnel current is directly proportional to the bias applied across the junction, (2) it decays exponentially as the distance between the tip apex and the sample surface is increased.

The significance of the probe-tip LDOS contribution is realised through a time-dependent perturbation model of metal-insulator-metal tunneling proposed by Bardeen [14]. Here, a *Transfer Hamiltonian* H_T is used to describe the transfer of a tunneling electron from a sample state ψ to a tip state χ . The tunnel current can be taken as a convolution of the sample LDOS ρ_s and the tip LDOS ρ_t .

$$I_t = \frac{4\pi e}{\hbar} \int_0^{eV} \rho_s(E_F - eV + E) \rho_t(E_F - E) |M|^2 dE \quad (2.9)$$

I_t also includes a tunneling matrix element M , describing the amplitude of electron transfer across the tunnel barrier (through the overlap of the ψ and χ states). The integral describing M is evaluated over any surface lying within the barrier region and rate of electron transfer is determined by the Fermi golden rule [15].

$$M = \frac{\hbar}{2m} \int (\chi^* \frac{\partial \psi}{\partial z} - \psi \frac{\partial \chi^*}{\partial z}) dS \quad (2.10)$$

Bardeen and Giaever [14] assumed that the magnitude of the tunneling matrix element $|M|$ does not change appreciably in the interval of interest. Then, the tunneling current is determined by the convolution of the DOS of two electrodes:

$$I_t = \frac{4\pi e}{\hbar} \int_0^{eV} \rho_s(E_F - eV + E) \rho_t(E_F - E) dE \quad (2.11)$$

2.1.3 Scanning tunneling spectroscopy (STS)

Equation 2.11 shows that the tunneling current can be expressed as a convolution of the sample LDOS ρ_s and tip LDOS ρ_t (see equation 2.9). In the semiclassical WKB approximation the tunneling current density between two planar electrodes can be expressed by:

$$J(s, V) \cong \frac{2\pi e}{\hbar} \left(\frac{\hbar^2}{2m} \right) \int_{+\infty}^{-\infty} T(s, V, E) [f(E - eV) - f(E)] \cdot \rho_s(E) \rho_t(E - eV) dE$$

where s is the tip-sample distance, V is the sample bias voltage, $T(s, V, E)$ is the tunneling transmission probability, $\rho_s(E)$ and $\rho_t(E)$ are LDOS of the surface and the tip respectively. $f(E)$ is the Fermi-Dirac distribution function.

In scanning tunneling spectroscopy formalism, the first derivative of the tunneling current is usually analysed:

$$\begin{aligned} \frac{dI(s, V)}{dV} &\cong A [eT(s, V, E) \rho_s(E) \rho_t(E - eV)]_{E=eV} + \\ &\int_{eV}^0 T(s, V, E) \rho_s(E) \cdot \frac{d\rho_t(E - eV)}{dV} dE + \\ &\int_{eV}^0 \frac{dT(s, V, E)}{dV} \rho_s(E) \rho_t(E - eV) dE \end{aligned} \quad (2.12)$$

where A is a proportionality coefficient related to the effective tip-surface contact area. the usual goal of the STS experiment is to probe the DOS distribution of a sample surface. Equation 2.12 means that this measurement is meaningful only when the tip DOS as a function of energy over the range of

measurement is known a priori. Otherwise, the sample DOS does not have a definitive relation to the tunneling spectrum. In equation 2.12, if the second and third terms are neglected, a constant tip LDOS and a weak voltage dependence of the tunneling probability are assumed, dI/dV is proportional to the sample LDOS $\rho_s(E)$. This simple proportionality forms the basis of the STS and mostly dI/dV measurements are directly compared to calculated sample densities of states. In order to obtain reproducible tunneling spectra, the STM tip must have reproducible DOS, preferably flat DOS, that is, with a free-electron-metal behavior. Tip DOS are usually highly structured. Feenstra *et al.* [16] developed an in-situ tip preparation procedure which causes local melting and recrystallisation of the tip apex. This procedure results in flattening of the tip DOS allowing one to obtain reproducible STS data with W tips.

From the present discussion it is already clear that the relation between dI/dV and the sample LDOS is highly complicated. In the case of a tip with a more complicated DOS, such as Fe or MnNi tips, this approximation has to be taken with caution and it might not be so accurate as for the case of W tips. Nevertheless, reproducible STS results have been obtained with W coated with Fe tips on the surface of Mn/Fe(110) [17].

Spectroscopy spectra are presented in the bibliography as I vs Voltage, dI/dV vs Voltage and $dI/dV/[I/V]$ vs Voltage [3,18–21]. Bischoff *et al.* [22–24] showed how the dI/dV or $dI/dV/(I/V)$ curves are dependent on the exponential background (which is tip dependent) and do not describe the LDOS very accurately. A scheme to extract the LDOS from a dI/dV measurement was proposed by Ukraintsev [25]. Ukraintsev showed that normalising dI/dV with its fitted tunneling probability function (T) leads to the best recovery of the sample DOS within a one dimensional WKB approach. The tunneling

probability function, T , is given by:

$$T = t_s \exp \left[-2S \left(\frac{2m}{\hbar^2} (\phi + V/2) \right)^{1/2} \right] + t_t \exp \left[-2S \left(\frac{2m}{\hbar^2} (\phi - V/2) \right)^{1/2} \right], \quad (2.13)$$

The first(second) term of T describes tunneling from the sample(tip) Fermi level to unoccupied tip(sample) states. t [nA/V] is a proportional coefficient which is related to the tip-surface effective contact area and is proportional to the sample (for t_s) or the tip (for t_t) densities of states at the Fermi level. ϕ [eV] is given by the local work function (which is the average of the tip and sample work functions in a first approximation). S [nm] is the tip-sample distance and m the electron mass. To extract these parameters from the experimental data, dI/dV should be fitted to T [17, 22, 23].

2.1.4 Low Energy Electron Diffraction (LEED)

A plane wave incident on an atom or atoms within a unit cell will be scattered in all directions, but interference between waves scattered from neighboring unit cells will restrict the net flux to those directions in which the scattered waves from all unit cells are in phase. This requires that the scattered waves from neighboring cells differ only by an integral number of wavelengths λ . In the simple case of a one-dimensional lattice, the in-phase condition is met for all integers n which satisfy the condition:

$$a(\sin\phi_n - \sin\phi_o) = n\lambda \quad (2.14)$$

where a is the distance between scattering planes, λ is the wavelength of the incident wave and ϕ_o is the angle of the plane wave with respect to

the lattice plane. This is known as the Laue condition. If the incident and emergent beams are described by unit vectors s_0 and s_n then this can be written in vector form as:

$$a \cdot (s_n - s_0) = n\lambda \quad (2.15)$$

or

$$a \cdot \Delta s_n = n\lambda \quad (2.16)$$

where

$$\Delta s_n = s_n - s_0 \quad (2.17)$$

The diffracted beams are determined by Δs_n and, in the one-dimensional case, they are given by integral multiples of the basic unit (λ / a). This involves the reciprocal of the real space lattice vector a . We can define a reciprocal lattice vector $a^* = (1/a)$.

For surface diffraction in a 2D system, the electron beam must conserve both its energy and the component of its momentum parallel to the surface.

$$\vec{k}_{\parallel}^2 + \vec{k}_{\perp}^2 = \vec{k}'_{\parallel}{}^2 + \vec{k}'_{\perp}{}^2, \quad \vec{k}'_{\parallel} = \vec{k}_{\parallel} + \vec{g}_{hl} \quad (2.18)$$

where \vec{k}_{\parallel} and \vec{k}_{\perp} are the parallel and perpendicular momentum components of the incident beam, while \vec{k}'_{\parallel} and \vec{k}'_{\perp} are those of the diffracted beam. The *reciprocal lattice vector* \vec{g}_{hl} is related to the beam energy E_{eV} , electron mass m_e and diffraction angle α by:

$$|\vec{g}_{hl}| = |h\vec{a}^* + l\vec{b}^*| = |\vec{k}| \sin\alpha = \frac{\sqrt{2m_e E_{eV}}}{\hbar} \sin\alpha \quad (2.19)$$

where \vec{a}^* and \vec{b}^* are the reciprocal lattice vectors. These are related to the real space vectors \vec{a} and \vec{b} by [26]:

$$\vec{a} \cdot \vec{a}^* = \vec{b} \cdot \vec{b}^* = 2\pi \quad \vec{a} \cdot \vec{b}^* = \vec{b} \cdot \vec{a}^* = 0 \quad (2.20)$$

This shows the direct correspondance between the observed diffraction pattern and the reciprocal lattice of the surface. The reciprocal lattice vector g_{hl} lies in a direction that is orthogonal to the plane of the real space lattice that is denoted by the Miller indices h and l . The Miller indices of the diffracting planes are used to index the diffraction spots of the LEED pattern.

2.2 Magnetite: Fe_3O_4

2.2.1 Introduction

Magnetite, Fe_3O_4 , is a truly unique material. The ancient Greeks noted magnetism in the mineral magnetite or lodestone. Magnetism gets its name from the Magnates, inhabitants of Magnesia and named by the Greeks, where lodestone is very abundant. Many living organisms, including humans, have used magnetite for navigation [27] for centuries. Nowadays, magnetite is of a high technological importance, with a range of applications including uses in the cores of electromagnets, in microwave resonant circuits, in computer memory cores and in high density magnetic recording media. In the last decade, the possibility of imaging the atomic structure and the electronic properties of a surface provided by STM has also boosted the fundamental research interest of imaging magnetic surfaces with magnetic contrast down to atomic scale. This technique is commonly known as spin-polarised scanning tunneling microscopy (SP-STM) [28–35].

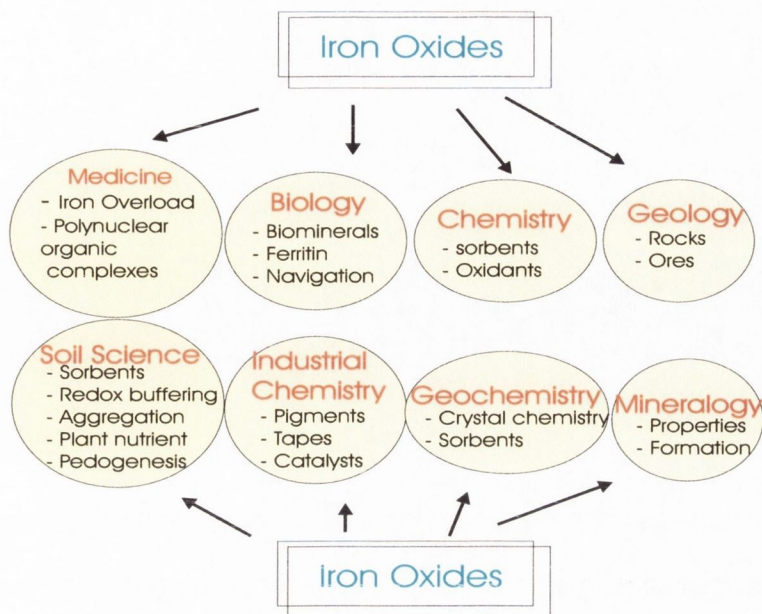


Figure 2.3: The multidisciplinary nature of iron oxide research

Magnetite is part of the iron oxide family. These compounds are in fact either oxides, hydroxides and oxide hydroxides [36]. The Fe-O system is formed by wüstite Fe_{1-x}O , magnetite Fe_3O_4 , hematite $\alpha\text{-Fe}_2\text{O}_3$ and maghemite $\gamma\text{-Fe}_2\text{O}_3$. Some physical properties are described for the different iron oxides on table 2.1.

Iron oxides are essential for other fundamental sciences as well as for a wide range of applications. Medicine, biology, environmental chemistry, geology and soil science are examples of the multidisciplines using of iron oxides (see figure 2.3) [36].

In this thesis the surfaces of magnetite (001) and (110) are studied. Preparing the surface of magnetite is not trivial and undesirable iron oxide-phases transition need to be avoided. Figure 2.4 shows the equilibrium phase diagram of the iron-oxygen system and the stability domains for wüstite Fe_{1-x}O , magnetite Fe_3O_4 , maghemite $\gamma\text{-Fe}_2\text{O}_3$ and hematite $\alpha\text{-Fe}_2\text{O}_3$ as a

	Magnetite	Haematite	Maghemite	Wüstite
<i>Formula</i>	Fe_3O_4	$\alpha\text{-Fe}_2\text{O}_3$	$\gamma\text{-Fe}_2\text{O}_3$	FeO
<i>Structural type</i>	Inverse spinel	Corundum	Defect spinel	Defect NaCl
<i>Crystal system</i>	Cubic	Hexagonal	Cubic/ Tetragonal	Cubic
<i>Space group</i>	$\text{O}_h^7\text{-Fd}3\text{m}$	$\text{D}_{2h}^{16}\text{-R}\bar{3}\text{c}$	$\text{O}_h^7\text{-Fd}3\text{m}/$ $\text{P}4_32_12$	$\text{O}_h^5, \text{Fm}3\text{m}$
<i>Cell dimensions (nm)</i>	a: 0.84	a: 0.50 c: 1.38	a: 0.84/ a: 0.83 c: 2.50	a: 0.43
<i>Colour</i>	Black	Red	Brown	Black
<i>Magnetic order</i>	Ferri-	Weakly ferro-	Ferri-	Antiferro-
<i>Curie/Neel temperature (K)</i>	850 $T_V: 119$	956	820–986 ⁽¹⁾	203–211
<i>RT Saturation magnetisation ($\text{JT}^{-1}\text{Kg}^{-1}$)</i>	92–100	0.3	60–80	–
<i>Density (gcm^3)</i>	5.18	5.26	4.87	5.9
<i>Formula units per unit cell</i>	8	6	8	4

Table 2.1: Some properties of the iron oxides. (Cornell [36]) (1) The T_C of maghemite is uncertain because it transforms to haematite above ~ 713 K.

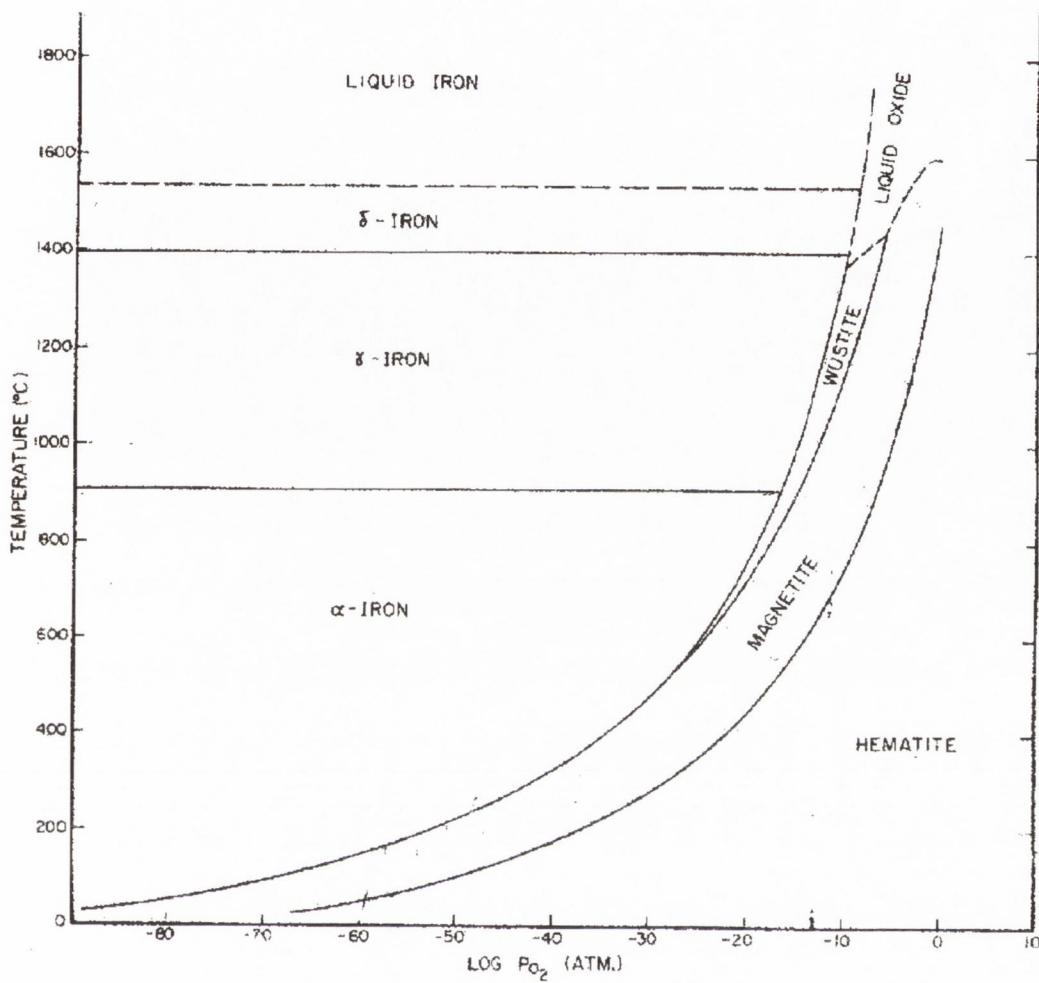
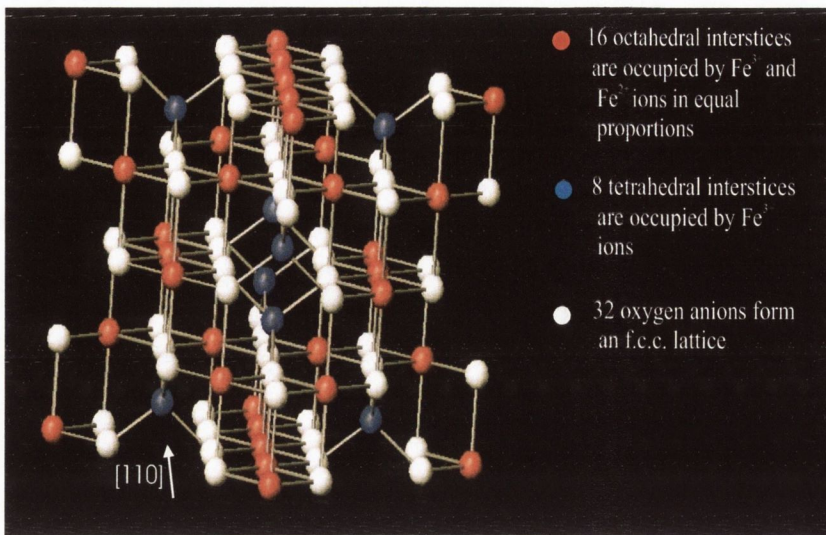


Figure 2.4: Phase diagram for the Fe – O system. Reproduced from [36]

function of the temperature and oxygen content.

Bulk Fe_3O_4 has a cubic inverse-spinel structure, where the 32 O^{2-} anions form an face centered cubic (f.c.c.) lattice, half of the Fe^{3+} cations occupy 1/8 of the available tetrahedral sites (64 available A-sites) and the other half of the Fe^{3+} cations are located in 1/4 of the available octahedral interstices (32 available B-sites). 1/4 sites of the octahedral interstices is occupied by Fe^{2+} cations. The unit cell edge constant is $a = 0.83963$ nm [37]. For stoichiometric Fe_3O_4 there are 2Fe^{3+} and 1Fe^{2+} per chemical formula. See figure 2.5.

Figure 2.5: Unit cell of Fe_3O_4

Magnetite is also predicted to be a half-metallic ferrimagnet [1,19], meaning that in the spin-up sub-band it is a metal and in the spin-down sub-band it is an insulator. There is a gap in the majority spin band at the Fermi level but there is not in the minority spin band. Filled bands of the majority spin are mainly composed of $3d$ levels of Fe in the B site. For the A site $3d$ orbitals of Fe are filled by the minority spin electron. Moreover, the orbitals just below the Fermi level are composed of $3d$ levels of Fe in the B sites [1,38]. *Alvarado et al.* have also demonstrated [38] that the electrons from the O $2p$ states lie well below the Fermi energy.

At a temperature of 120 K bulk magnetite exhibits a metal-insulator transition, known as the Verwey transition [2,4], at which its conductivity decreases by some two orders of magnitude [5,6]. Above the Verwey transition temperature, magnetite is thought to be a half-metal [1,3] with a highest known T_c of 860 K [39]. At room temperature, the electrical conductivity of Fe_3O_4 is some $200 \Omega^{-1} \text{cm}^{-1}$. This first order metal-insulator transition [40], is associated with a lattice distortion from cubic to monoclinic, which however

has not been fully resolved [41, 42]. The transition has been viewed as an order-disorder transition in relation to the arrangement of cations on the octahedral sites of the inverse spinel structure whose formal chemical formula can be written as $\text{Fe}_A^{2+}[\text{Fe}^{2+}\text{Fe}^{3+}]_B\text{O}_4^{2-}$ [43–47].

2.2.2 The surface of Fe_3O_4 (001)

The (001) plane of magnetite can be viewed as a stacking sequence of two alternating layers. The A-layer contains tetrahedrally coordinated Fe^{3+} ions, while the B-layer is composed of rows of octahedrally coordinated Fe^{2+} and Fe^{3+} ions surrounded by oxygen ions. The separation between neighbouring planes (i.e. the A-B interplanar separation) is 1.05 Å, while the separation between successive like planes (i.e. the A-A or B-B interplanar separation) is 2.10 Å. In each octahedral plane, the nearest-neighbor B-site cations form rows that run along the [110] and $[1\bar{1}0]$ directions.

The rows in successive octahedral planes are rotated by 90° with respect to one another, giving these planes a two-fold rotational symmetry. In contrast, the arrangement of cations in the A-layers give them a four-fold rotational symmetry. A ball model of Fe_3O_4 (001) is shown in figures 2.6 and 2.7 where a full B and A-terminated surface are depicted respectively.

2.2.3 The surface of magnetite (110)

The bulk of Fe_3O_4 can be thought to consist of two different planes perpendicular to [110] with arrangement of the Fe and O ions as given in figure 2.8.

These type-A and type-B layers alternate with a spacing of 1.484 Å between successive layers. The type-A contains only iron ions on the octahedral

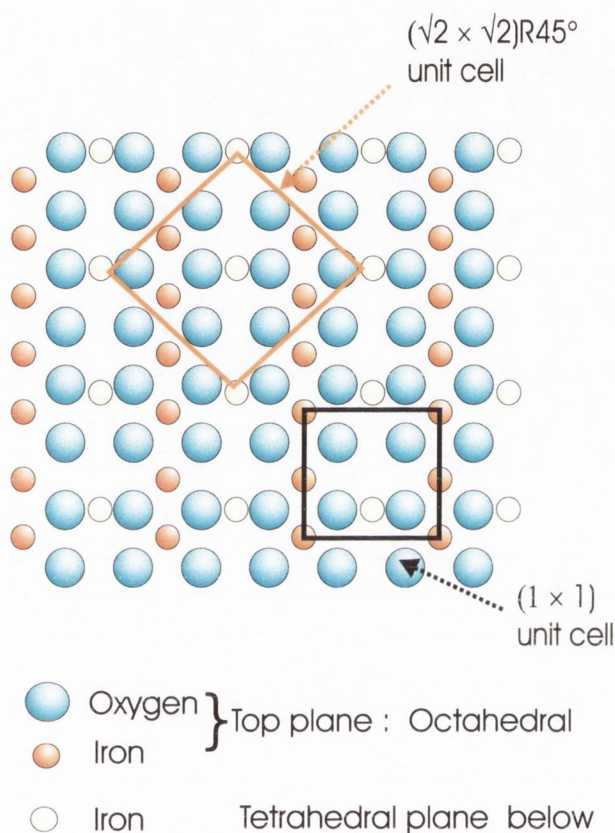


Figure 2.6: The (001) *B*-terminated surface of Fe_3O_4 . The large circles represent oxygen atoms forming an f.c.c. lattice. The small circles depict iron atoms located at the *A* and *B* sites. The $p(1 \times 1)$ primitive unit cell is marked with a black square. The $(\sqrt{2} \times \sqrt{2})R45^\circ$ unit cell is marked with a orange square.

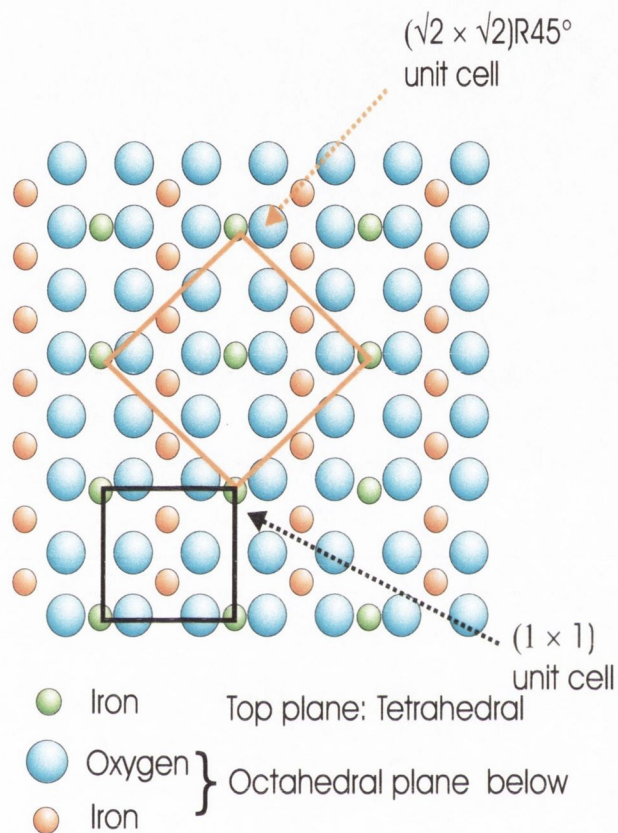


Figure 2.7: The (001) *A*-terminated surface of Fe_3O_4 . The large circles represent oxygen atoms forming an f.c.c. lattice on the layer below. The small circles depict iron atoms located at the *A* and *B* sites. The $p(1 \times 1)$ primitive unit cell is marked with a black square. The $(\sqrt{2} \times \sqrt{2})R45^\circ$ unit cell is marked with a orange square.

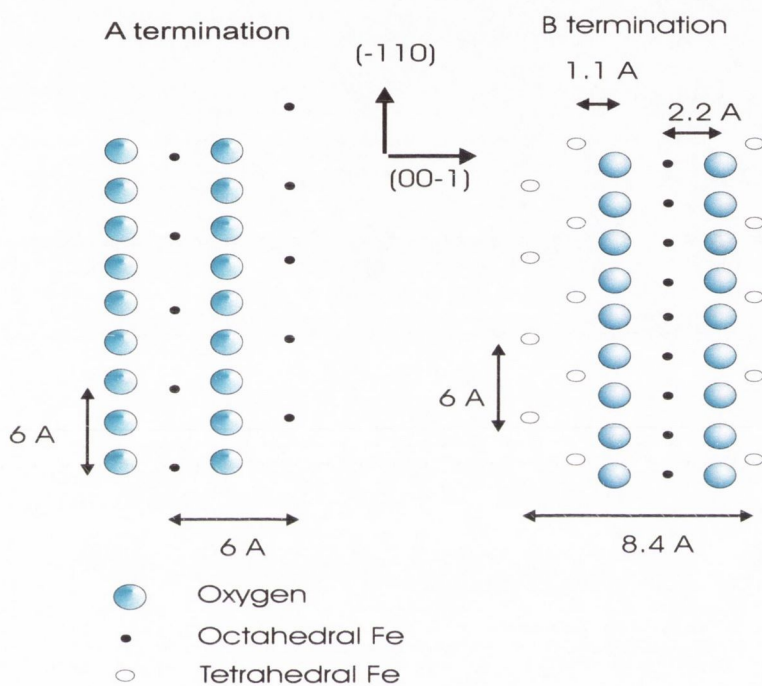


Figure 2.8: The atomic arrangement in the two types of (110) layers A and B presented in the bulk Fe₂O₃. The surface unit cell is 8.4 Å along the (001) and 6 Å along the (-110).

positions. The type-B contains both octahedrally and tetrahedrally coordinated Fe ions which have antiparallel magnetic moments (see figure 2.8). Magnetite (110) is a non-polar surface. This means that the surface of Fe_3O_4 (110) has no dipole moment perpendicular to the surface, therefore it has a finite surface energy meaning that the surface may retain the structure of the bulk termination with minor relaxations [48] (see appendix C).

2.2.4 Autocompensated surfaces

The concept of autocompensation, originally developed for surfaces of compound semiconductors, such as GaAs and ZnSe [49], is very successful for predicting reconstructions of metal oxide surfaces [50]. The most stable surfaces are predicted to be those which are autocompensated, which means that excess charge from cation-derived dangling bonds compensates anion-derived dangling bonds. The surface is then "self-compensated", that is the cation-(anion) derived dangling bonds are completely empty (full) on stable surfaces. This model allows for the partially covalent character found in many metal oxides, including oxides of iron. This simple electron-counting approach is somewhat more complicated in Fe_3O_4 because of the mixed valency and coordination of iron ions in the inverse spinel structure.

For magnetite, one tetrahedral Fe^{3+} ion contributes three electrons to a total of four bonds to neighboring oxygen atoms in bulk Fe_3O_4 . Therefore, each bond contains $\frac{3}{4} e^-$ that are donated from the tetrahedral iron ions. Above the Verwey transition, electrons hop freely between octahedral Fe^{2+} and Fe^{3+} , giving rise to an average formal oxidation state for iron of 2.5. Each octahedral iron ion contributes $2.5 e^-$ to a total of six bonds to oxygen ions. Each Fe(oct)-O bond thus contains $\frac{2.5}{6} = \frac{5}{12} e^-$ contributed from iron

ions. Assuming two electrons per bond, each oxygen contributes $2 - \frac{3}{4} e^- = \frac{5}{4} e^-$ to each Fe(tet)-O bond, and $2 - \frac{5}{12} e^- = \frac{19}{12} e^-$, to each Fe(oct)-O bond. These numbers can be used to determine dangling bond charges when different surfaces structures are created. This is known as the *electron-counting model*.

This is formally equivalent to conditions for creating a non-polar surfaces of ionic (or partially ionic) crystals introduced by Tasker [51]. The *electrostatic model* proposed by Tasker classifies the surfaces of any ionic or partially ionic materials into three types. Type 1 consists of neutral planes with both anions and cations (i.e. (001) and (110) surfaces of rocksalt metal oxides, such as MgO and NiO). Type 2 consists of charged planes arranged symmetrically so that there is no dipole moment perpendicular to the unit cell (i.e. (111) surface of the fluorite structure terminated with an anion plane). Neither of these surfaces affect ions in the bulk of the crystal and they should therefore have modest surface energies (also called *non-polar*), which diverges when a net dipole is presence on the surface. The type 3 surface is charged and there is a perpendicular dipole moment. These surfaces have infinite surface energies (i.e. (111) surfaces in the rocksalt structure). These surfaces are also called *polar* (see appendix C).

For *A* or *B*-bulk terminated Fe_3O_4 (001) surface electrostatic arguments lead to uncompensated charge at the surface. In figure 2.9 a schematic representation of a polar crystal is shown. The ionic charge of ± 6 per layer unit cell is autocompensated throughout the bulk of the crystal in magnetite (001). However, an extra charge of ± 3 (depending on an *A* or *B* surface termination) is not compensated when the surface is created. For energetic reasons charge neutrality is required. Charge neutrality at the polar (001) surface of Fe_3O_4 must be realized by an adjustment of the structure and

polar surfaces, therefore intrinsically unstable. It belongs to type 3 surfaces according to Tasker's model. The surface of magnetite (110) is a non-polar surface [48].

2.2.5 Literature review

The clean $\text{Fe}_3\text{O}_4(001)$ surface

As explained in section 2.2.2, the (001) plane of magnetite can be viewed as a stacking sequence of two alternating layers, *A* and *B*, containing iron ions on the tetrahedral and octahedral sites respectively .

Both A- [52–54] and B- [47, 55, 56] terminated surfaces have been reported in the literature, with no satisfactory explanation as to why the (001) magnetite surface should be terminated at either plane. However it is clear that the preparation conditions play a crucial role in determining the surface termination.

A $(\sqrt{2} \times \sqrt{2})R45^\circ$ reconstruction has been observed by several groups on the clean magnetite (001) surface of both natural and synthetic single crystals, and on thin films grown by Molecular Beam Epitaxy (MBE)². STM studies carried out by Tarrach *et al.* [52] have suggested that the top-most surface layer consists of a full monolayer of tetrahedral Fe ions. Chambers *et al.* [54] used x-ray photoelectron spectroscopy (XPS), X-ray

²Two different notations to define the same surface reconstruction are used in the literature leading to confusion. Some authors [52,53,57] reference the reconstructed surface to the bulk unit cell and call it $p(1 \times 1)$. Others [56,58–60] reference the simplest primitive unit mesh to the unreconstructed surface, and consequently this reconstruction is called $(\sqrt{2} \times \sqrt{2})R45^\circ$. In surface crystallography it is common to denote any unreconstructed surface with the smallest primitive (1×1) unit cell and the latter notation is adopted in this thesis

photoelectron diffraction (XPD) and STM to support the conclusion that the Fe_3O_4 (001) surface is constituted by half filled layer of tetrahedral Fe ions. The latter surface termination is charge compensated. Wiesendanger *et al.* [34] imaged two distinct structures on different areas of a natural crystal of magnetite; the two structures were attributed to bulk terminated tetrahedral and octahedral terminations of the surface. In contrast, Voogt *et al.* [55] and more recently Stanka *et al.* [56] have proposed a B-terminated layer on a single crystal and a $\text{Fe}_3\text{O}_4/\text{MgO}(001)$ film, respectively. In both cases, they have proposed that charge compensation is achieved by an array of oxygen vacancies accompanied by a change in the valence state of the Fe. Mariotto *et al.* [47] observed a $(\sqrt{2} \times \sqrt{2})R45^\circ$ reconstruction on a clean magnetite (001) single crystal surface interpreted as a B-layer surface termination. Mariotto *et al.* further proposed that the reconstruction is due to charge ordering of the Fe cations in octahedral positions, and not to an ordered array of vacancies as proposed by previous studies. Such a surface is not charge compensated.

The contaminated $\text{Fe}_3\text{O}_4(001)$ surface

Surface reconstructions induced by alkaline and alkaline-earth metals have been observed on a range of different systems, such as thin films of Fe_3O_4 grown on $\text{MgO}(001)$ substrates [60,61], thin films of Fe_3O_4 grown on $\text{Pt}(111)$ substrates [62] and TiO_2 single crystals [63,64]. A $p(1 \times 4)$ reconstruction was observed by Anderson *et al.* [60] on a $1 \mu\text{m}$ thick film of magnetite grown on a MgO (001) substrate. A similar effect was observed by Voogt *et al.* [55] who reported the onset of a $p(1 \times 3)$ reconstruction on a magnetite thin film grown on MgO (001). Anderson *et al.* attributed the surface reconstruction

to the segregation of magnesium from the substrate, leading to the formation of a MgFe_2O_4 phase. Kim *et al.* [59] in a study of magnetite thin films grown on MgO (001) suggested that the Mg ions diffuse through the iron oxide via vacancies in the octahedral cation sublattice. Once they reach the surface, they decorate the rows of octahedral *B*-site cations. Nörenberg *et al.* [64] have investigated Ca-induced surface reconstructions on TiO_2 . They have observed a variety of surface reconstructions, including $p(1\times 3)$ and $p(1\times 4)$. They attributed the $p(1\times 3)$ reconstruction to Ca^{2+} cations replacing the Ti cations at the surface of the crystal. A $p(1\times 4)$ reconstruction, caused by an ordered array of trenches, was found to succeed the $p(1\times 3)$ reconstruction and it was attributed to oxygen loss from the surface.

Magnetite is a particularly well suited material for these studies. The polar surface of magnetite must reconstruct or undergo a charge redistribution to minimize the surface energy. As explained and demonstrated in chapter 5, a clean surface of magnetite terminated at the (001) plane exhibits a $(\sqrt{2}\times\sqrt{2})R45^\circ$ reconstruction. The contaminant free magnetite surface had revealed interesting data of its fundamental properties. These fundamental properties are modified by the presence of contaminants on the surface.

Nanostructures will play a fundamental role in many future electronic, mechanical and optical devices. The traditional methods of microfabrication, e.g. lithographic methods, are limited in their resolution and new techniques to manipulate atoms and molecules to ultimately fabricate nanodevices are developing [65–68]. Since the latter is far too slow and awkward, a different method is that of self assembly of atoms and molecules in nanostructures. As an alternative method to the deposition of atoms onto a substrate, the controlled diffusion of impurities from the bulk of a single crystal to the surface or, in the case of thin films, from the substrate into the film is

proposed as a method by which self-assembly can be achieved. One could use these nanotemplates for the deposition of carbon nanotubes, fullerenes and DNA molecules, whose sizes are compatible with the typical dimensions of our nanotemplates. Organic/Inorganic interfaces are suitable for building and testing new electronic devices that could be used in nanotechnology such as organic light emitting diodes (OLEDs), organic field effect transistors (OFETs) [69,70], solar cells [71], sensors etc. Several studies have been made, investigating the formation of thin semiconductor organic molecules on semiconductors [72,73] and metallic surfaces, such as: gold [56], silver, nickel [74], copper [75] etc. Organic epitaxy on inorganic substrates is no easy task, but can successfully be achieved if the molecule/substrate combination is properly chosen and if the interface is optimised. Since very few suitable systems have previously been considered, the study of new candidate systems could be a very productive area of future research. These organic molecules can modify the properties of metals and semiconductors (i.e. the density of states, electronic and magnetic properties.) and vice versa. 1-D nanostructures of organic large organic molecules could be an starting point for fundamental research (*i.e.* study of the interaction of organic molecules with an arranged pattern) and development of the mentioned molecular devices [76].

The surface of Fe_3O_4 (110)

As explained in section 2.5, magnetite (110) is a non-polar surface. The surface of Fe_3O_4 (110) has a finite energy, meaning that it may retain the structure of the bulk termination with minor relaxations according to Tasker's model [51].

There has not been much research carried out on the surface of magnetite (110) compared to the polar surfaces (001) and (111). Jansen *et al.* [77] stud-

ied the surface of artificially grown single crystals of magnetite (110). A clean terraced surface was obtained by STM for annealing temperatures of 1200 K. LEED and STM data showed a magnetite (110) reconstructed surface. STM images showed atomic rows running along the $[1\bar{1}0]$ with a periodicity of multiples of 3 Å and a separation between the rows of 17, 24 and 34 Å along the [001] direction. To explain the surface reconstruction, a model based on iron oxide phase transition (from Fe_3O_4 to $\alpha\text{-Fe}_2\text{O}_3$ -like) was proposed. These results were corroborated by the same author using STM/STS when investigating a 50 nm Fe_3O_4 (110) film grown on a MgO substrate [78]. Annealing of the thin film at 850 K produced the formation of rows separated by 20-40 Å periodicity along the [001] direction. The formation of a MgFe_2O_4 phase on the surface was also discussed, but this explanation was ruled out.

Oda *et al.* [79] carried out a LEED investigation on a clean surface of Fe_3O_4 (110) single crystal. Annealing of the crystal at 850 K was enough to produce a sharp LEED pattern. Missing spots along the $[1\bar{1}0]$ direction have been seen on their LEED patterns. A model based on a Fe_3O_4 - $p2mg$ -(1 × 3) surface was proposed for this surface. This result disagrees with that obtained by Jansen *et al.* and it is attributed to the different annealing temperature and a better quality of the single crystal.

Chapter 3

Experimental details

3.1 The ultrahigh vacuum set up

The original UHV system was designed and constructed by Professor I.V. Shvets, Dr. A. Quinn and Dr. J. Osing. It consists of three main chambers: the preparation chamber, the room-temperature STM (RTSTM) chamber and the low-temperature STM (LTSTM) chamber. The layout of this system is shown schematically in figure 3.1. A full description of the construction and operation of the RTSTM and preparation systems is given by Quinn [80]. The LTSTM description can be found in [81]. Finally the RTSTM is detailed in [82].

Each chamber can be valved off from the rest of the system via a series of UHV gate valves (VAT [83]) and brought to atmospheric pressure for maintenance without breaking vacuum in the rest of the system. Samples and STM tips are introduced to the system via a fast-entry loadlock connected to the preparation chamber by a gate valve. When not in use, this loadlock is usually maintained in the low 10^{-8} mbar range by a $20 \text{ L} \cdot \text{s}^{-1}$ differential ion-pump (Perkin-Elmer [84]). Tip and sample transfer throughout the

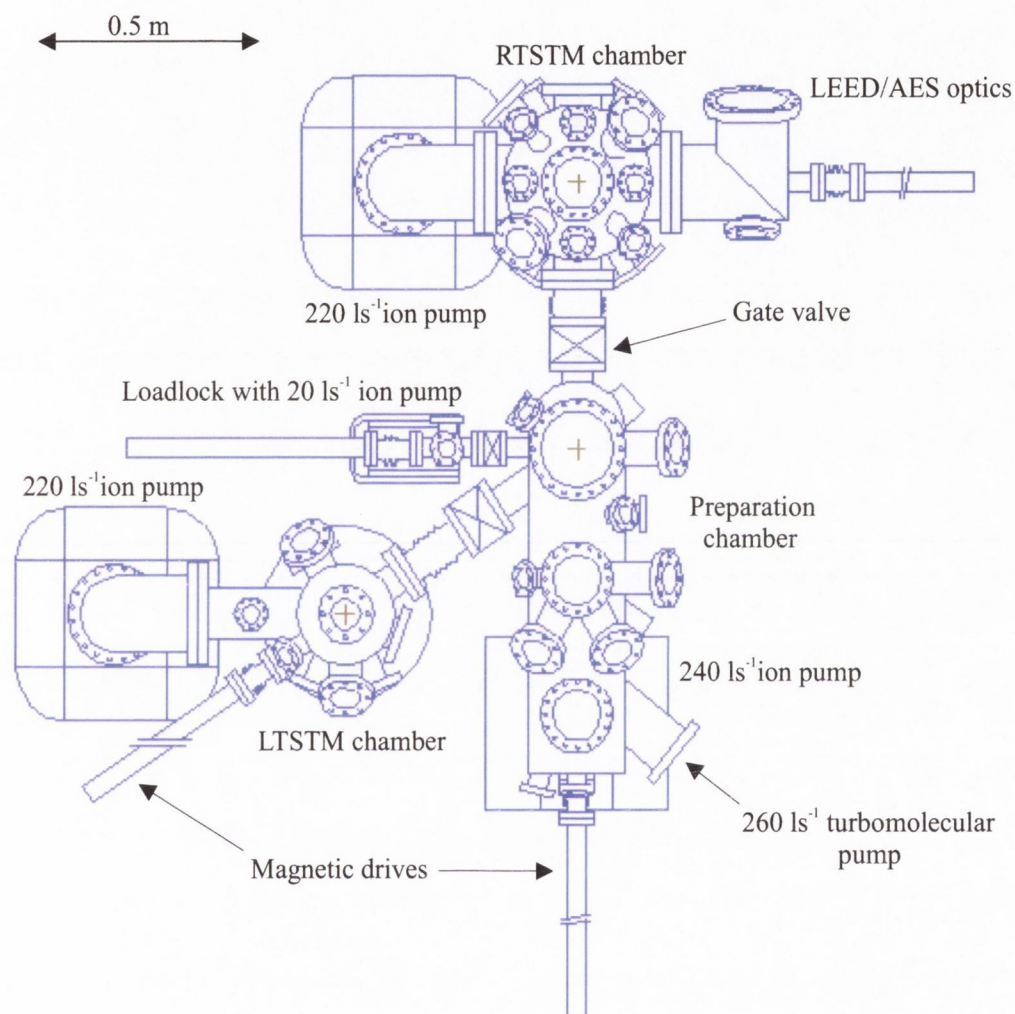


Figure 3.1: Top view schematic of the UHV system.

chamber is facilitated by a series of wobblesticks and magnetically-coupled linear drives (Vacuum Generators Ltd. [85]) which can access each sample stage. The pressure in each chamber is monitored using nude Bayard-Alpert type ionisation gauges (Perkin-Elmer). The entire system is supported on a stainless steel box-section frame which can be floated on pneumatic dampers to isolate the system from building vibrations during STM operation. The box-section is filled with gravel to minimise hollow pipe vibrations.

3.2 The preparation chamber

The preparation chamber was designed by Dr. S. Murphy [82] and manufactured by Caburn-MDC Ltd. [86]. It is a standard O.D. 457 mm commercial chamber (Perkin-Elmer) with two modified ports and total of twenty-one ports. To achieve UHV the chamber is usually baked for 3 days at 170-180 °C. A customised bake-out tent was designed by the author and manufactured by [86]. A base pressure in the low $\sim 10^{-10}$ mbar is obtained in this chamber after baking out.

A number of pumps are used to achieve UHV conditions in the chamber: the first is a TMU 260 L · s⁻¹ turbomolecular pump (Pfeiffer Vacuum [87]). This pump is backed by a 0.7 L · s⁻¹ two-stage rotary vane pump. A double-ended 240 L · s⁻¹ differential ion-pump (Physical Electronics [84]) is used to maintain UHV conditions. A liquid nitrogen cryoshroud is inserted in the base flange of the ion-pump which houses a titanium sublimation pump (TSP). A non-evaporable getter pump (NEG) from SAES Getters [88] is positioned mid-way along the chamber. This pump is particularly effective pumping in hydrogen.

The chamber contains all the facilities for *in-situ* tip and sample prepa-

ration: electron-beam and resistive heaters, quartz crystal deposition monitor (Inficon [89]), a triple evaporator with integral flux monitor, ion-gun (VG [90]) and precision leak valves for controlled introduction of high purity oxygen, hydrogen and argon gases. In addition, the preparation chamber also contains a cylindrical mirror analyser (CMA) based AES subsystem (Perkin-Elmer) for sample characterization. A detailed description of the main sample preparation facilities used for the preparation and analysis of the crystals covered in this thesis is given below.

3.2.1 The resistive heater

The heater was designed by C. Kempf. The heater consists of an alumina crucible with a spiral groove machined along its circumference along which a $\phi = 0.2$ mm W wire is wrapped. The sample sits inside a Ta insert which fits inside the crucible. Both the crucible and the Ta insert have concentric apertures machined in their bases. The sample can be inserted face-down for film depositions or face-up for Ar^+ ion bombardment. The crucible fits inside a stainless steel can which is connected to the feedthrough for the quartz crystal monitor. This feedthrough comprises two water cooling pipes and a BNC feedthrough to carry the quartz crystal signal to the monitor. A separate feedthrough carries the connections to the heater filament and a K-type (Omega) thermocouple which is spot-welded to the Ta insert. A schematic of the resistive heater set-up can be seen in figure 3.2. The heater was calibrated for temperature ($^{\circ}\text{C}$) *versus* filament power (W) with the thermocouple attached in this position and to the face of a sample-holder mounted face-down in the heater. Samples can be heated up to a temperature range of $350 \text{ K} \leq T_{flash} \leq 900 \text{ K}$.

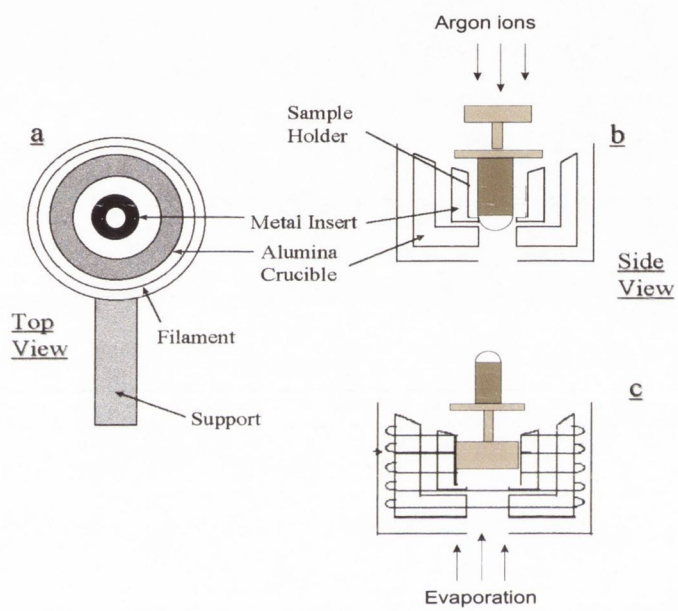


Figure 3.2: Schematic illustration of the resistive heater. The sample can sit face-down in the heater for evaporation experiments. Alternatively, the sample (or tip) is inserted face-up for ion-etching. Reproduced from [91].

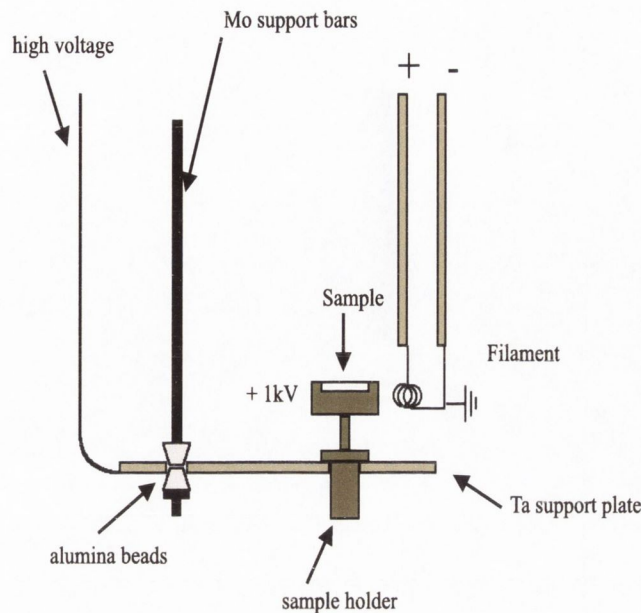


Figure 3.3: A schematic illustration of the e-beam heater. Reproduced from [81].

3.2.2 The e-beam heater

The electron beam heater was designed and assembled by Dr. J. Osing [81]. It was initially used for the sample preparation treatment of tungsten, molybdenum and magnetite surfaces. Short flash-annealing of the surface at very high temperatures ($1000 \text{ K} \leq T_{flash} \leq 2600 \text{ K}$ for 15-20 seconds in UHV) are able to remove impurities from the surface [82]. A schematic illustration of the e-beam set-up is shown in figure 3.3. The sample is clamped in a sample holder between a Ta cap that screws onto a Mo body. The sample holder is mounted into a Ta stage which is held at a potential of +1 kV.

A current ($1.5 \text{ A} \leq I \leq 4.5 \text{ A}$) is passed through a grounded thoriated tungsten filament ($\phi = 0.15 \text{ mm}$, 0.6 % Th) which generates thermionic emission of electrons. These electrons are accelerated towards the cap of the sample holder, where upon collision, their kinetic energy is transferred

to the sample as heat. Because the filament is situated to one side of the sample there will be a temperature gradient across the sample, however, this set-up produces a contamination free surface. Surface temperatures are measured from outside the chamber using an infra-red pyrometer (Altimex UX-20/600 [92]).

3.2.3 The ion gun

The preparation chamber is fitted with a inert sputter ion source (PSP vacuum technology [93]), which is used for Ar^+ ion etching of STM tips and for some sputtering experiments. The argon gas is introduced by leak-valve directly into the gas-cell of the ion-gun, the base pressure in the chamber rises to $5 \times 10^{-6} \leq P_{base} \leq 1 \times 10^{-5}$ mbar. An energy from 0.5 to 3 KeV is applied to the ions for rapid cleaning of samples in UHV. The ions are created by an oscillating electron discharge inside a chamber at Ion Energy (kinetic energy) potential. There are two long life tungsten filaments which typical filament currents of 2.6 A will run through. Discharge currents used usually vary from 30-40 mA. The target diameter is taken as 11 mm, which is the diameter of the circular Ta insert in the resistive heater, into which the sample/tip is mounted for ion-etching. A sample/gun working distance of 100 mm is required for this ion-gun. This insert is isolated from ground by the surrounding ceramic crucible. The thermocouple spot-welded to this insert allows the target current to be measured. This is typically of the order of $8.0 \leq I \leq 20.0 \mu\text{A}$ for a 0.5-2 keV beam energy and a chamber pressure of 1×10^{-5} mbar.

An estimate of the amount of material removed from the surface by sputtering can be calculated knowing the incident ion flux (calculated from the

target current) and the sputter yield Y (the number of target atoms ejected per incident ion). The sputter rate ν is obtained from the relation [11]:

$$\nu = \frac{JYM}{\rho e N_A n} \quad [m.s^{-1}] \quad (3.1)$$

where J is the ion current density ($A.m^{-2}$), Y the sputter yield (atoms/incident ion), M the molar mass of the target matrix ($kg.mol^{-1}$), ρ the density ($kg.m^{-3}$), e the electron charge ($A.s$), N_A is Avogadro's constant (mol^{-1}) and n the number of components yielded per matrix molecule ($n = 1$ for an elemental target). For a circular target, this can be re-written as:

$$\nu = \frac{4IYM}{e\pi D^2 \rho N_A} \quad [m.s^{-1}] \quad (3.2)$$

where I is the target current (A) and D is the sample diameter (m).

3.2.4 Sample Characterization: Auger Electron Spectroscopy

The main parts of the Auger spectrometer are the electron gun and the electrostatic energy analyzer. Auger spectrometer uses a cylindrical mirror analyzer (CMA, model 10-155A Physical Electronics) with a variable potential applied between an inner and outer cylinder and resulting in a signal which is proportional to the number of detected electrons N at kinetic energy E . Primary electrons of known energy which are reflected from the sample surface are used to optimise the signal intensity and calibrate the analyzer.

A beam energy of 3 keV was used for all measurements, the filament and emission currents were 3.2 A and 1.4 mA respectively, giving a target current of $\sim 8 \mu A$. A SR 850 DSP lock-in amplifier from Stanford Research

Systems [94] was used to output a $0.5 V_{rms}$ sinusoidal signal of frequency 12 kHz. A lock-in sensitivity of $100 \mu V$ was used to detect the Auger signal. The scan speed was always set at $1 eV.s^{-1}$, with scan ranges of 0-750 eV for magnetite (100)/(110) and 0-1200 eV for Fe_3O_4/MgO (001). An example of a concentration calculation for magnetite (001) is shown in the appendix 3.2.4.

3.3 The room-temperature STM

All STM images described in this thesis were obtained by scanning the tip across the surface in constant current mode. In this configuration the tip-sample separation is maintained at a constant value by means of a feedback-loop which controls a piezoelectric tube scanner holding the tip. The STM head is constructed from machineable ceramic (Macor) and comprises a piezo tube scanner and a fine approach walker based upon the system developed by Dr. S.H. Pan at the University of Basel, Switzerland [95]. The sample is mounted on top of a polished quasi-cylindrical sapphire rod which is clamped between a set of six piezo stacks. These piezo stacks are arranged pairwise in a triangular fashion about the sapphire rod with one pair of stacks spring-loaded against it. A signal composed of quarter sections of a period of a sine wave is applied to the piezo stacks. The rod is moved towards or away from the tip in two steps: first the stacks deform quickly in one direction and slip under the rod leaving its position virtually unchanged. Then they deform slowly back simultaneously and drag the rod with them. The fine approach piezo-walker can operate both in an inertial and a frictional mode. A full description of this mechanism is discussed in [96, 97].

The tube scanner is sectioned into four outer electrodes which carry the

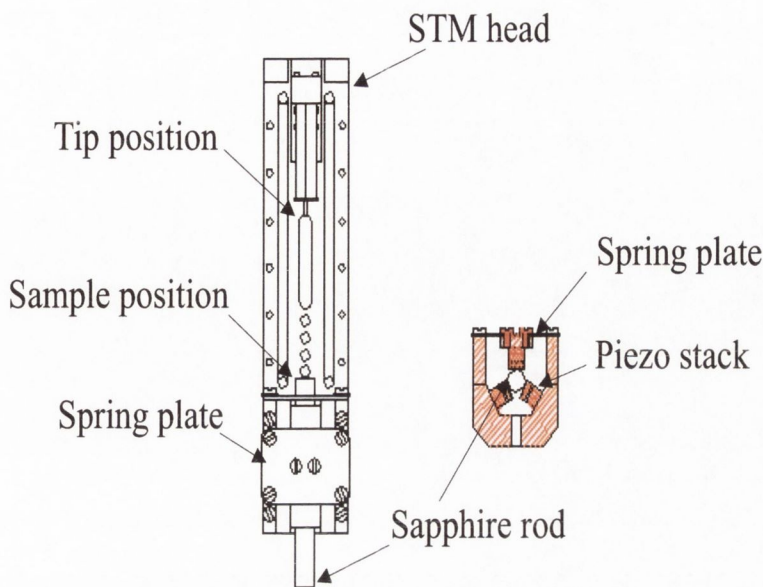


Figure 3.4: Schematic representation of a STM head similar to the RTSTM used. A front view and cross-section of the fine approach walker are shown.

Z-X, Z+X, Z-Y and Z+Y voltages, while the inner electrode is grounded. The scanner has a dynamic range of $\pm 13000 \text{ \AA}$ in the z-direction and $\pm 20600 \text{ \AA}$ in the x- and y- directions. These directions were calibrated on Cu(100) monatomic steps and HOPG atomic resolution images respectively. The STM head is isolated from vibrations by a two-stage spring system [80] which works in conjunction with the pneumatic dampers on the system frame.

The RTSTM chamber is also fitted with an electromagnet, designed and assembled by J. Naumann, to carry out magnetic STM experiments. This consists of two Permanorm 5000 poles with Kapton-insulated copper wire windings. Three thermocouples are fitted to monitor the heat output generated by the magnet. This magnet can be positioned so that the sample in the STM lies between the poles. An in-plane magnetic field of 90 mT is possible without significant overheating of the sample.

The STM controller used for these experiments is a SCALA system by Omicron [98]. This controller allows the user to compensate for the thermal drift using a topographic feature of the STM image as a reference point. A 0.1 nm/s thermal drift was measured when no correction was applied. By enabling this option, thermal drift was reduced to 0.0025 nm/s. The accompanying software provides some functions for data analysis, however data was also analysed using commercial software from Nanotec Electronica S.L. [99]

3.3.1 Four-grid LEED

The RVLO 900 four-grid reverse view optics were manufactured by VG Microtech. The optics are mounted on a O.D. 200 mm CF custom elbow which is tilted at an angle of 30° to the horizontal. The sample sits in the transfer fork of a magnetic drive, which is grounded by a stainless steel braid to an OFHC copper block at the bottom of the LEED annexe. The sample is rotated in this drive so that its surface faces the electron gun. Scattered electrons are collected by the grids and screen located behind the gun.

A schematic illustration of the four-grid LEED is shown in figure 3.5. The grid nearest the sample M1 is earthed so that electrons scattered by the sample, initially travel in field-free space. A negative potential is applied to the two centre grids M2a and M2b to suppress inelastically scattered electrons, while elastically scattered electrons are accelerated towards the phosphorescent screen by its +5 keV potential. The fourth mesh M3 is also grounded to reduce the field penetration of the suppressing grids by the screen.

LEED patterns of the metal surfaces were taken at energies between 40 and 200 eV, using an emission current of 0.5 mA the target current could not

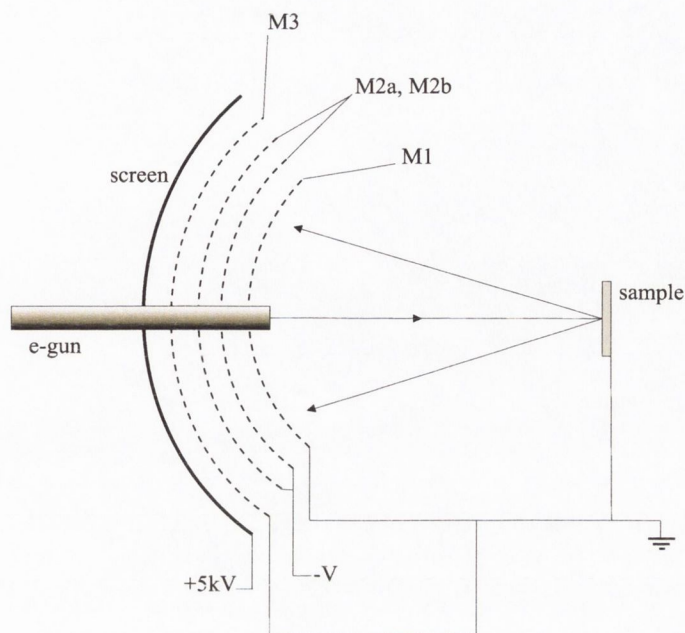


Figure 3.5: Schematic of four-grid optics operating in LEED mode (*c.f.* reference [26]).

be measured. LEED patterns were recorded by photographing the screen.

The angle α may be determined from the spot-separation d_r between indexed spots in the LEED pattern by using the geometry of the LEED screen, shown in figure 3.6. The actual spot-separation can be calculated from the distance d_{photo} measured in a photograph of the pattern if a calibration photo of the entire screen is taken, using:

$$d_r = \frac{d_{photo} D_r}{D_{photo}} \quad (3.3)$$

where D_r is the actual screen diameter and D_{photo} is the screen diameter measured in the photograph. An example of a LEED calculation on the magnetite (001) surface can be found on the appendix B.

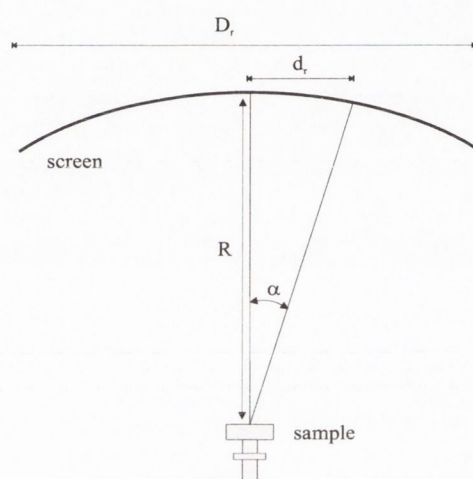


Figure 3.6: Schematic of the LEED screen geometry. The sample is placed at the focal point of the screen. The angle α can be determined from $\tan\alpha = d_r/R$. The distance d_r is the separation between the hk spot and the specular spot.

Chapter 4

Fabrication and characterisation of STM tips for spin-polarised STM and STS

4.1 Introduction

There has been substantial interest in the fabrication of probes, with well defined geometry and composition, for use in Scanning Tunneling Microscopy (STM) [100–104]. The usual criteria for a good STM tip are: (1) radius of curvature lower than 100 nm, to obtain a suitably high resolution, (2) a high aspect-ratio (i.e. the ratio of tip length to diameter) near the tip apex to allow probing of surfaces with significant roughness, (3) a low aspect-ratio away from the apex, to reduce mechanical oscillations of the tip during scanning and (4) a single apex to avoid multiple tip artefacts. A variety of techniques have been developed to produce tips with different geometries.

These are usually variations on the electrolytic etching/polishing of a thin wire ($\phi=0.25\text{-}1$ mm) with additional treatments to further sharpen the tip and to remove residues formed during the electrolytic treatment.

Much of the previous work in this field has focused on refining the preparation procedure for producing W or PtIr tips, which are now the standard tips used in most STM applications. By comparison, there has been much less investigation of the suitability of magnetic materials for STM tips [105–109]. This work deserves more attention, given the potential uses of such tips for imaging magnetic surfaces with magnetic contrast down to atomic scale, also known as spin-polarised STM (SPSTM), which have recently seen many promising developments [110–116]. A variety of tips based on ferromagnetic or antiferromagnetic materials have been proposed, including Fe and Gd coated W [117,118], Ni [119], Fe [31], CrO₂ layers on Si(111) [120], Cr, MnNi, and MnPt [121–123]. Cr coated W tips were recently used to perform spin-polarised scanning tunneling spectroscopy (SPSTS) experiments to image the domain structure of the Fe/W(110) ultrathin film system [32].

In this study, a similar technique to that described by Iijima and Yasuda [102] for preparation of Fe, Ni and FeBSiC magnetic force microscope (MFM) tips is employed, to produce STM tips from polycrystalline MnNi, Cr, Fe and Ni and W. Using this technique, we have improved upon the earlier preparation procedures developed in our laboratory [122,123], to produce tips with better geometry and with tip apexes lying in the 50–100 nm range. Special emphasis is placed on the fabrication of tips of antiferromagnetic materials. These tips, unlike ferromagnetic tips, do not produce a stray magnetic field that can affect the sample. In addition, the magnetic configuration of the tip itself is also not influenced by the stray field of the sample. Moreover, as the tip and the sample do not interact through magnetostatic forces, the

tunnel gap should be more stable.

These advantages were first highlighted by Minakov et al. [33], who calculated the spin-dependency of the tunnel current between an antiferromagnetic tip and a ferromagnetic sample. They also proposed the use of antiferromagnetic tips made from Cr for imaging magnetic surfaces with magnetic contrast down to atomic scale experiments. Cr has a Néel temperature that lies above 300 K, which makes it applicable in experiments that do not require cryogenic temperatures. Other materials with high Néel temperatures are the ordered equiatomic alloys MnNi, MnPd, MnPt, MnAu and MnIr [121]. Special emphasis has been placed on the fabrication of tips from MnNi. Because this material is an alloy, it is necessary to consider the effects of the preparation procedure on the stoichiometric composition of the tip, in addition to the usual considerations of tip geometry and sharpness.

4.2 Tip fabrication procedure

A schematic diagram of the electrochemical etching setup is shown in figure 4.1.

The rod is partially covered with a close-fitting section of teflon (PTFE) insulating tubing and then immersed into a bath of the etchant (NaOH or HCl). A modified micrometer screw is used to position the rod so that the electrolyte covers the PTFE tube. This physically restricts the active etching region to a small volume of the rod above the PTFE tubing. The tip is formed at the upper end of the PTFE tube, where the physical restriction of the etching region leads to a thinning or necking-in of the rod, as shown in the schematic in figure 4.2 a). An example of the thinning process is shown in figure 4.2 b) which was taken during the etching of a Cr rod.

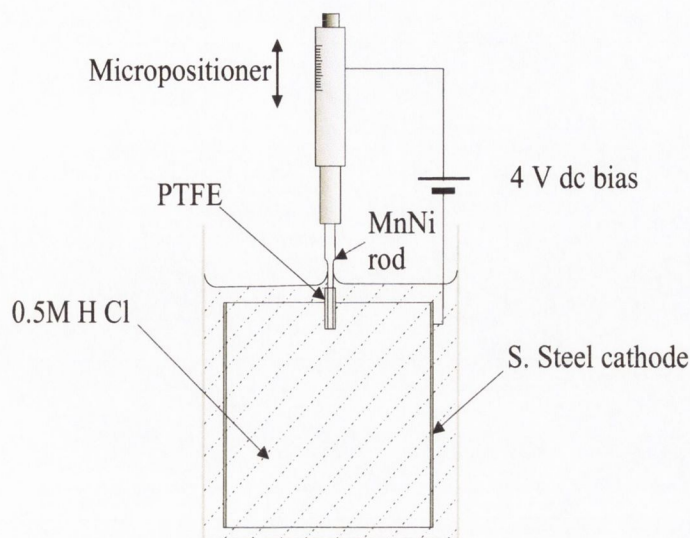
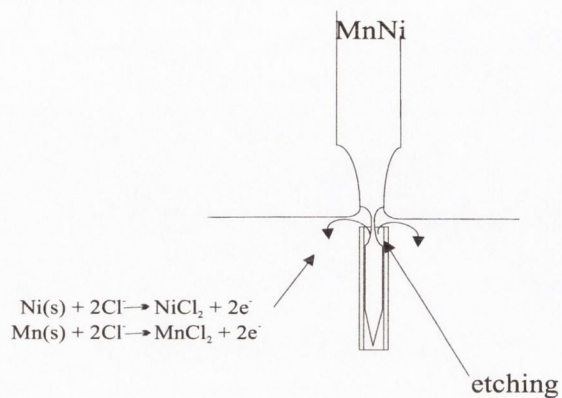


Figure 4.1: Electrochemical etching set up. A rod is partially covered with insulating PTFE tubing and dipped into a bath of 0.5M HCl etchant.

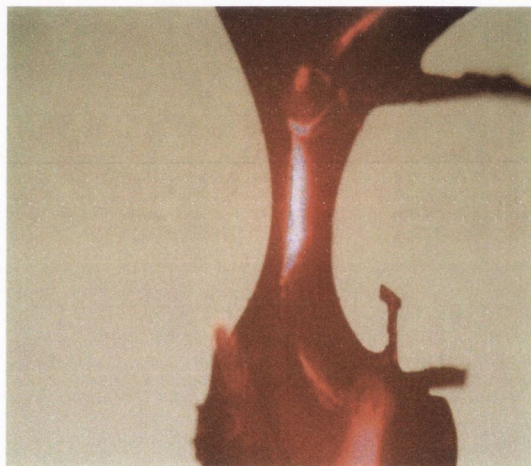
The etching process was interrupted prior to drop off the tip. An optical microscope manufactured by Zeiss Microscope Axiovert 25 was used (lens CP-ACHROMAT) to visualise the necking-in process.

When the cross-section of the thinned region becomes sufficiently small, it can no longer support the suspended weight of the lower wire portion and breaks, forming a nanometer-scale tip. The tip which falls to the bottom of the electrolyte bath is usually found to be sharper. Because the tip is formed inside the PTFE tube, it is protected when it falls to the bottom of the bath.

For etching, the circuit was typically biased with 4 V d.c., using an electronic shut off control circuit, which monitored the etching current and automatically closed the etching circuit when a pre-set reference value was reached. This value was calibrated to correspond to the typical current at which drop-off of a tip occurs. A stainless steel foil was used as the cathode in all the experiments. The tips were removed from the PTFE tube by inserting a needle into the opposite end of the tube. They were then rinsed with



(a)



(b)

Figure 4.2: a) Thinning or necking-in of the MnNi rod at the air/PTFE interface. The Mn and Ni are oxidised, leading to the formation of chloride compounds. b) Etching process of a Cr rod interrupted before dropping off. The PTFE tube is removed for the photograph. The thinning or necking in of the rod can be seen. $\times 10$ magnification.

distilled water, followed by a rinse with iso-propanol to remove contaminants. The tips were glued using UHV conductive glue into a custom tip holder and then loaded into the UHV system. Prior to use, they were ion etched with 0.5 - 2.0 keV Ar^+ ions (typically 10 minutes at 2 keV, followed by 10 minutes at 1 keV, and finally 5 minutes at 0.5 keV) to remove any oxide layer or contaminants that may have been produced during the electrochemical etching procedure.

MnNi tips were previously fabricated by a loop method, where the etchant was suspended by surface tension in a metal loop that forms the cathode [122, 123]. The technique described above improves upon the loop method by simplifying the preparation. Moreover, by creating a single air/electrolyte interface instead of the two present with the loop method, the tip aspect-ratio can be improved. The fact that the dropped-off tip is protected by the PTFE tubing is another advantage compared to the loop method, where the dropped-off tip may be retained in the etchant film and may be damaged by contact with the metal loop.

4.3 MnNi tips

4.3.1 MnNi alloy

The MnNi alloy has a CuAu-I type face centred tetragonal crystal structure, with lattice parameters $a = 3.740 \text{ \AA}$, $c = 3.524 \text{ \AA}$ [124,125]. This alloy is antiferromagnetic within a composition range of about $\pm 2\%$ of the equiatomic composition [126]. Neutron diffraction studies indicate that the Mn atoms have large magnetic moments ($\mu = 4.0 \pm 0.1\mu_B$) [124,127], although more recent theoretical calculations (Linearized muffin-tin orbital method combined with atomic sphere approximation, LMTO-ASA) based on local spin density functional theory have predicted smaller values ($\mu = 3.29\mu_B$) [125]. The magnetic moments of the Ni atoms are by comparison much smaller ($\mu \leq 0.6\mu_B$). The magnetic moments are antiferromagnetically aligned in planes that are normal to the crystallographic c -axis (see figure 4.3).

4.3.2 Tip preparation

A polycrystalline MnNi ingot was prepared by Dr David Fort (Metallurgy and Materials, University of Birmingham) by arc-melting equiatomic proportions of 99.9% pure Mn and Ni powder under an Argon atmosphere. Having melted the ingot 30-40 times to ensure homogeneity, it was then annealed for 48 hours at 900 °C under an inert Argon atmosphere. EDX analysis was performed on the sample, showing a 49.87 atomic-% of Mn. X-ray powder diffraction (at $\text{CuK}\alpha_1$ wavelength, corresponding to $\lambda = 1.541 \text{ \AA}$ was used) was carried out on a sample of the ingot to ensure that the correct crystallographic structure was obtained. The results are shown in Fig. 4.4. Cylindrical rods (0.5mm \times 13mm) of the material were then prepared by cutting the ingot with a low-speed diamond-wheel saw and polishing.

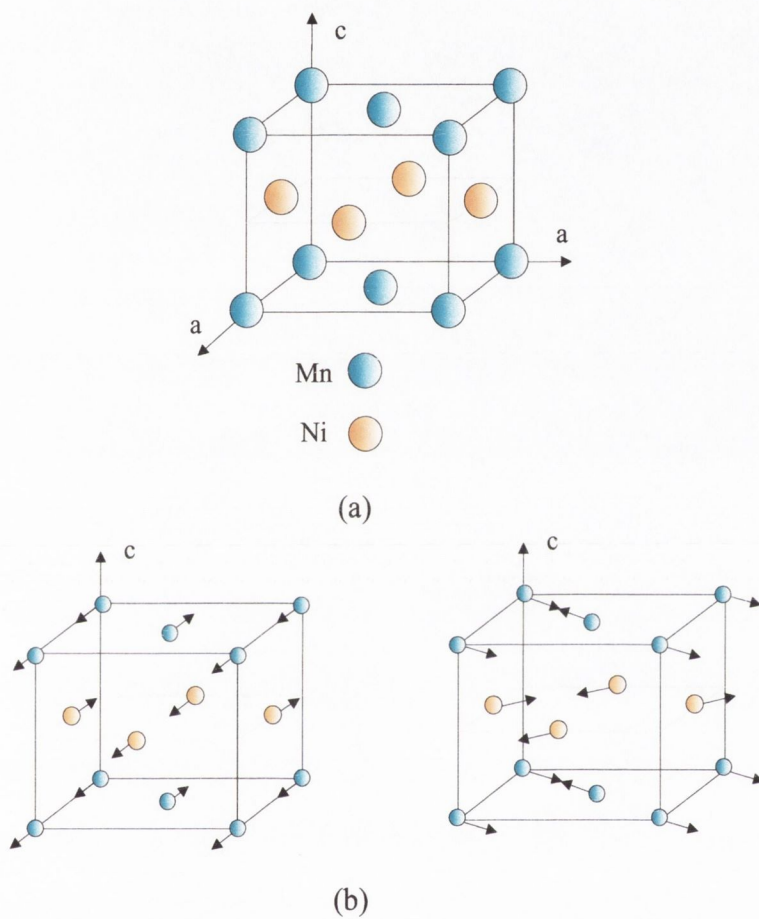


Figure 4.3: a) CuAu-I type face-centred tetragonal structure of equiatomic alloy. b) possible antiferromagnetic ordering configurations for this alloy. Reproduced from [127]

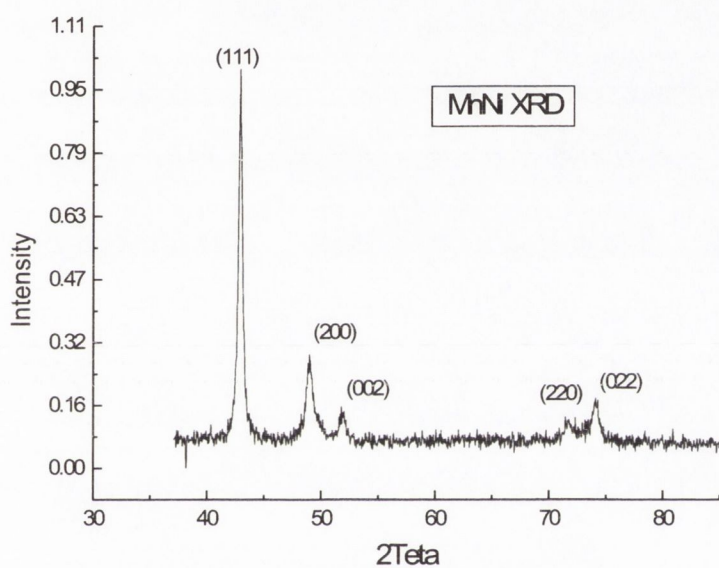


Figure 4.4: X-ray diffraction spectrum of a powdered sample of one of the MnNi ingots prepared. All the lines can be identified with the crystal structure of MnNi.

The rods were etched in an aqueous solution of 0.5 M HCl for approximately 6 minutes before drop-off occurred. Because the PTFE tubing used to restrict the etching region is positively buoyant in the solution, it was important that the weight of the dropped off tip exceeded the buoyancy caused by its protective PTFE tubing. Otherwise, the tip would float upwards just before drop-off, causing the tip to bend. However, it was observed that sharper tips were formed if the combined weight of the wire and PTFE tubing suspended in the electrolyte was reduced. Typically, a length of 2.5 mm of PTFE tube was found to give good results, producing tips with an apex of 50-100 nm. SEM images of an MnNi tip prepared in this fashion are shown in Fig. 4.5.

4.3.3 MnNi tips characterization

An important consideration when producing STM tips from alloy materials, is the effect of the preparation procedure on the local composition near the tip apex. Both electrochemical etching and ion etching of the tips may cause changes to the stoichiometry of the MnNi tips, resulting in Mn- or Ni-rich phases near the tip apex, which have quite different magnetic properties to the bulk material. While very little is known about the kinetics of the electrochemical reaction, it is possible that the removal rates of each element will differ. There will also be some dependence on the local crystalline structure at the tip apex. The grain size, orientation and density of grain boundaries, will all affect the removal rates. In order to obtain more information about the atomic composition and possible changes to the local magnetic properties at the apex of the tip, different surface and bulk studies have been carried out on a MnNi sample. The techniques used for this investigation are: Alternant gradient force magnetometer (AGFM), X-ray diffraction (XRD), Auger

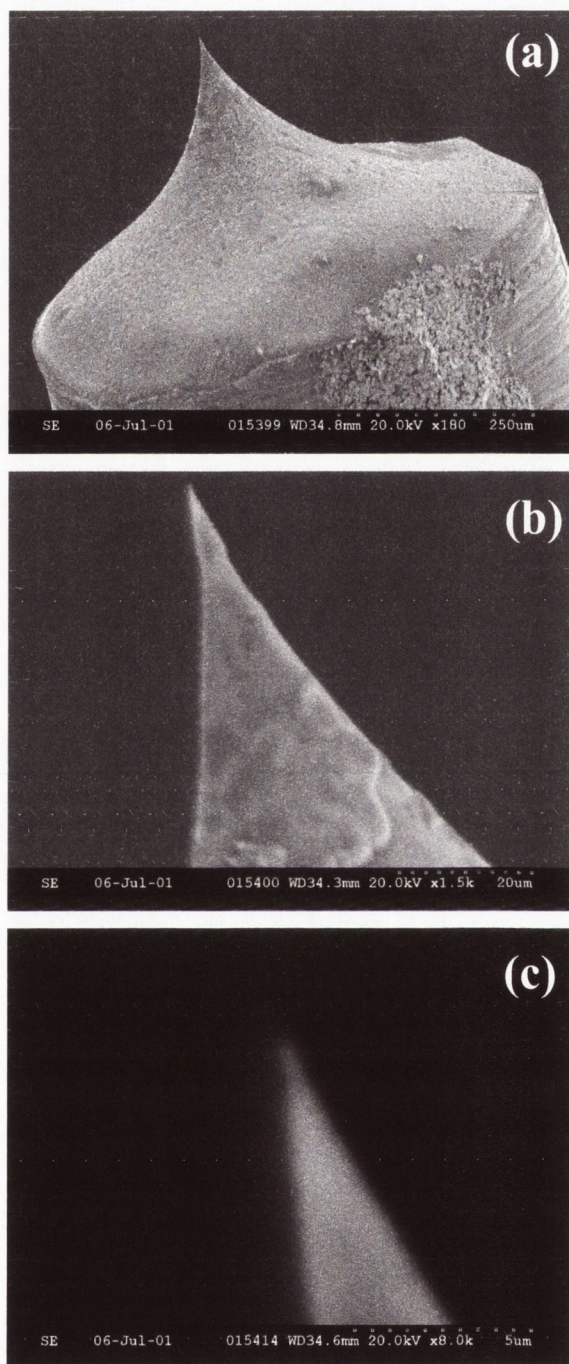


Figure 4.5: SEM images of a MnNi tip with (a) $\times 180$ magnification, showing the low aspect-ratio possible with the PTFE insulation. Some by-products of the etching process are visible on the tip. A 250 μm scale bar is indicated in the lower right-hand corner of the image. The sharpness of the tip apex is apparent in images (b) $\times 1.5\text{k}$ magnification; with a 20 μm scale and (c) $\times 8\text{k}$ magnification; with a 5 μm scale.

electron spectroscopy (AES) and Transmission electron microscope (TEM) and Scanning tunneling spectroscopy (STS).

Study of the effects of electrochemical etching: AGFM and XRD analysis

The alternating gradient force magnetometer (AGFM) is a highly sensitive tool particularly suited for thin film magnetometry. The measurement technique is based upon the alternating force generated on a magnetised sample by a set of field-gradient coils. The so-induced sample oscillation is directly proportional to the sample's magnetisation.

AGFM was used to study the effect of the electrochemical etching on the MnNi probes. Two flat MnNi samples were characterized, one electrochemically etched (sample A) under similar conditions as for a MnNi tip (cell/voltage/etchant concentration/etching time), and an unetched sample (sample B). The thickness and diameter of the samples were approximately 0.5 mm and 10 mm approximately. An AGFM unit, MicroMag (model 3200 VSM/AGFM) manufactured by Princeton Measurements Corporation was used. The magnetisation (emu) versus external magnetic field [$-10^3, 10^3$] (Oe) was recorded for the two samples in order to compare the magnetic susceptibility. The weight of sample B was 5.3 ± 0.5 mg and sample A was 1.8 ± 0.5 mg. In figure 4.6, the magnetic behavior for a paramagnet, diamagnet, antiferromagnet and ferrimagnet material is shown. For an antiferromagnetic material, no hysteresis loops are recorded and small values for the susceptibility are usually calculated ($\sim 10^{-4}$ - 10^{-6} emu/g).

Pal *et al.* [127] investigated the change in the susceptibility with temperature for different Mn based Cu-Au-I type alloys. A susceptibility value of $\sim 8 \cdot 10^{-6}$ emu/[Oe · g] at 300 K was found for the MnNi compound.

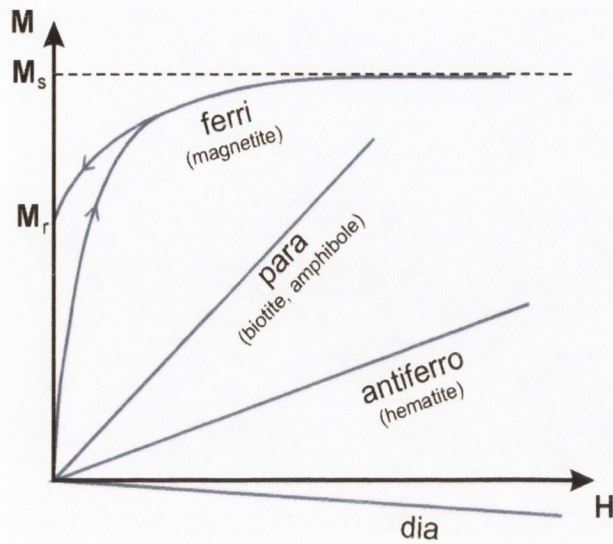


Figure 4.6: The general magnetic behaviour for magnetic materials is represented. Notice the small slope (susceptibility) for the antiferromagnetic alloys.

Magnetisation vs. external magnetic field was recorded for both samples (see figure 4.7). The magnetic susceptibility can be defined as, $k = M_{\text{saturation}}/H_{\text{external}}$.

A value of $1.24 \cdot 10^{-6}$ and $3.33 \cdot 10^{-6}$ emu/[Oe · g] for the magnetic susceptibility can be extracted from figure 4.7 for MnNi sample B and A respectively (There is a 3 % error on the values measured, coming from systematic and instrumental errors). Some conclusions can be extracted from these values. 1) There is a change of the value of the magnetic susceptibility due to the variation in composition caused by electrochemical etching. More Mn than Ni atoms are removed while electrochemically etching. The electrochemical etching process produces surface stress, reorganising the MnNi grain structure at the surface of the tips. This leads to a small increase in the magnetic susceptibility. 2) The value of the magnetic susceptibility of sample A is of the same order of magnitude as the one given by the

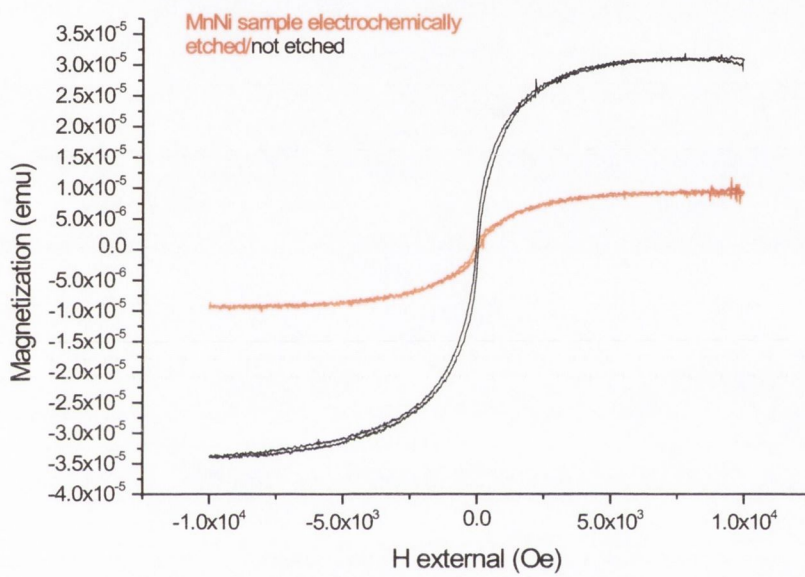


Figure 4.7: Comparison of M_{sample} vs. H_{external} for a MnNi sample (etched/not etched).

literature for a MnNi alloy [127] and is also comparable to that of sample B. We can conclude that the change of the susceptibility value is not large enough to change the magnetic properties of the MnNi samples due to preferential electrochemical etching. Some concern arises from the fact that in figure 4.7, a small hysteresis loop can be observed. This can be due to a small amount of impurities in the bulk sample introduced during fabrication or to a non ideal 50 Ni-50 Mn atomic percentage in the chemical composition of the sample.

In order to investigate the possible change of structure due to the electrochemical etching, X-ray measurements were taken on a flat MnNi etched/notched (A/B) samples (sample A, etched under the same conditions followed for the tip fabrication). The thickness and diameter of the samples were approximately ~ 1.0 mm and ~ 10.0 mm approximately. Sample A was rinsed with distilled water for chloride and oxides removal after electrochemical etching.

A $\text{CuK}\alpha_1$ wavelength, corresponding to $\lambda = 1.541$ Å was used. The XRD-depth penetration depends on the material to be analysed. For most metals a few μm penetration depth is estimated for this device. In order to compare A and B samples, we need to ensure that the etchant penetration into the sample is deeper than the XRD-depth penetration. Visual inspection of sample A after electrochemical etching shows an increase in roughness of the flat surface. The etchant penetration into the sample while etching was higher than XRD-depth penetration visually estimated. The XRD spectra obtained for sample B and A is represented in figure 4.8.

The position of the XRD-peaks remained the same, for sample A and B, as in figure 4.4. Therefore, the electrochemical etching does not change

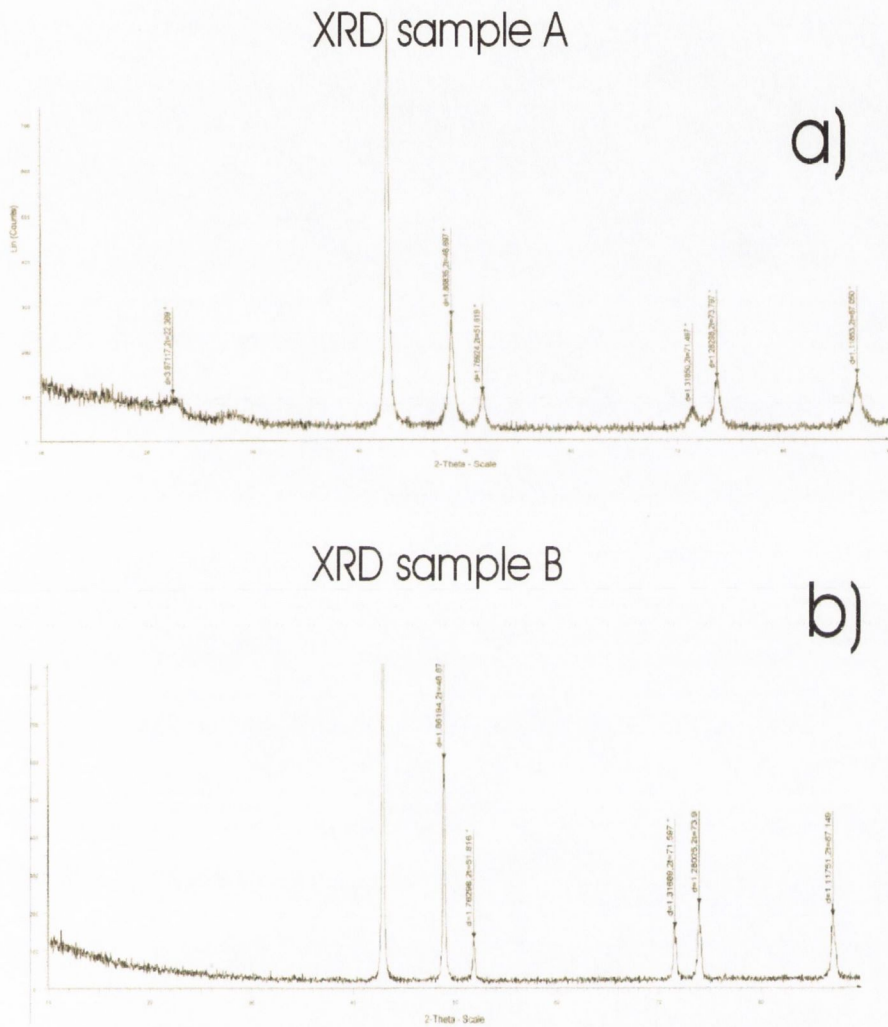


Figure 4.8: XRD spectra obtained for a MnNi sample not etched, B, and etched, A. A variation on the FWHM of the peaks of sample A compared to sample B is observed.

the structure, which remains tetragonal Cu-Au-I-type. While the XRD spectrum for sample A indicates a MnNi structure-type, a variation on the full width at half maximum (FWHM) of the peaks can be seen when compared to sample B in figure 4.8. The XRD-peaks for sample A have approximately twice the FWHM of those for sample B. This is produced as a result of the stress induced on the surface of sample A while etching. Since this measurement indicates that there is no change of structure, it could be suggested that despite the fact the electrochemical etching is a very aggressive procedure, a layer by layer removal occurs. In other words, the layer underneath cannot be removed until the layer on top has been fully etched.

It has been demonstrated how the MnNi crystallographic structure and magnetic properties slightly vary while electrochemical etching. This could be an indication to believe that MnNi tips keep their antiferromagnetic behavior.

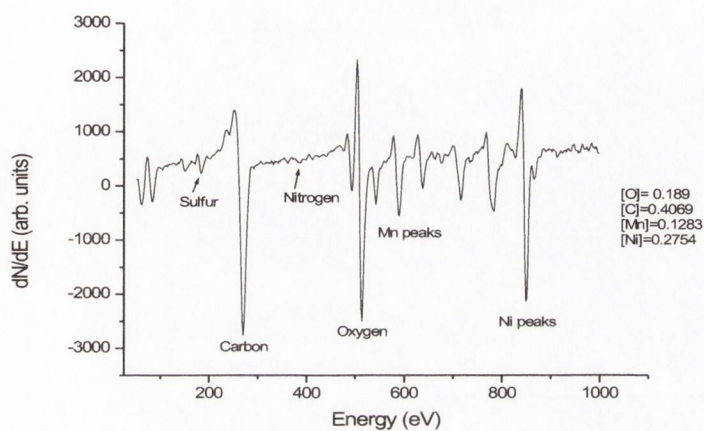
Study of the argon ion bombarding effect: AES composition analysis

The ion-etching procedure used in UHV to remove oxides and residues from the tip, may also subject the tip to some preferential sputtering since the sputtering yields for elemental Mn and Ni are different, being 2.88 and 2.03 respectively at 1 keV [128]. The sputtering rate has been separately calculated for pure elemental Mn and Ni, under the conditions used for the preparation of the MnNi tips. Elemental sputtering rates of 0.07 Å/sec for Ni and 0.1 Å/sec for Mn were calculated for ion-etching with 1 keV Ar⁺ ions at a fluence

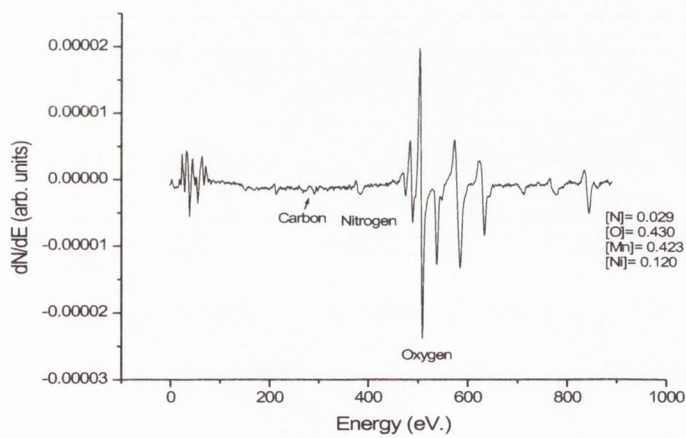
of 2.8×10^{17} ions/m²·sec. However, it is important to note that the sputtering yields for Mn and Ni in the MnNi alloy may differ from the elemental values and so a calculation of the elemental sputtering rates may be misleading.

To investigate the impact of ion etching on stoichiometry, a polished flat sample was taken from the MnNi ingot and introduced into our UHV system. Figure 4.9 a) shows the AES spectrum for the MnNi sample. Traces of N (370 eV), C (272 eV), S (150 eV) and O (508 eV) are present on the surface. As a result, the Mn/Ni ratio does not correspond to the expected equiatomic composition. As a first attempt to obtain a clean and a smoother MnNi surface for the analysis of the Ar⁺ etching effect, the MnNi sample was annealed for a period of 30 h. at 900 K \pm 50 K. Contaminants such as N, C and S are significantly reduced after annealing at high temperatures [7,9,47]. An AES spectrum of the sample post-annealing can be found in figure 4.9 b). A small amount of N and C are detected but the concentration of O has dramatically increased.

A second sample was introduced then into the UHV chamber. AES was performed after loading the sample, and a similar spectrum to the one obtained in figure 4.9 a), was recorded. The concentration of contaminants was reduced by Ar⁺ ion sputtering the MnNi surface for 2 seconds at 1 keV. Then, the sample was Ar⁺ etched at the same energy for another 15 and 45 seconds. The AES spectra showing the effect of 15, 45 sec. of Ar ion bombardment is shown in figure 4.10. A reduction of the concentration of contaminants such as C, N and O can be seen. The calculated values for the atomic ratio between Mn and Ni, $R[\text{Mn}/\text{Ni}]$, are 0.8383 and 0.550 for the 15 and 45 seconds of ion bombardment respectively. This means that there is a preferential sputtering of approximately 33 % faster for Mn than for Ni, as



(a)



(b)

Figure 4.9: AES analysis of a flat, polycrystalline MnNi sample; (a) before annealing (the sample is highly contaminated) and (b) after annealing for 30 h. in UHV at high temperatures. The concentrations of each elements are calculated on the right.

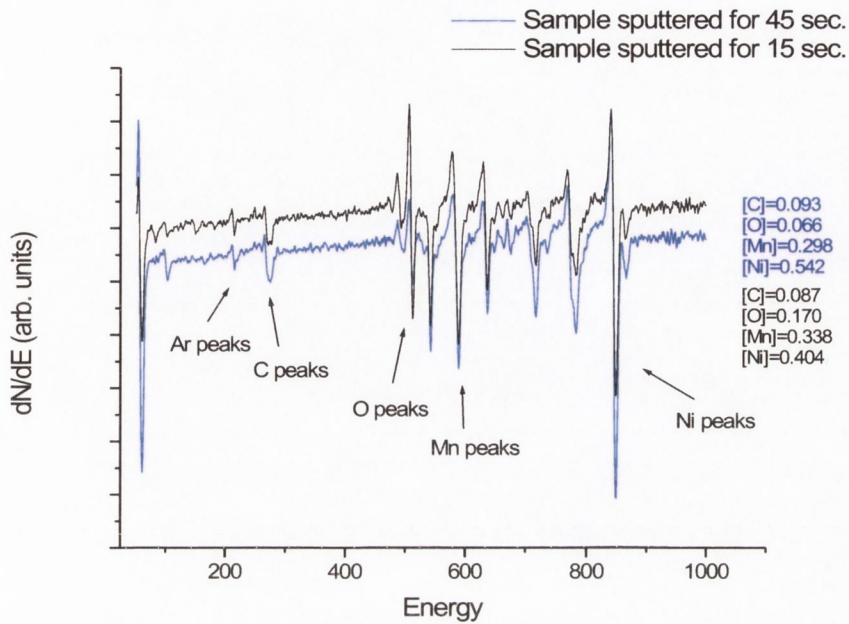


Figure 4.10: AES spectra of a flat, polycrystalline MnNi sample after 15 (black spectrum) and 45 sec. (blue spectrum); The concentrations of each element are calculated on the right. There is a reduction in the Mn/Ni signal ratio for the longest etched sample, indicating that there is preferential etching of the Mn component.

predicted by the theoretical sputtering yield values.

Convincing evidence has been provided that preferential sputtering of the Mn component occurs. This suggests that a (possibly ferromagnetic) Ni-rich phase may be produced on the surface of the tips. Also, the presence

of contaminants such as O and N coming from the bulk as a result of the annealing must be considered, as these may affect the composition and crystallographic structure of MnNi, thereby changing its magnetic properties. If the MnNi tip is off-stoichiometric as a consequence of the tip preparation and cleaning procedure, the antiferromagnetic order of the tips may be lost. However, it is probable that a thin ferromagnetic layer would still be produced on the surface of the tip, which would allow a spin-polarised tunneling effect to occur. It is even possible that the magnetisation direction of such a ferromagnetic layer would be pinned by the antiferromagnetic portion of the tip, in an analogous situation to that found in planar tunnel junctions.

A conclusive piece of evidence regarding the magnetic order of the apex of the tip could be given by the Lorentz Microscopy. In this technique a transmission electron microscope (TEM) maps the stray magnetic field near the sample surface by monitoring the interaction of transmitted electrons with the field ¹.

4.3.4 Magnetic contrast: Scanning tunneling spectroscopy (STS)

A cooperation experiment was carried out by the author in the University of Nijmegen (The Netherlands) under the supervision of Dr. T. Yamada, Dr. M. M. J. Bischoff and Prof. H. van Kempen. The growth of ultrathin Mn films on Fe (001) whisker at 370 K was investigated at room temperature by STS/STM with antiferromagnetic MnNi probes. In order to characterise

¹A collaboration project has been initiated with University of Glasgow, Department of Physics and Astronomy, Scotland, where the TEM technique is available. In order to find out more about the magnetic properties of the MnNi tips, a batch of Ar ion etched unetched tips have been sent to Dr. S. McVitie and Prof. JN Chapman to be analysed.

the magnetic properties of MnNi tips, STM/STS experiments were carried out on a magnetically characterised Mn/Fe(001) sample.

Previous work by this group has shown that the growth of Mn on Fe(001) at this temperature is believed to lead to flat films and low intermixing. AES and grazing ion-surface scattering measurements showed that the film morphology switches from layer-by-layer to layer-plus-island when a coverage of 3 monolayers (ML) is reached. Yamada *et al.* [17] reported the observation of a magnetic contrast of up to 10-20 % in scanning tunneling spectroscopy dI/dV maps obtained with Fe coated W tips (7 - 10 nm) on Mn layers (> 3 ML) grown on an Fe (001) whisker. They did not observe an alternating contrast in the dI/dV maps using W tips. Despite the fact that the magnetic dipole interaction between the sample and the tip is considerably reduced for ferromagnetic ultra-thin film coatings on a non-magnetic tip in comparison to thicker coatings or even bulk ferromagnetic tips, a remaining magnetostatic influence cannot be ruled out which might play an important role for magnetically soft or superparamagnetic samples. Although a quantitative analysis has not been performed yet, the influence of magnetic interactions on a magnetic surface was studied by Wulfhekel *et al.* [110, 111]. The effects of the stray field on the magnetisation of the Co(0001) surface was investigated with an Fe tip and it was concluded that these effects are not neglectible.

The Asymmetry term in the dI/dV curves was defined by:

$$A_{dI/dV/[T]} = \frac{dI/dV_{even} - dI/dV_{odd}}{dI/dV_{even} + dI/dV_{odd}}, \quad (4.1)$$

where dI/dV_{even} and dI/dV_{odd} are the dI/dV curves obtained for even

and odd layers. The asymmetry at positive voltages gives the sample polarisation multiplied by the tip polarisation at the Fermi level. If a 100 % polarisation is assumed for the sample surface states, the tip polarisation level can be found out. A minimum of 10 % tip polarisation was obtained using equation 4.1 with Fe coated W tips with perfect (anti)parallel tip sample magnetisation.

In order to learn more about the magnetic properties of the MnNi tips such as, 1) ability of MnNi probes to provide magnetic contrast and 2) magnetisation orientation of the apex of the tip, a well characterized surface of Mn layers (> 3 ML) grown on an Fe (001) whiskers was used as a test sample. MnNi tips were prepared following the preparation procedure described above. STM/STS measurements were performed in UHV at room temperature with a commercial STM (Omicron UHV STM-1).

To obtain a clean and flat substrate surface, a Fe(001) whisker, with dimensions $10 \times 2 \times 0.5 \text{ mm}^3$ was Ar ion sputtered, leading to a contaminant free substrate. STS measurements were performed by recording an $I(V)$ curve at every pixel of a topographic scan which is obtained at a typical set point of $V = 0.2\text{-}0.3 \text{ V}$ and $I = 0.5 \text{ nA}$. dI/dV profiles were obtained by numerical differentiation of the $I(V)$ curves and then divided by the T factor. STM image in figure 4.11 a) shows the stacking number of monolayers on Fe (001) scanned with a MnNi tip. Monolayers 2 and 3 have unique electronic properties and a different contrast on the dI/dV maps is expected. This contrast is due to two contributions, electronic and magnetic properties. The electronic properties of $ML > 3$ are the same but they are spin coupled antiferromagnetically in plane [17]. The dI/dV map can be found in figure 4.11 b). A difference in brightness between monolayers 4 and 5 can be observed. This

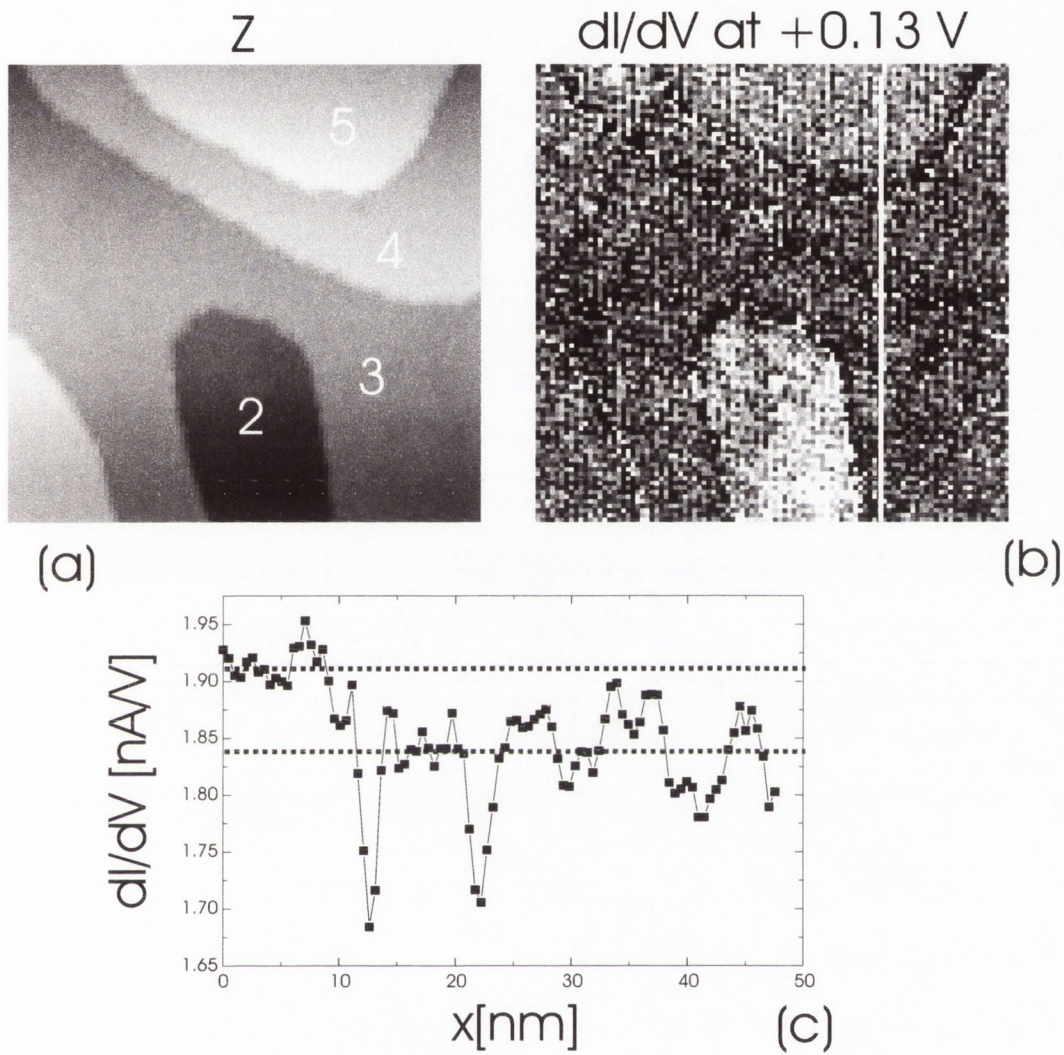


Figure 4.11: a) $(500 \times 500) \text{ \AA}^2$ STM image. Different stacking Mn layers are found. $V_s = 0.13$ and $I_t = 0.5$ nA taken with a MnNi tip. b) dI/dV map at 0.13 V measured at the same area as a). The difference in brightness level can be seen between terrace 4 and 5. c) dI/dV curve across the line profile in figure b).

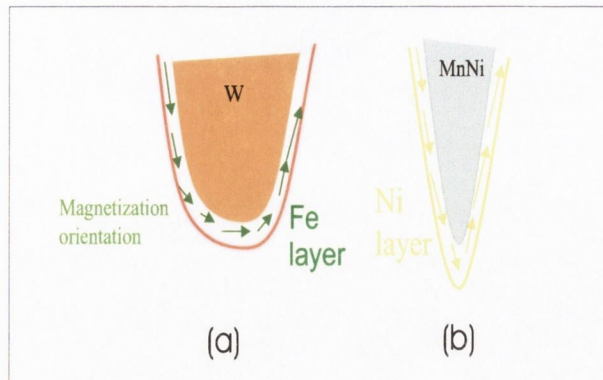


Figure 4.12: a) Fe/W blunt tips, the magnetisation orientation has been proved to be in-plane b) MnNi sharp tips, the magnetisation orientation is sketched out of plane.

is attributed to a magnetic contrast difference between the dI/dV signals. Using the asymmetry term defined in equation 4.1, a magnetic contrast value of $\sim 2\text{-}2.5\%$ was calculated from the line profile along the terraces (see figure 4.11 c)).

Blunt Fe/W tips can resolve the in-plane magnetisation of the surface of Mn/Fe(001) as shown by [17]. The tip geometry of the Fe/W tips used by Bischoff *et al.* is sketched in figure 4.12 a) ($\sim \phi_{apex} = 400\text{-}800$ nm). It has been illustrated how the magnetisation orientation for the tip lies in-plane. The preparation conditions, as well as the geometry, are responsible for this. Bischoff *et al.* were interested in magnetically resolving the terraces at a *nanometer scale*, whereas we are interested in using the MnNi tips for atomically resolved SP-STM.

Another aspect to discuss is the polarisation of the tip. The magnetic contrast is proportional to $P_{sample}(E_f + V) \cdot P_{tip}(E_f) \cdot \cos(B)$ where P is the sample(tip) polarisation at an applied Voltage V and B is the angle between polarisation directions. If B is not close to 0 or 180° the contrast is

reduced, but also if P_{tip} is low the contrast is reduced. For Fe, the polarisation level is about 43 % at the Fermi level [129]. Assuming that the apex of the MnNi tips has a thin Ni covering layer (as discussed in section 4.3.4), it would be interesting to know the level of polarisation of Ni, i.e. if Ni has a much lower polarisation this could lead to a lower magnetic contrast. Measurements of spin polarisation for different materials is given by reference [119,129,130]. The polarisation at the Fermi level for magnetite and Ni was found to be 84 % and 42 %, respectively. Therefore, the consideration of MnNi as having a lower polarisation at the Fermi level can be ruled out.

The presence of the Ni layer on the MnNi tips is sketched in figure 4.12 b). We have found that for MnNi tips, the magnetic contrast recorded in-plane is low. The fact that the shape of the tip ($\sim \phi_{apex} = 50-100$ nm) is different to that of the Fe/W tips, might affect the orientation of the local magnetisation orientation of the thin layers. The local magnetisation orientation may have a strong component oriented out of plane forced by the tip shape as drawn in figure 4.12 b).

A test sample to prove the latter assumption could be Fe films on Au(111). Between 0.5 and 3 ML the magnetisation of the Fe film is out of plane as demonstrated by polar magneto Kerr effect (PMOKE) and AGFM [131, 132]. If this is certain, MnNi tips could be ideal for magnetically resolving Bloch walls, step edges between terraces and samples with an out of plane magnetisation orientation at an *atomic level*.

4.4 Cr tips

The difficulties regarding composition, faced when attempting to fabricate tips from alloy materials, are removed when dealing with the elemental an-

tiferromagnet Cr. In this case, cylindrical rods were prepared from a high purity polycrystalline Cr ingot. The PTFE insulation method was used to electrochemically etch the tips in a 2 M NaOH solution. Again, sharp tips (50-100 nm tip apexes), with a low aspect ratio were obtained (Fig. 4.13). However the Néel temperature of this material makes it more suitable for experiments below room temperature.

4.5 Other tips

Fe, Ni and W tips were also produced, using $\phi = 0.5$ mm diameter commercial wire. An etchant solution of 2 M NaOH was used for the W tips, while 0.5 M HCl was used to prepare the Fe and Ni tips. The tip fabrication procedure was identical to the one described for Cr and MnNi and reproducibly sharp tips were obtained (Fig. 4.14).

4.6 STM results on magnetite (001) taken with a MnNi tip

Both Ni and MnNi tips have been used to obtain atomic resolution on the $\text{Fe}_3\text{O}_4(001)$ surface. MnNi tips have been used to resolve the atomic structure of the $(\sqrt{2} \times \sqrt{2})R45^\circ$ reconstruction of the clean $\text{Fe}_3\text{O}_4(001)$ surface. Figure 4.15 shows an atomically resolved image of the surface of $\text{Fe}_3\text{O}_4(001)$ obtained by Dr Guido Mariotto.

The corrugation along the rows alternates between bright points and dark points, where a ~ 0.2 Å corrugation was measured at the bright points, while a ~ 0.1 Å corrugation was measured at the darker points. The periodicity of the bright points along the [110] rows is ~ 12 Å and the

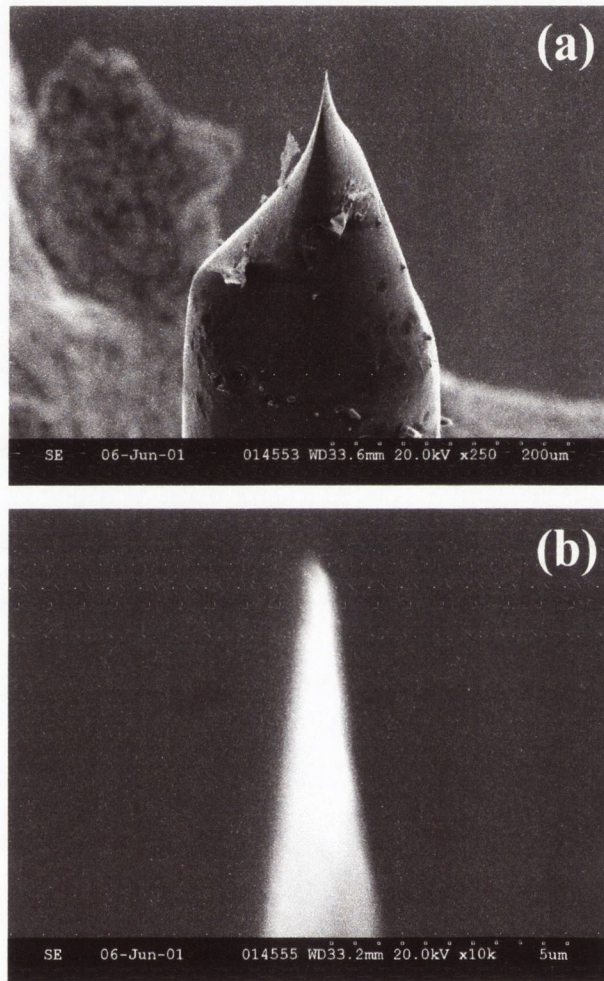


Figure 4.13: SEM images of an antiferromagnetic Cr tip with (a) $\times 250$ magnification and (b) $\times 10k$ magnification.

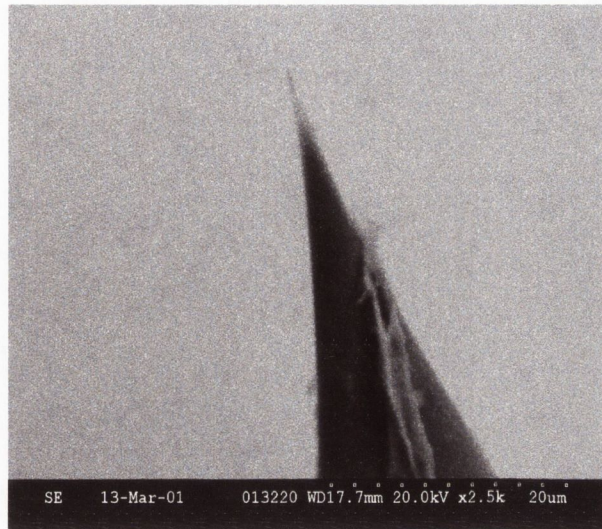


Figure 4.14: SEM image of a ferromagnetic Ni tip with $\times 2.5k$ magnification. The scale in the lower right corner of the image measures $20 \mu\text{m}$.

separation between bright and dark points is $\sim 6 \text{ \AA}$. The contrast in the STM images is attributed to the Fe^{2+} and Fe^{3+} ions at the B-sites. The variation of the tunneling current depends on m_s , which differs locally for Fe^{2+} and Fe^{3+} in magnetite being $4\mu_B$ and $5\mu_B$ respectively, making these ions distinguishable in STM images using a MnNi tip. This results may be interpreted as a possible spin-polarised effect [47].

Although further studies on the magnetisation of the MnNi tips are needed, it is clear that the tip fabrication, using the teflon tubing technique, improves the geometry (high aspect-ratio near the tip apex and low aspect-ratio away from the apex) of the tips compared to tips obtained by standard etching. Therefore these tips provide a more stable tunneling current due to a reduction of tip resonance during scanning.

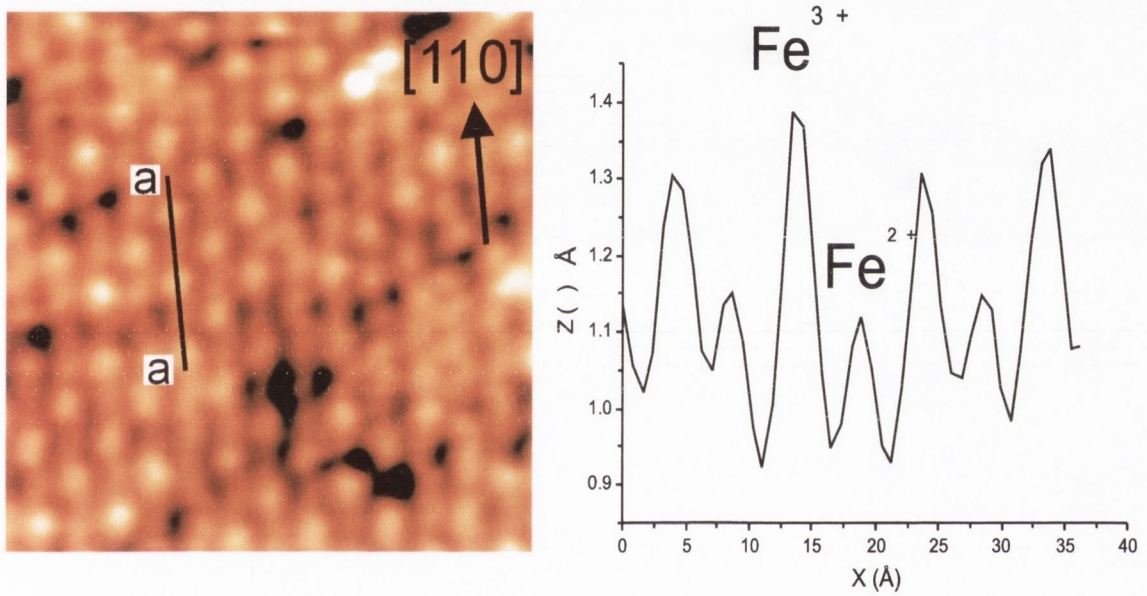


Figure 4.15: $65 \times 65 \text{ \AA}^2$ STM image of an synthetic Fe_3O_4 (001) single crystal. Taken with a MnNi tip, $I_t=1 \text{ nA}$, $V_b=1.0 \text{ V}$. a-a line profile taken along the [110] direction. Reproduced from [133]

4.7 Conclusions

STM tips have been electrochemically etched from both antiferromagnetic and ferromagnetic materials, using a technique where the active etching region is physically restricted by a close-fitting section of teflon (PTFE) tubing. This technique produces sharp tips (typically 50-100 nm in diameter), with a low aspect ratio, making them very suitable for STM applications. Particular emphasis has been placed on the fabrication of tips from the antiferromagnetic materials Cr and MnNi, as it has been shown that these tips possess a number of advantages over ferromagnetic tips for spin-polarised STM applications. The implications of the tip preparation procedure on composition and magnetic order have been discussed for the MnNi binary alloy:

1. The effect of the electrochemically etching process on MnNi tips has been analysed by AGFM and XRD. No evidence of change of the crystal lattice or an alteration of the magnetic order of the tip has been found.
2. The effect of Ar-ion bombardment on the tips in UHV might change the composition of the apex due to a preferential sputtering as indicated by AES. It is suspected that a thin-layer of ferromagnetic Ni might be covering the apex of the tip. If this layer is present it also allows may also allow a spin-polarised tunneling effect to happen. SP-STs experiments on a Mn/Fe(001) sample have shown that the total magnetisation orientation at the apex of the tip has two components, in-plane and out-of-plane. A stronger out-of-plane component is suspected, although these results are not conclusive.
3. MnNi tips fabricated with the teflon technique provide a more stable

tunneling current due to a reduction of tip resonance during scanning compared to tips fabricated under a standard electrochemically technique.

It has also been demonstrated that MnNi tips are suitable for SP-STM experiments as first pointed by Minakov *et al.* [33]. MnNi tips have been used to obtain atomic resolution on the $\text{Fe}_3\text{O}_4(001)$ surface and for SP-STM [9,35].

Chapter 5

An atomic scale study of the clean $\text{Fe}_3\text{O}_4(001)$ surface

5.1 Introduction

In this chapter, the clean magnetite (001) surface is studied. A contaminant free magnetite surface exhibits a $(\sqrt{2} \times \sqrt{2})R45^\circ$ superlattice. A *B*-terminated surface has usually been observed after annealing the sample in an oxygen atmosphere. A novel preparation procedure which leads to a rare co-existing *A* and *B*-surface termination after annealing the sample in a hydrogen atmosphere is described. A detailed analysis of the topography and nature of the *A*- and *B*- surface terminations of magnetite (001) has been given. The problem of the surface terminated on an *A* or *B* layer is addressed by means of chemical interaction of oxygen and hydrogen with the surface.

5.2 Sample preparation

A number of synthetic single crystals have been used in these experiments. The crystals were grown by Prof. Honig (Purdue University, Indiana) employing the skull melting technique. The experiments were carried out on crystals taken from the same ingot. The crystals were first characterized by powder x-ray diffraction. The diffraction patterns showed good agreement with the diffractograms for magnetite, and a lattice constant of $8.398 \pm 0.010 \text{ \AA}$ was measured. Four-point resistance vs. temperature measurements were also performed; A Verwey transition temperature of 108 K was found for the crystals [7]. The crystals were mechanically polished using diamond paste, with grain size down to 0.25 \mu m , before being introduced into the UHV system. The experiments were carried out in the UHV system described in section 3. STM measurements were carried out at room temperature in constant current mode. A bias voltage between +0.6 V and +1 V was applied to the sample and a tunneling current of between 0.1 nA and 0.3 nA was typically used [98]. MnNi tips have been used as probes in the STM experiments.

5.3 Surface preparation

We have developed two different *in-vacuum* preparation procedures to obtain a clean surface of magnetite (001). Both procedures lead to a contaminant-free surface as shown by the AES spectrum (see figure 5.1 a). The O(509 eV)/Fe(700 eV) ratio and the Fe $M_{2,3}VV$ peak shape of the AES spectra provide strong evidence that no iron oxide phase other than magnetite was present [10,134,135]. A typical LEED pattern of the surface is shown in figure 5.1 b). Satellite spots corresponding to a $(\sqrt{2} \times \sqrt{2})R45^\circ$ mesh are clearly visible. The reconstructed unit cell length is $a_{[100]} = 8.2 \pm 0.2 \text{ \AA}$. The $p(1 \times$

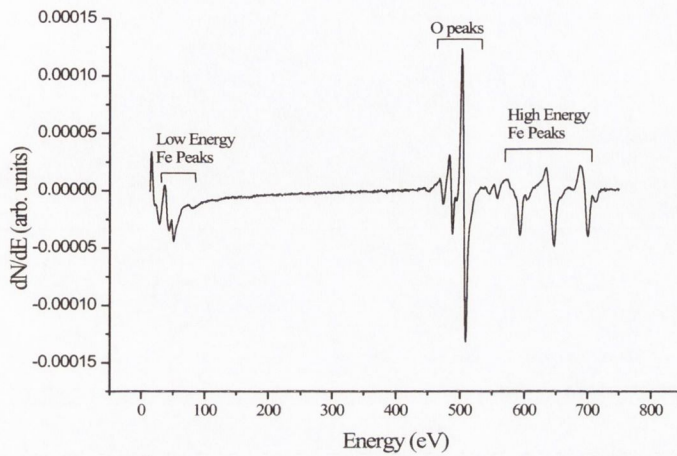
1) unit cell is marked with a white square and its unit cell is $a_{[110]} = 6.1 \pm 0.2 \text{ \AA}$. The $(\sqrt{2} \times \sqrt{2})R45^\circ$ superlattice was routinely reproduced following either of the preparation procedures described below.

1. The first sample preparation procedure consisted of annealing the crystals in UHV at $990 \pm 50 \text{ K}$ for long periods of time. According to our AES data, this has a two-fold effect of reducing the surface and causing segregation of impurities to the surface. The impurities were removed from the surface by Ar^+ sputtering for 10 minutes at 1 KeV ($I_{target} \sim 15\text{-}20 \mu\text{A}$). The crystals were then annealed in an oxygen partial pressure (the typical exposure varied between 3600 and 7200 Langmuir) to compensate for the reduction of the surface caused by the long UHV annealing. The crystals were finally annealed in UHV at the same temperature for short periods of time (typically 2 to 8 hours). It was found that this preparation procedure consistently led to a *B-terminated* surface [47].
2. The second preparation procedure is similar to the first one, with the exception of annealing the crystals in a hydrogen atmosphere (typical exposure of $\sim 2000\text{-}3000$ Langmuir) instead of in an oxygen atmosphere. This leads to co-existing *A-* and *B-* terminations.

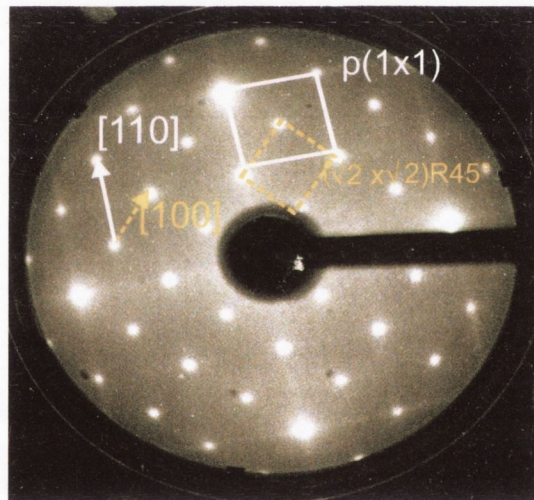
5.4 STM results and discussion

5.4.1 B- termination surface

After annealing the synthetic single crystal in an oxygen atmosphere followed by short periods of annealing in UHV, well defined terrace edges and a $(\sqrt{2} \times \sqrt{2})R45^\circ$ superlattice (see figure 5.2) were formed.



a)



b)

Figure 5.1: a) AES spectrum shows a contaminant-free magnetite (001) surface. b) LEED pattern of a clean Fe_3O_4 (001) surface taken with a primary electron energy of 78 eV. The $p(1 \times 1)$ unit cell and the $(\sqrt{2} \times \sqrt{2})R45^\circ$ superlattice are highlighted in white and yellow respectively.

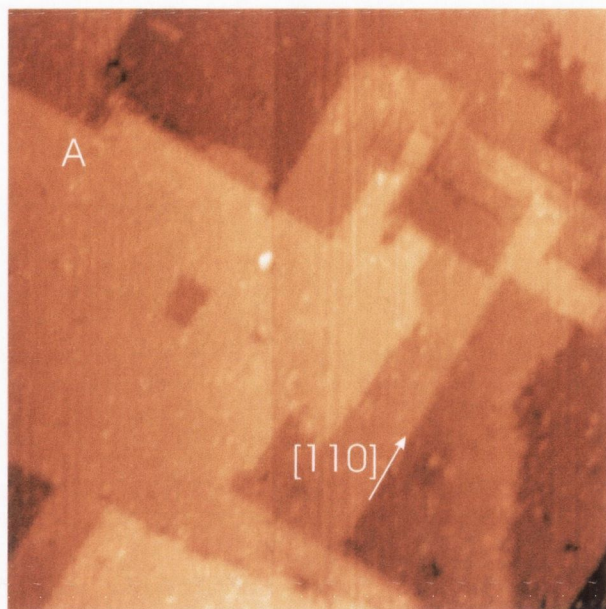


Figure 5.2: $(1000 \times 1000) \text{ \AA}^2$ STM image, $I_t=0.1 \text{ nA}$, $V_b=1 \text{ V}$ taken with a MnNi tip. A terraced surface was found after Ar^+ sputtering a synthetic single crystal followed by annealing it in an oxygen atmosphere (3600 L) and in UHV. The terrace edges are aligned along the $[110]$ and $[1\bar{1}0]$ directions.

A closer inspection of terrace marked as *A* in figure 5.2 shows an atomically resolved STM image of a B-terminated area (see figure 5.3). It was observed that neighboring terraces are separated by step heights that are multiples of $2.1 \pm 0.2 \text{ \AA}$, corresponding to the separation between $A - A$ or $B - B$ planes. Atomic rows are running along the terrace edges $[110]$ and $[1\bar{1}0]$ directions. A highly regular structure of a $12 \pm 1 \text{ \AA}$ periodicity along the $[110]$ direction is visible (see figure 5.3 b) and c)). Adjacent atomic rows are separated by $6 \pm 1 \text{ \AA}$. The primitive unit cell is marked with a black square in figure 5.3 b). A 90° rotation of the iron rows has been observed on neighboring terraces separated by 2.1 \AA . Therefore it can be concluded that the surface is terminated at a B plane.

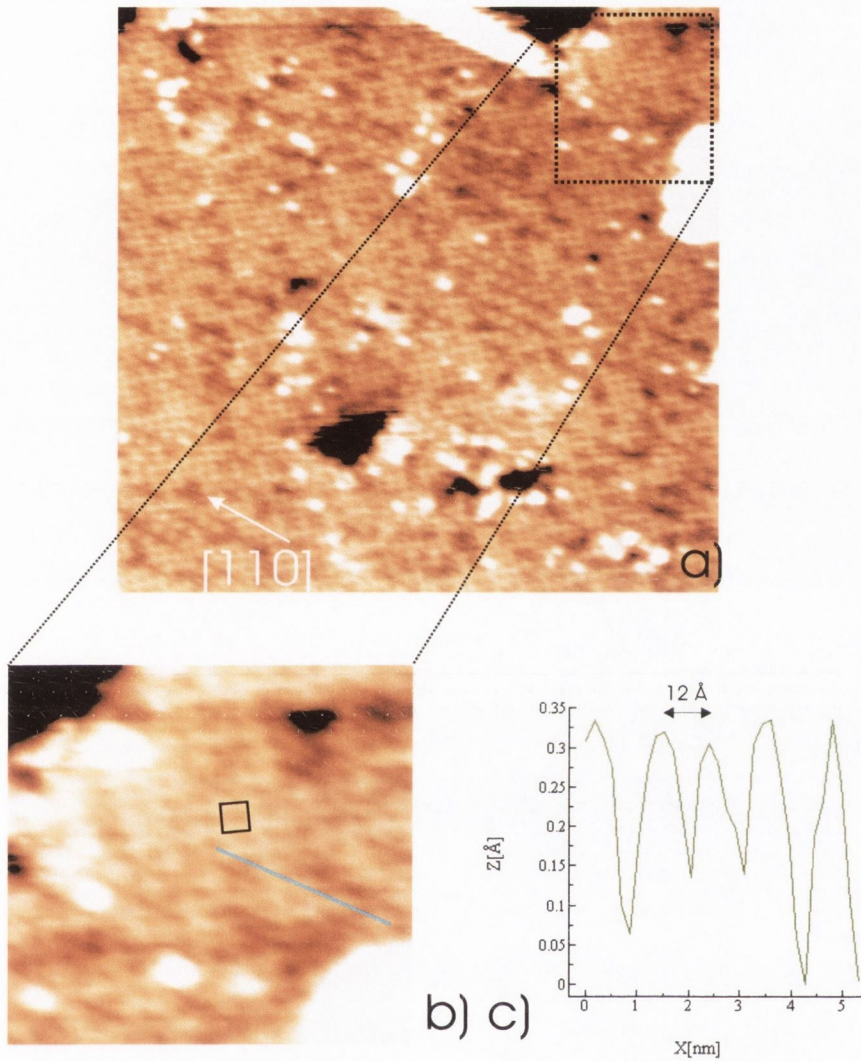


Figure 5.3: a) $(300 \times 300) \text{ \AA}^2$ STM image, $I_t=0.1 \text{ nA}$, $V_b=1 \text{ V}$ taken with a MnNi tip. Atomic rows are running along the $[110]$ and $[1\bar{1}0]$ directions. b) $(90 \times 90) \text{ \AA}^2$ zoom-in STM image. The $(\sqrt{2} \times \sqrt{2})R45^\circ$ primitive unit cell is marked with a black square. c) Line profile along the $[110]$ direction. The dimers are separated by a $12 \pm 1 \text{ \AA}$ periodicity.

This structure was found to extend over a length of the order of about 40-50 unit cells on terraces with average size of $(400 \times 400) - (500 \times 500) \text{ \AA}^2$, suggesting that not only a short-range order as suggested by *Anderson et al.* [136] but also medium and long-range order (LRO) had set in on the surface.

An extensive analysis of these results is given by Mariotto *et al.* [47]. There a $(\sqrt{2} \times \sqrt{2})R45^\circ$ superlattice observed by LEED and STM was attributed to an ordering of electron charges, with the formation of $Fe^{2+}-Fe^{2+}$ and $Fe^{3+}-Fe^{3+}$ dimers at the *B*-sites. It is emphasized that such long-range order is established at room temperature suggesting that the metal-insulator transition on the surface occurs at a temperature that is well above the bulk transition temperature T_V . Two possible mechanism that can lead to the formation of $Fe^{2+}-Fe^{2+}$ and $Fe^{3+}-Fe^{3+}$ dimers have been proposed.

One possible mechanism of formation of dimers is described by Jordan *et. al* [35]. It is claimed that a $(\sqrt{2} \times \sqrt{2})R45^\circ$ array of oxygen vacancies, results in the localization of the hopping electrons on neighboring Fe_{oct} sites and the formation of $Fe^{2+}-Fe^{2+}$ and $Fe^{3+}-Fe^{3+}$ dimers along the [110] oriented Fe rows. A second model has been also proposed by Shvets *et al.* [137] where dimerization of the Fe_{oct} ions is caused by an electron-lattice interaction. A deformation of the oxygen f.c.c. lattice leads to a dimerization of the Fe ions at the *B*-sites.

5.4.2 Co-existing A- and B- terminations

Co-existing *A*- and *B*- terminations were obtained by annealing the sample in a hydrogen atmosphere as described in section 5.3. Following this preparation

procedure, a rectangular terraced surface was found. A $\sim 1 \pm 0.1 \text{ \AA}$ step height has been measured between the terraces labelled 2 and 3 (as shown by the line profile in Fig. 5.4). An atomic step height of 1.05 \AA provides evidence of a both *A*- and *B*- terminated surface. An atomic resolution image taken on the terrace labelled "4" is shown in figure 5.5.

The white lines present in the side images in figure 5.5 denote missing rows along the $[110]$ and $[1\bar{1}0]$ directions. They are attributed to missing Fe cations. A 90° rows(vacancies) rotation is observed on the same terrace. The structure exhibits a four-fold symmetry, typical of a tetrahedrally terminated surface. Therefore, terraces 3 and 4 are terminated at the *A*-plane. By including these vacancies in the tetrahedral surface planes, they exhibit a similar reconstruction to the octahedral planes, and the $(\sqrt{2} \times \sqrt{2})R45^\circ$ unit cell marked by a white square is easily identified. Although the *A*- and *B*-planes exhibit similar reconstructions, the nature of the two reconstructions are intrinsically different. As explained at the beginning of this section, It is gathered substantial evidence to support the claim that the $(\sqrt{2} \times \sqrt{2})R45^\circ$ superlattice observed at the *B*-planes is due to the ordering of electron charges at the *B*-sites. This cannot be the case for a tetrahedrally terminated surface, since *A*-sites are occupied by Fe^{3+} cations only. The $(\sqrt{2} \times \sqrt{2})R45^\circ$ mesh observed on the *A*-plane surface was explained by Chambers *et al.* [54] as due to a missing Fe^{3+} cation per unit cell, which makes the magnetite surface electron balanced. Our results are in good agreement with this explanation. The $(\sqrt{2} \times \sqrt{2})R45^\circ$ reconstruction exhibited by the $\text{Fe}_3\text{O}_4(001)$ surface has been attributed by some groups to *A*-planes at the surface and by other groups to *B*-planes at the surface, leading to a certain degree of confusion. This is possibly due to the fact that the simultaneous presence of both terminations has been rarely observed on

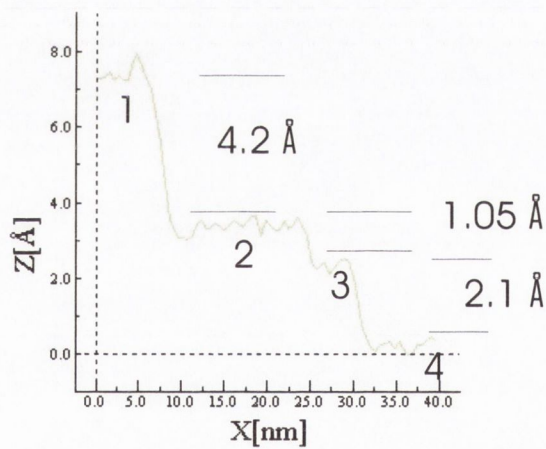
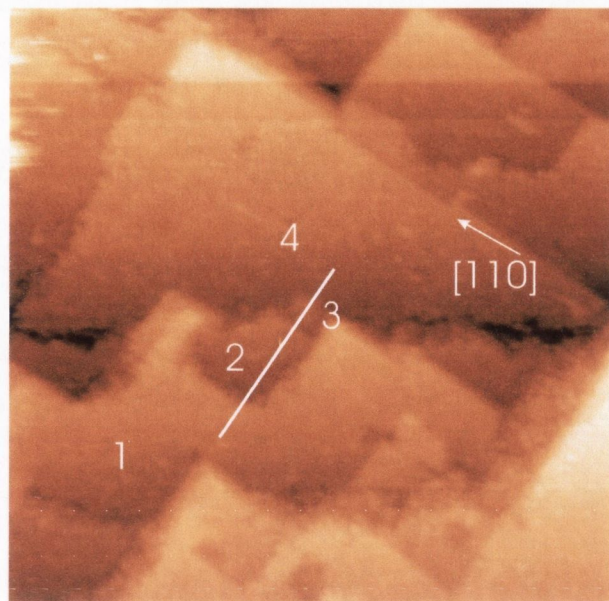


Figure 5.4: $(1100 \times 1100) \text{\AA}^2$ STM image, $I_t=0.1 \text{ nA}$, $V_b=1 \text{ V}$ taken with a MnNi tip. A line profile is taken along different terraces numbered from 1 to 4. Step heights of $2.10 \pm 0.2 \text{\AA}$ are present except for the separation between terraces 2-3 where the step height with the neighboring terrace is 1.05\AA .

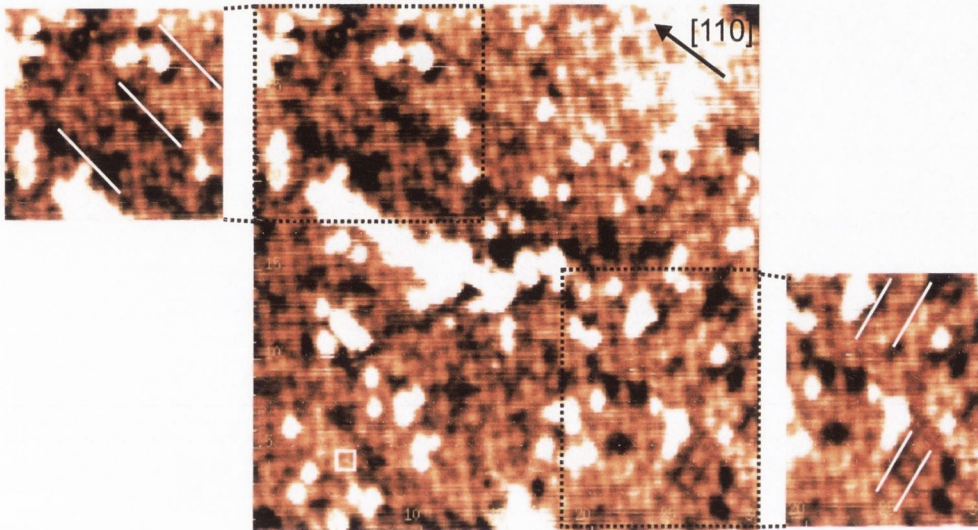


Figure 5.5: $(100 \times 100) \text{ \AA}^2$ STM image, $I_t=0.1 \text{ nA}$, $V_b=1 \text{ V}$ taken with a MnNi tip. Atomic rows run along the $[110]$ and $[1\bar{1}0]$. A white square in the lower right-hand corner denotes the $(\sqrt{2} \times \sqrt{2})R45^\circ$ primitive unit cell. Missing rows can be seen along both the $[110]$ and $[1\bar{1}0]$ directions on the same terrace and are indicated with white lines on the side images.

the surface of magnetite.

The first preparation procedure described in section 5.2 which consists of annealing a magnetite crystal in an oxygen atmosphere, followed by UHV annealing periods has been intensively studied in the last decade as explained in the introduction. This leads to a reorganization of the surface in order to minimise the surface energy leading to a B -terminated surface.

On the other hand, the interaction between magnetite (001) and other gases such as hydrogen has not been studied to any extent in the past. When the surface is exposed to a hydrogen atmosphere, oxygen is desorbed, leading to Fe_{oct} which can contain a maximum of 5 dangling bonds. As described in section 2.2.4, oxygen vacancies on the surface lead to a deficiency of electrons, which makes the surface less stable. Further annealing in UHV will produce a re-organisation of the surface to minimise its energy by means of desorbing those Fe_{oct} ions. The plane lying underneath the oxygen and Fe_{oct} ions is an A -layer, which then becomes visible. Since the exposure in hydrogen atmosphere was lower than the one in oxygen, it is possible that the exposure was not sufficient to create an A -termination layer but a co-existing A - and B -termination.

This was also discussed by Chambers *et al.* [54], they suggested that a more oxidized magnetite surface is most likely to show a B -termination as also suggested by Stanka *et al.* [56]. Even though molecular gases are known not very reactive with metallic surfaces, a small exposure in hydrogen or oxygen atmosphere may have a crucial effect on the surface termination when preparing the crystal of magnetite.

5.5 Conclusions

We have studied the (001) surface of synthetic Fe_3O_4 single crystals using a range of surface sensitive techniques. A detailed description of the preparation procedure leading to a contaminant-free magnetite surface is outlined.

A clean magnetite (001) surface usually exhibits a $(\sqrt{2} \times \sqrt{2})R45^\circ$ superlattice as observed by LEED and STM. This reconstruction was attributed to an ordering of electron charges, with the formation of $\text{Fe}^{2+}\text{-Fe}^{2+}$ and $\text{Fe}^{3+}\text{-Fe}^{3+}$ dimers at the B -sites. For a tetrahedrally terminated surface, the $(\sqrt{2} \times \sqrt{2})R45^\circ$ mesh observed on the A -plane surface has been explained by a missing Fe^{3+} cation per unit cell. This structure was found to extend over 40 unit cells on terraces suggesting that long-range order (LRO) had set in on the surface.

A possible mechanism to explain the controversial nature of the surface termination on magnetite has been proposed. It was found that the surface terminates at the B plane when annealed in oxygen partial pressure. A surface comprising co-existing A and B terminations was observed following mild anneal of the crystal in hydrogen partial pressure. Oxygen radicals are desorbed from some most top layers when reacting with hydrogen gas. This led to deficiency of electrons and hence a non-autocompensated surface. After further annealing of the crystal in UHV, the surface energy is minimised by losing Fe_{oct} cations. This explains why some A -layers are then visible on the surface.

The surface preparation plays a critical role in determining the surface termination of magnetite (001).

Chapter 6

An atomic scale study of the contaminated $\text{Fe}_3\text{O}_4(001)$ surface

6.1 Introduction

In this chapter, the diffusion of K, Ca and Mg atoms in Fe_3O_4 (magnetite) single crystals and $\text{Fe}_3\text{O}_4/\text{MgO}(001)$ have been studied. The onset of a self assembled pattern of rows and nanotrenches on the $\text{Fe}_3\text{O}_4(001)$ surface [8, 9, 138] induced by long annealing periods has also been analysed. We will show that segregation of K and Ca to the surface is induced by thermal diffusion *i.e.* via interstices in single crystals and thin films grown on MgO. Although K and Ca are present only in small concentrations, they play a crucial role in the formation of the surface of a magnetite crystal. This is due to the fact that K_{1-x} , Ca_{1-x} and Mg_{1-x} do not form spinel structures, as these ions are too large to fit into the interstitial sites between the oxygen anions. Therefore, they diffuse to the surface during the anneal of the crystals, causing the

appearance of self assembled structures. A detailed study of the topography and mechanism of self-assembly of contaminants on the magnetite surface at a nanometer and atomic scale is given.

6.2 Sample preparation

A set of magnetite synthetic and natural single crystals and thin films grown on MgO have been used in these experiments. The natural crystals were cut from the single crystalline nugget used by Tarrach *et al* [52], which originated from Zillertal, Austria. The crystals were aligned with a precision of $\pm 1^\circ$ with respect to the (001) plane and were oriented along the [010] direction. The synthetic crystals were those used in section 5.2.

The single crystals were characterized by powder x-ray diffraction as in section 5.2. The diffraction patterns showed good agreement with the reference spectra for magnetite and lattice constants of $8.398 \pm 0.010 \text{ \AA}$ and $8.406 \pm 0.010 \text{ \AA}$ were measured for the synthetic and natural crystals, respectively. Four-point resistance vs. temperature measurements were also performed; Verwey transition temperatures of 108 K and 98 K were measured for the synthetic and natural crystals respectively [7]. The crystals were mechanically polished as explained in section 5.2 and introduced into the UHV system. The experiments were carried out in the UHV system described in section 3.

A 70 nm Fe_3O_4 thin film was grown on (100) oriented MgO single crystal cleaved- and polished- substrates using an oxygen plasma assisted molecular beam epitaxy (MBE) system (DCA MBE M600, Finland). The MgO substrate was purchased from MTI Corporation [139]. The purity of the MgO

substrate is 99.95 %, with typical impurities of Ca, Al and Si at 40, 15 and 10 ppm respectively. The substrate was chemically cleaned before loading into the UHV-chamber and then cleaned in-situ at 600 °C in UHV for 1 hour (at a base pressure of $\sim 5 \cdot 10^{-10}$ Torr) followed by four hours in a $5 \cdot 10^{-5}$ Torr oxygen pressure. The growth of the Fe_3O_4 was carried out by electron beam evaporation of pure metallic Fe (purity of 99.999 %) in presence of free oxygen radicals generated by an ECR (Electron Cyclotron Resonance) plasma source [140] in an oxygen atmosphere at a base pressure of $5 \cdot 10^{-5}$ Torr.

Reflection high-energy electron diffraction (RHEED) intensity oscillations showed that the film was grown in a layer-by-layer mode (0.3 Å/s) and that it is epitaxial. From the symmetric (400/200) and asymmetric (622/311) Bragg reflections it can be shown that an in plane lattice constant of Fe_3O_4 thin film (0.8426 nm) is equal to twice the lattice constant of MgO substrate. The out of plane lattice constant is less than twice the difference between lattice constant of bulk Fe_3O_4 and MgO (0.8372 nm). The structural characterization of the $\text{Fe}_3\text{O}_4/\text{MgO}$ (001) was carried out using multi-crystal high-resolution x-ray diffractometer (HRXRD, Bede-D1, UK). It was revealed that the Fe_3O_4 film grows strained on the MgO substrate with a tetragonal distortion caused by the lattice mismatch of 0.344 %.

6.3 Contaminated $\text{Fe}_3\text{O}_4(001)$ surface

As explained in the introduction, annealing a single crystal of magnetite for extended periods in UHV (900 ± 50 K) resulted in the diffusion of contaminants from the bulk to the surface.

The most common contaminants for single crystals are Ca, K and S. The

K^+_{Tetr}	K^+_{Oct}	Ca^{+2}_{Oct}	Fe^{+2}_{Oct}	Fe^{+2}_{Oct}	Fe^{+3}_{Tetr}
151	152	114	92	78.5	63

Table 6.1: Ionic radii for different contaminants found on the surface of single crystals of magnetite. Values given in pm (10^{-12} meters units)

segregation mechanism for metallic systems can be explained in terms of the size accommodation model [141]. In this model, segregation is driven by the decrease in the elastic strain energy as solute atoms - either too big or too small - diffuse from the bulk and occupy an interface site with less strain. Table 6.1 shows the ionic radii for the typical contaminants found in single crystals of magnetite [142]. Ca and K have much larger ionic radii than Fe, therefore they are expected to segregate to the surface. These contaminants segregate (*i.e.* via interstices) through the bulk remaining on the most top layers. Some of them may be located not at the interface, but in some layers below. The new locations of these large ions at the interstices of the magnetite unit cells, will stress the top most layer of the surface. The strain created on the surface increases the surface energy, forcing the surface to undergo major changes to lower it. It is believed that the strain is relieved by the breaking of the long range $(\sqrt{2} \times \sqrt{2})R45^\circ$ order, which shifts towards $p(1 \times n)$ superlattices.

A series of $(\sqrt{2} \times \sqrt{2})R45^\circ$, $p(1 \times 1)$, $p(1 \times 2)$, $p(1 \times 3)$ and $p(1 \times 4)$ surface reconstructions have been observed with increasing concentrations of Ca and K on single crystals. These are summarized in figure 6.1.

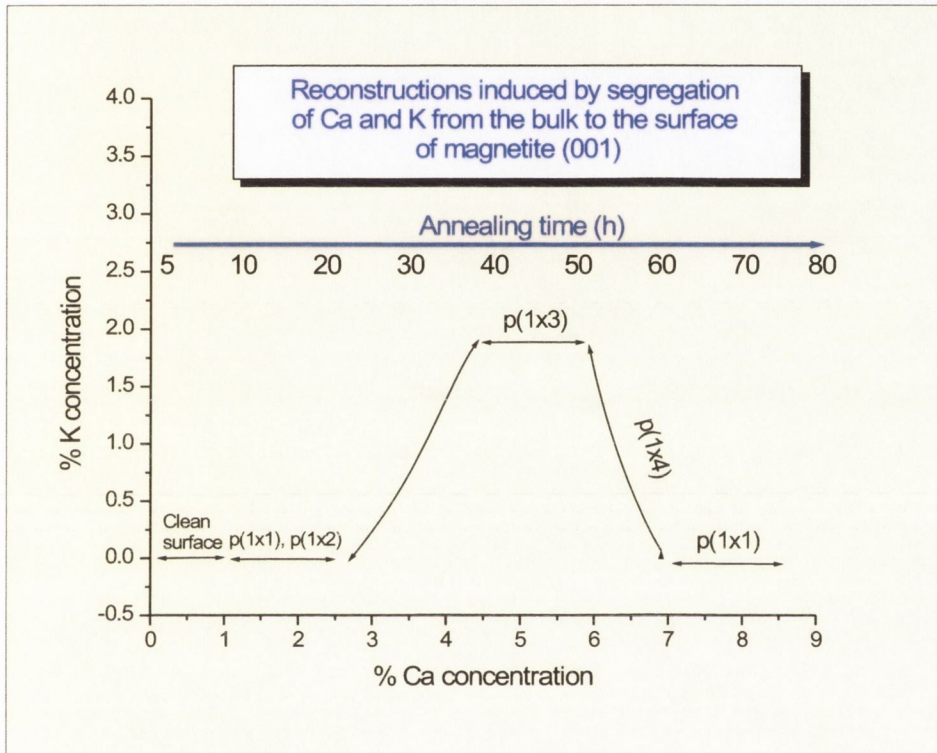


Figure 6.1: A series of $p(1 \times 1)$, $p(1 \times 2)$, $p(1 \times 3)$, $p(1 \times 4)$ surface reconstructions observed on the $\text{Fe}_3\text{O}_4(001)$ surface caused by the segregation of impurities from the bulk. The reconstructions are plotted as a function of the annealing time and of the Ca and K atomic concentrations.

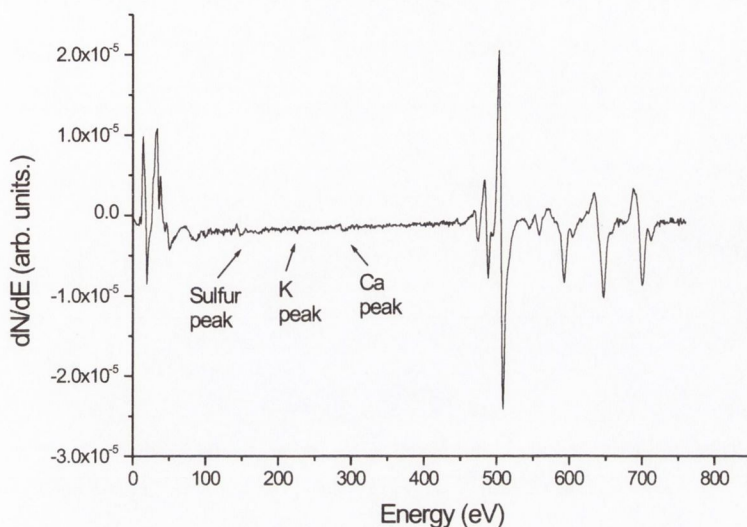


Figure 6.2: AES spectrum showing a low level of contaminants present on the surface

6.3.1 Breaking of long range $(\sqrt{2} \times \sqrt{2})R45^\circ$ order by the presence of contaminants

The same magnetite crystal as that used in section 5.4 has been used to performed these experiments. A $(\sqrt{2} \times \sqrt{2})R45^\circ$ surface reconstruction was obtained after following the preparation procedure described in 5.3 (annealing in a hydrogen atmosphere). Further annealing of the crystal (~ 6 h at 900 ± 50 K) resulted in some diffusion of contaminants. Sulphur, Potassium and Calcium were detected on the top most layers by AES (see figure 6.2). The atomic percentages in their concentration were found to be $S < 1\%$, $K < 1\%$ and $Ca < 1\%$. This level of contamination is very close to our AES detection limit. LEED showed blurred satellite spots indicating the presence of a $(\sqrt{2} \times \sqrt{2})R45^\circ$ surface reconstruction.

Figure 6.3 a) shows a $(500 \times 500) \text{ \AA}^2$ STM image of this surface.

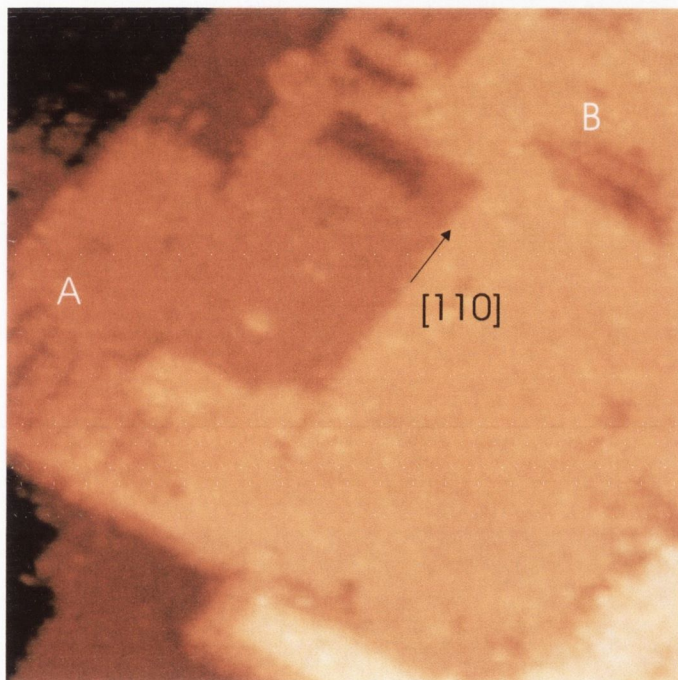


Figure 6.3: a) $(500 \times 500) \text{ \AA}^2$ STM image, $I_t=0.1 \text{ nA}$, $V_b=1 \text{ V}$ taken with a MnNi tip. The terraces *A* and *B* shows the onset of formation of trenches due to the annealing of the crystal in UHV.

The terraces *A* and *B* show the onset of formation of trenches due to the annealing of the crystal in UHV. The step height between terraces *A* and *B* is $2.1 \pm 0.2 \text{ \AA}$. A 90° rotation of the trenches is observed between the terraces, concluding that planes *A* and *B* have a two fold symmetry, typical of a octahedrally terminated surface. A short annealing of the crystal in UHV favors the creation of oxygen vacancies on the *B* layers and therefore the formation of missing iron rows. Missing oxygen and iron ions will result in the formation of trenches. The periodicity of these trenches varies from 20-30 \AA although an average of $24 \pm 2 \text{ \AA}$ was the most common value. A 24 \AA periodicity is identified with a $p(1 \times 4)$ superlattice on the surface. A zoom-in of areas *A* and *B* can be seen in figure 6.4 a) and b) respectively.

Atomic rows and trenches can be seen running along the $[110]$ and $[1\bar{1}0]$ directions in figure 6.4 a). A closer analysis of the atomic rows shows areas where no shift of bright spots on adjacent atomic rows is observed. A (1×1) square cell is marked in black. On the other hand, figure 6.4 b) shows that bright spots, marked with white squares, are not in-phase. This is typical of a $(\sqrt{2} \times \sqrt{2})R45^\circ$ -like reconstruction.

On other areas of the surface when contaminants have reached the surface, they start to nucleate on the edges of the terraces along the $[110]$ direction. Figure 6.5 a) shows an STM image where an onset of contaminants arrangement can be seen. The two rows of contaminants labeled as *A* and *B* labels in figure 6.5 b) are separated by $\sim 18 \pm 2 \text{ \AA}$ which is identified with a $p(1 \times 3)$ superlattice.

Although the surface is mainly covered with a $(\sqrt{2} \times \sqrt{2})R45^\circ$ -like reconstruction, similar to that found in section 5, one main difference can be highlighted: the more frequent presence of trenches on the surface. This leads to the appearance of a new set of surface reconstructions which breaks the

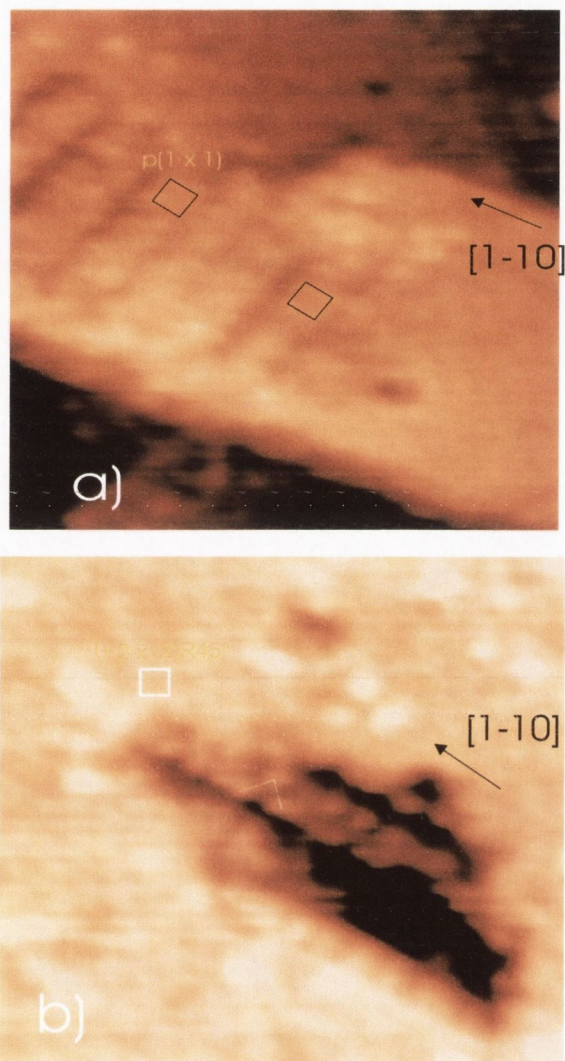


Figure 6.4: a) $(90 \times 80) \text{ \AA}^2$ STM image, $I_t=0.1 \text{ nA}$, $V_b=1 \text{ V}$ taken with a MnNi tip. Zoom-in on area A in figure 6.3. A $(6 \times 6) \text{ \AA}^2$ primitive unit cell corresponding to a $p(1 \times 1)$ reconstruction is marked with a black square. b) $(100 \times 90) \text{ \AA}^2$ STM image. The $(\sqrt{2} \times \sqrt{2})R45^\circ$ unit cell is marked with white squares.

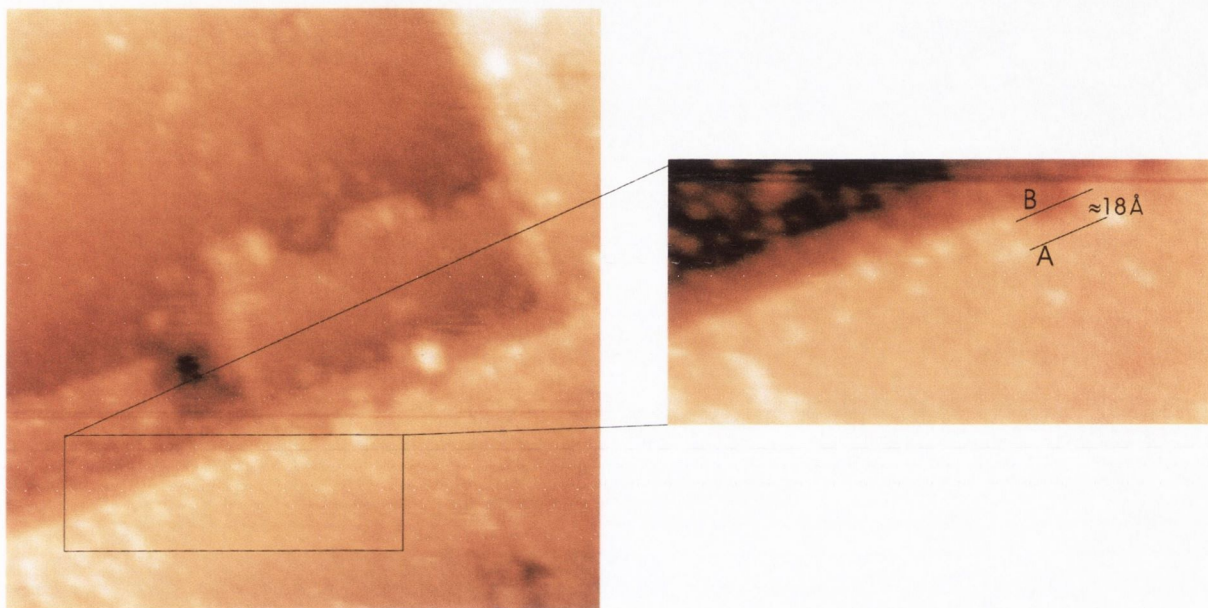


Figure 6.5: a) $(400 \times 400) \text{ \AA}^2$ STM image, $I_t=0.1 \text{ nA}$, $V_b=1 \text{ V}$ taken with a MnNi tip. The presence of contaminants at the edge of the terrace can be seen. b) $(200 \times 90) \text{ \AA}^2$ STM image, Zoom-in in figure 6.5 a). Labels A and B denote two rows of contaminants separated by $\sim 18 \pm 2 \text{ \AA}$. This is identified with a $p(1 \times 3)$ superlattice.

long range $(\sqrt{2} \times \sqrt{2})R45^\circ$ order.

As corroborated by AES and STM the only difference between the surface studied in section 5 and that of concern here is the presence of contaminants. Therefore the change of topography of the surface is just attributed to the increasing amount of impurities, as will be discussed in the following sections.

6.3.2 $p(1 \times 2)$ reconstruction

The annealing in UHV at $900 \pm 50^\circ C$ in UHV of a synthetic single crystal of magnetite (001) for 1-15 hours produced diffusion of Ca up to a concentration of 1.3 % (see figure 6.6 a)), while LEED analysis showed a streaked $p(1 \times 1)$ superlattice as can be seen in figure 6.6 b). The calculated unit cell along the $[110]$ direction is $5.8 \pm 0.2 \text{ \AA}$.

Figure 6.7 a) shows a $(800 \times 800) \text{ \AA}^2$ STM image taken with a ferromagnetic nickel tip showing a terraced surface. The terrace edges are aligned along the $[110]$ and $[1\bar{1}0]$ directions. The separations between successive like planes are multiples of $2.1 \times 0.2 \text{ \AA}$, suggesting that all terraces belong to an A or B type termination.

A zoom-in of figure 6.7 a) can be found in figure 6.7 b). The two successive planes are separated by $2.1 \pm 0.2 \text{ \AA}$. Two different surface rearrangements are marked with black lines a and b . Line a shows two rows of atoms running along the $[110]$ direction. An average corrugation of $\sim 0.2 \text{ \AA}$ along the bright spots is found. This value is equal to that measured on a clean magnetite (001) surface for Fe ions [8, 138]. A $(\sqrt{2} \times \sqrt{2})R45^\circ$ -like reconstruction can be seen. The line b shows bright spots in-phase. The primitive unit cell is identified with a $p(1 \times n)$ surface reconstruction.

It is also of interest to highlight the accumulation of clusters on the top terrace edge marked with line A . An analysis of the corrugation showed a \sim

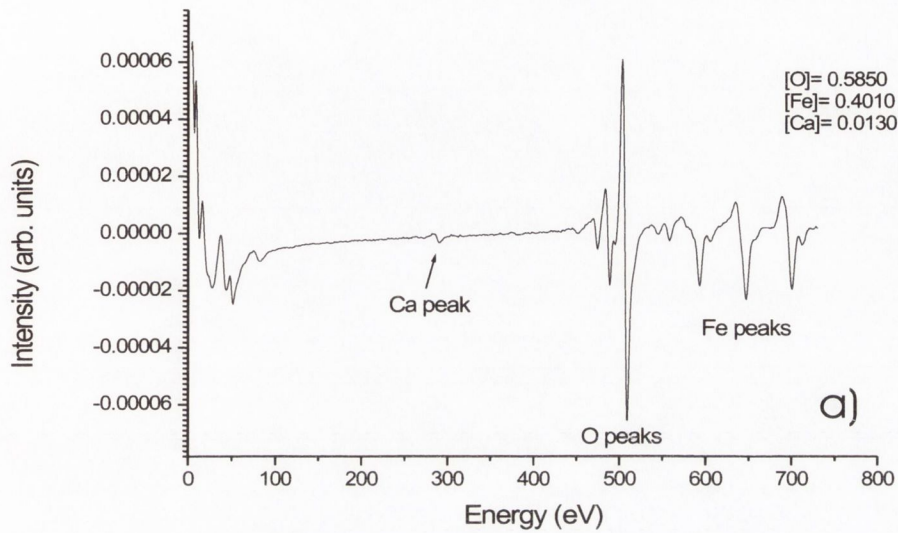


Figure 6.6: a) AES spectrum of low-level contaminated surface. 1.3 % of Ca has been found at the surface of the crystal. b) LEED pattern, taken with a primary electron energy of 90 eV, corresponding to a $p(1 \times 1)$ streaked superlattice, marked with a yellow square.

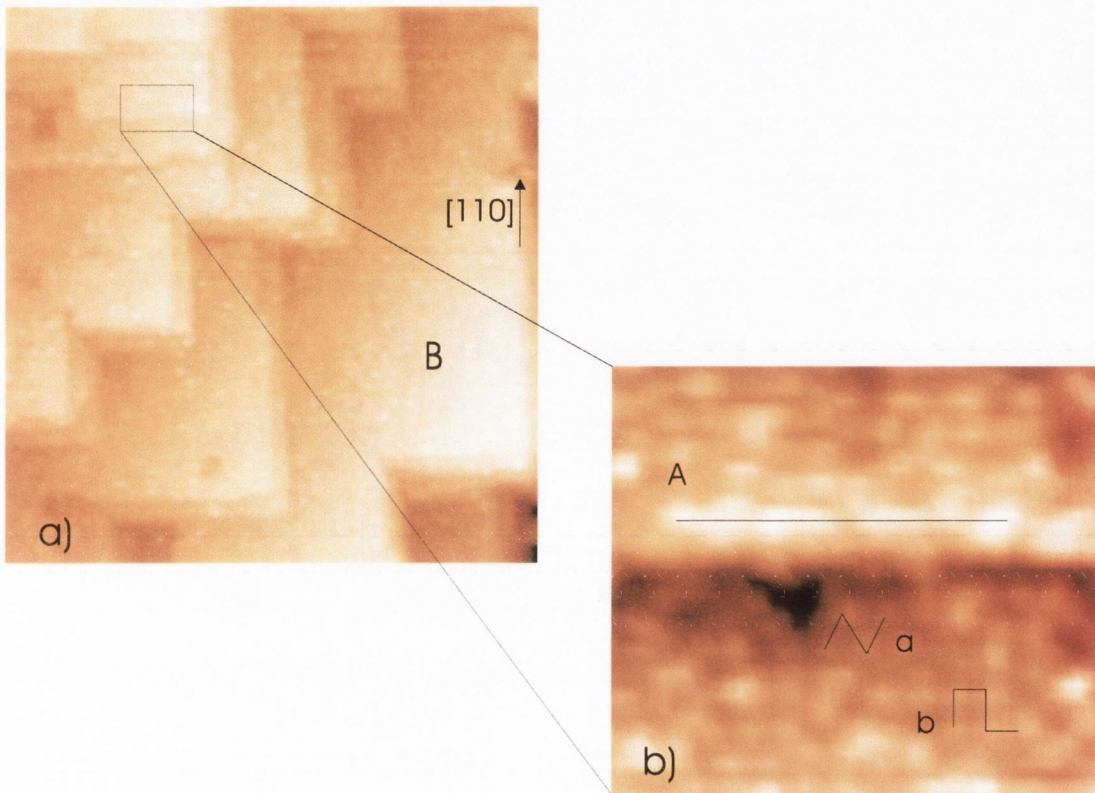


Figure 6.7: a) $(800 \times 800) \text{ \AA}^2$ STM image, $I_t=0.1 \text{ nA}$, $V_b=1 \text{ V}$ taken with a Ni tip. The neighboring terraces are separated by multiples of $2.1 \times 0.2 \text{ \AA}$. b) $(144 \times 122) \text{ \AA}^2$ zoom-in STM image. Two different surface rearrangements are marked with black lines *a* and *b*. Line *A* shows the accumulation of clusters of contaminants on the edge of the terrace.

0.4 Å value, which is approximately twice the value of the corrugation measured on rows of Fe ions. Therefore this features can be identified with Ca (see table 6.1). A shift on the $(\sqrt{2} \times \sqrt{2})R45^\circ$ surface reconstruction exhibited by a contaminant free surface towards a $p(1 \times n)$ has been produced due to the presence of Ca on the surface. Despite the fact that some $(\sqrt{2} \times \sqrt{2})R45^\circ$ -like reconstruction areas have been found, most of the surface is covered with a $p(1 \times n)$ superlattice.

Figure 6.8 a) is a (200×200) Å² zoom-in on the terrace marked as *B* in figure 6.7 a). Atomically resolved rows can be seen along the [110] direction. A closer inspection on these atomic rows can be found on image 6.8 b). A primitive unit cell of (12×6) Å² is marked with black square. This is identified with a $p(1 \times 2)$ surface reconstruction. Although whether the surface is terminated at an *A* or *B* plane can not be concluded from the corrugation analysis (line profiles marked as α in figure 6.8 c)), it can be concluded that two different species are present on the surface. An average corrugation of ~ 0.2 Å and 0.4 Å along the bright spots is found. Ca and Fe ions are identified with those exhibiting 0.4 Å and 0.2 Å corrugation respectively. This means that the Ca ions are replacing or nucleating on every second Fe ion along the [110] direction. This is shown in a schematic in figure 6.9 for an *A* or *B* termination surface.

As explained in chapter 2.5, the surface of magnetite (001) is a polar surface and is intrinsically unstable. Therefore, it needs to reconstruct to minimise the surface energy. The *electroncounting model* approach can be applied then to find out if the surface is autocompensated. The tetrahedral termination model is taken as an example. There are 1 Fe_{tetra} atom, 1 Ca^{2+} atom, 4 Fe_{oct} atoms and 4 oxygen atoms per unit cell. Each of the 1 Fe_{tetra} and Ca^{2+} atoms have 2 dangling bonds. These 4 bonds contain a total of (2

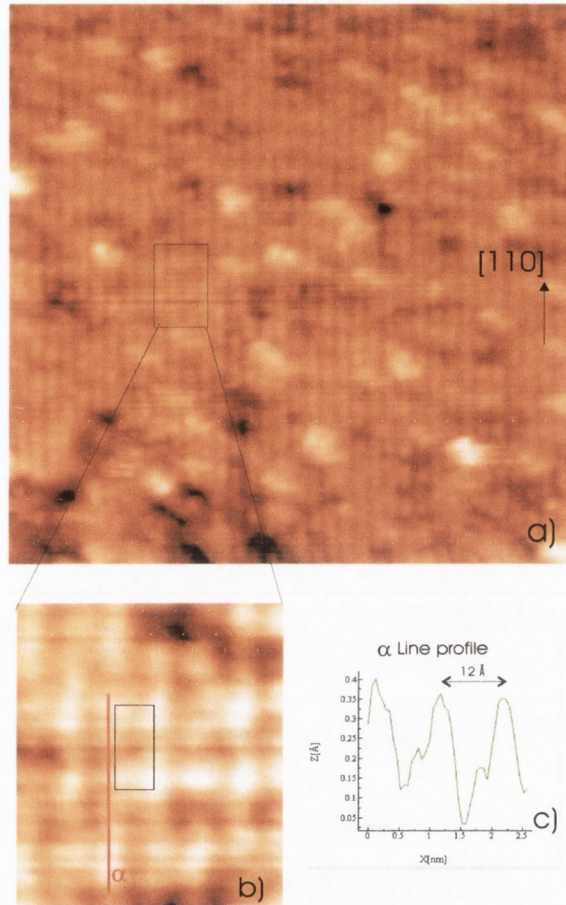


Figure 6.8: a) A $(200 \times 200) \text{ \AA}^2$ zoom-in STM image of terrace B in figure 6.7 a). Atomic rows have been imaged along the terrace edge on the $[110]$ direction. b) and c) $(36 \times 32) \text{ \AA}^2$ zoom-in STM image and its line profile along α line profile respectively. A $p(1 \times 2)$ surface reconstruction is marked with black square.

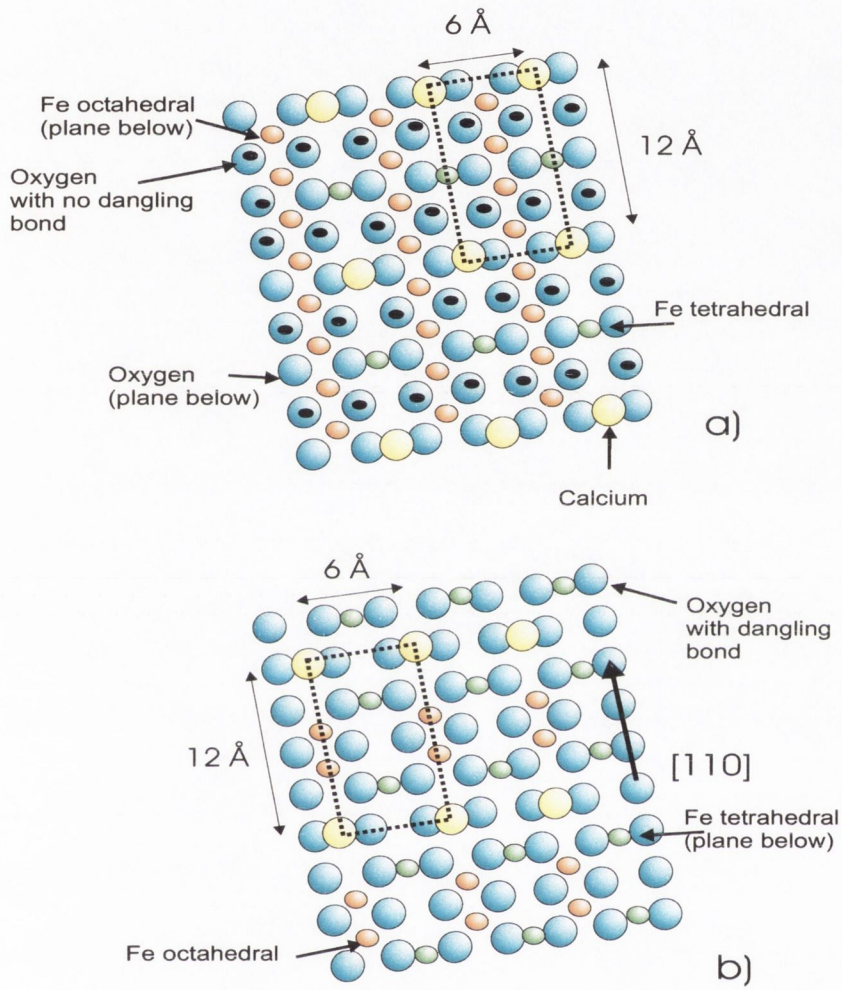


Figure 6.9: A schematic of the $p(1 \times 2)$ surface reconstruction. The Ca ions are replacing or nucleating on the Fe ions in the tetrahedral a), and octahedral b) coordination. The $p(1 \times 2)$ superlattice is marked by a dashed rectangle.

$\times 3/4) = 1.5 e^-$ and $(2 \times 1/2) = 1 e^-$. The 4 Fe_{oct} atoms have one dangling bond each; these 4 dangling bonds contain a total of $(4 \times 5/12) = 1.67 e^-$. The total number of e^- contained in the dangling bonds of the electropositive elements is $(1.5 + 1 + 1.67) = 4.17$. Each of the 4 O atoms has one broken bond to a Fe_{oct} . This means that the total number of e^- contained in the dangling bonds of the electronegative elements is $(4 \times 19/12) = 6.33$ instead of the $8 e^-$ required to completely fill the 4 bonds. That means that, to completely fill the anions dangling bonds a total of $(8 - 6.33) = 1.67 e^-$ can be transferred from the cations dangling bonds. $4.17 e^-$ were found on the dangling bonds of the electropositive elements. The electro balance of these figures means that an excess of $2.5 e^-$ is present on the surface. Following the same procedure, a deficiency of electrons is calculated for the octahedral terminated model. Both models proposed for the $p(1 \times 2)$ superlattice, makes the surface non-autocompensated, therefore it is a non-stable surface. These type of reconstruction has not been observed often and it will be replaced by other surface reconstructions by further annealing.

6.3.3 $p(1 \times 3)$ reconstruction

A different reconstruction was obtained when the Ca and K concentrations increased to $\sim 5.7\%$ and $\sim 1.5\%$, respectively after 30-40 h. of annealing at 900 ± 10 K. The corresponding Auger spectrum is shown in figure 6.10 a). A similar concentration of K and Ca was found for a $p(1 \times 4)$ surface reconstruction (see section 6.3.4), however contrary to the $p(1 \times 4)$ reconstruction no reduction of the surface was detected and the $[O/Fe]$ ratio was measured to be 1.3, in accordance with the value of a stoichiometric surface. Oxygen vacancies do not therefore play a role in the formation of a $p(1 \times 3)$ reconstruction, which is induced solely by diffusion of contaminants. The LEED

pattern displays fractional order spots along the $[110]$ and $[1\bar{1}0]$ directions. The fractional order spots are marked with white arrows and their separation is $1/3$ of the separation between the primary spots, which corresponds to a distance of $\sim 18 \pm 2 \text{ \AA}$ in real space.

Figure 6.11 a) shows a $(600 \times 600) \text{ \AA}^2$ zoom-in STM image taken with a W tip. The line profile *a* shows planes separated by multiples of $2.1 \pm 0.2 \text{ \AA}$ (see figure 6.11 b)). Atomic rows are visible along the $[110]$ and $[1\bar{1}0]$ directions. The rows are rotated by 90° on terraces separated by odd multiples of $2.1 \pm 0.2 \text{ \AA}$, which proves a *B*-plane terminated surface is imaged.

A zoom-in of these atomic rows can be seen in figure 6.12 a) and b).

The periodicity along these rows is $\sim 6 \pm 1 \text{ \AA}$, and adjacent rows are separated by $\sim 18 \pm 2 \text{ \AA}$. A $(6 \times 18) \text{ \AA}^2$ unit cell (marked with a black rectangle in figure 6.12 b)) is identified with a $p(1 \times 3)$ superlattice. From the studies of the clean $Fe_3O_4(001)$ surface presented in chapter 5, we conclude that the $p(1 \times 3)$ surface reconstruction is created by the diffusion of Ca and K to the surface. The diffusion of metals such as Ca or K ions from the bulk to the surface is explained in terms of the size accommodation model [141]. We have attributed the $p(1 \times 3)$ reconstruction to the segregation of either Ca and K ions, replacing every second Fe ion in octahedral coordination.

A schematic model of the reconstruction is shown in figure 6.13.

Using the *electron-counting model*, to fill O bonds with Fe_{oct} ions, each oxygen shares $(2-5/12) = 19/12 e^-$. To fill the bond with the Fe_{tetr} ions, the oxygen shares $(2-3/4) = 5/4 e^-$. In the case of a K^+ ion replacing an octahedrally co-ordinated Fe ion in the model proposed here for a $p(1 \times 3)$ surface reconstruction, the modified unit cell contains 5 Fe_{oct} atoms, 1 K_{oct} atoms and 12 O atoms. Following the same electron counting procedure as previously described, a $p(1 \times 3)$ reconstructed surface has a lack of $4.75 e^-$ /unit cell. A

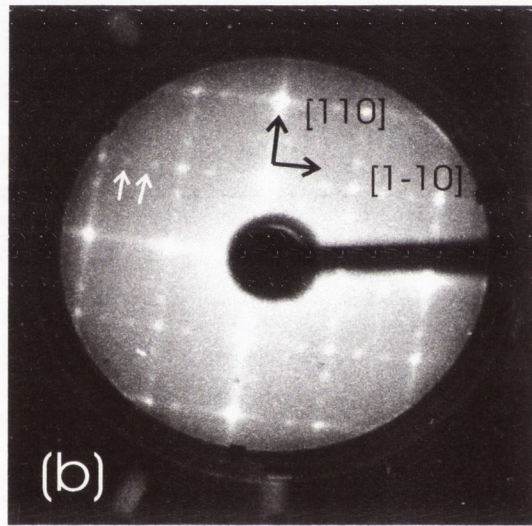
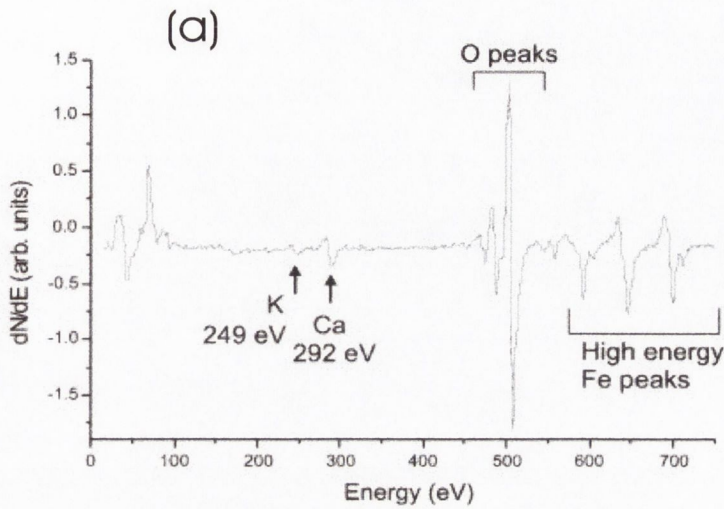


Figure 6.10: a) The presence of K and Ca contaminants on the surface can be clearly seen on the AES spectrum. A Ca peak at 292 eV and a K peak at 249 eV are visible, corresponding to a $\sim 5.7\%$ and $\sim 1.5\%$ concentration in the near surface layers, respectively. b) LEED pattern taken with a primary electron energy of 47 eV. Fractional order spots around the primary spots are clearly seen and marked with white arrows. Their separation is $1/3$ of that between the integral order spots.

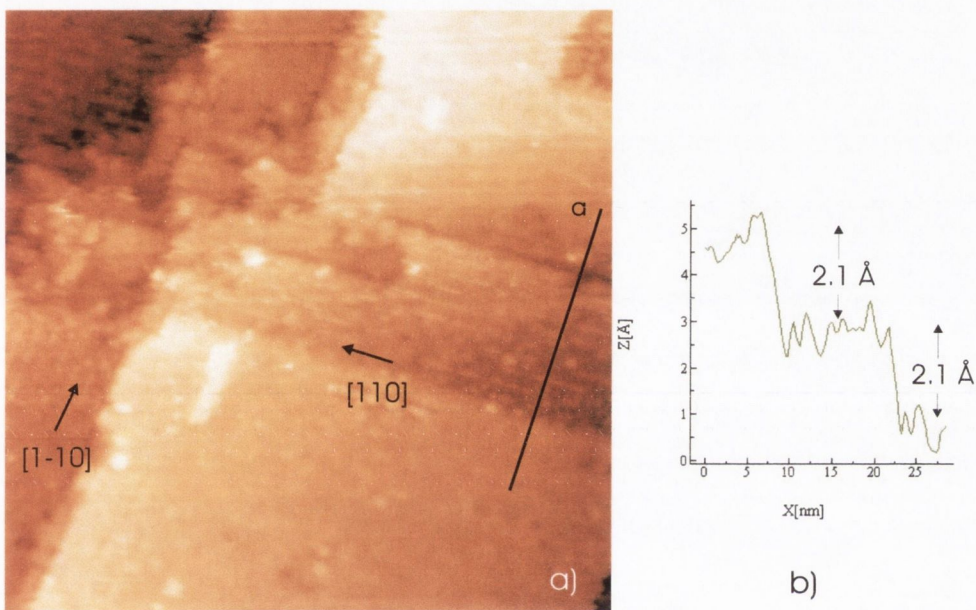


Figure 6.11: a) $(600 \times 600) \text{ \AA}^2$ STM image, $I_t=0.1 \text{ nA}$, $V_b=1 \text{ V}$ taken with a W tip. Atomic rows are visible along the $[110]$ and $[1\bar{1}0]$ directions. b) Line profile marked as a in a) shows step heights of 2.1 \AA between terraces.

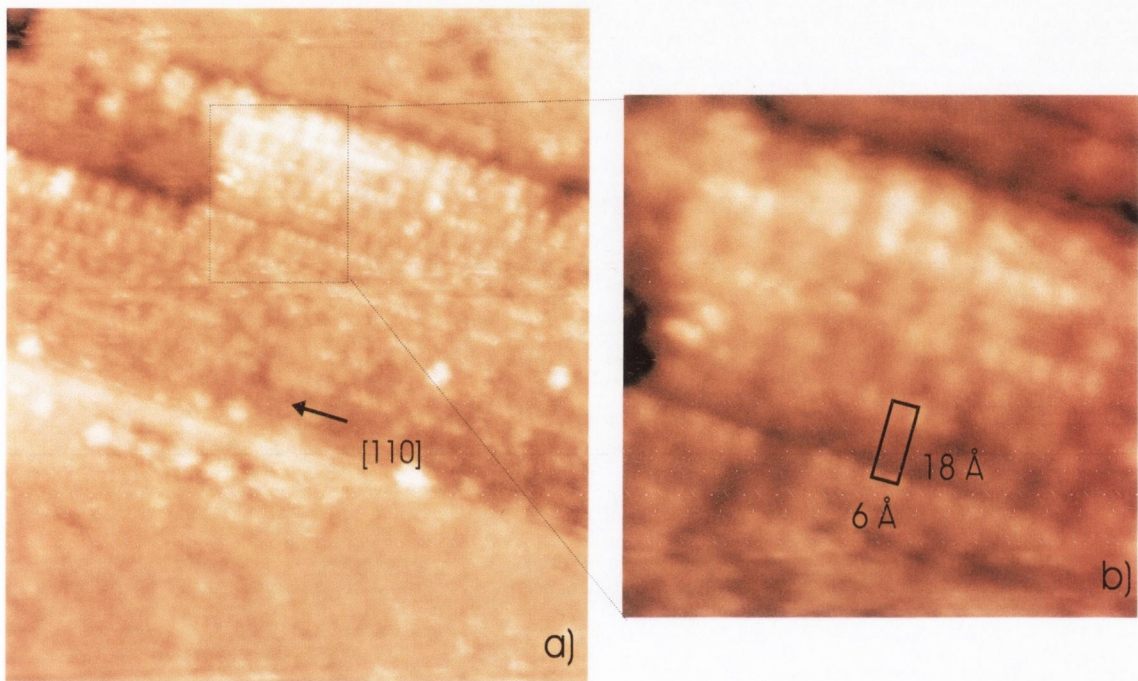


Figure 6.12: a) $(300 \times 300) \text{ \AA}^2$ STM image, $I_t=0.1 \text{ nA}$, $V_b=1 \text{ V}$ taken with a W tip. Atomic rows are running on the terrace edge along the $[110]$. b) $(109 \times 96) \text{ \AA}^2$ zoom-in STM image showing a periodicity of $\sim 6 \pm 1 \text{ \AA}$, and adjacent rows separated by $\sim 18 \pm 2 \text{ \AA}$.

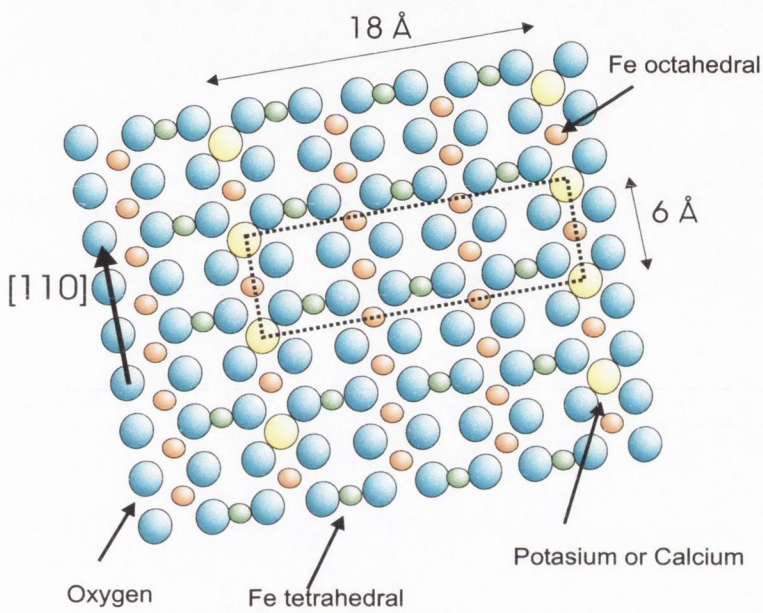


Figure 6.13: A schematic of the $p(1 \times 3)$ surface reconstruction. The Ca or K ions replace Fe ions in the octahedral coordination. The $p(1 \times 3)$ superlattice is marked by a dashed rectangle.

non-autocompensated surface is also found for the case of Ca^{+2} replacing an octahedrally co-ordinated Fe ion. These considerations indicate that a surface exhibiting a $p(1 \times 3)$ reconstruction is not expected to be a stable one, and our experimental evidence support this model by showing that it is a metastable state. A $p(1 \times 3)$ surface reconstruction was observed on only a few occasions and after further annealing was replaced by a different reconstruction.

6.3.4 $p(1 \times 4)$ surface reconstruction

Magnetite single crystals

For long annealing times of natural single crystals, metallic K is gradually desorbed from the surface due to its high vapour pressure [143]. The sub-surface layer tends to be depleted of this impurity thus reducing the rate of its surface segregation. Longer annealing times also reduce the O/Fe ratio at the surface which leads to the formation of a $p(1 \times 4)$ surface reconstruction. The typical O/Fe ratio for a clean surface exhibiting a $(\sqrt{2} \times \sqrt{2})R45^\circ$ reconstruction is 1.3, while our AES data showed O/Fe ranging from 1.1 to 0.8 as the annealing time increases. The decrease of the O/Fe ratio shows that oxygen vacancies are created at the surface, and correlates well with the increase in the number of trenches created on the surface. The LEED pattern recorded for this surface shows satellite spots between the primary spots. They are marked with white arrows in figure 6.14.

The fractional order spots have $1/4$ of the separation between the primary spots, which corresponds to a distance of $\sim 24 \text{ \AA}$ in real space identified with a $p(1 \times 4)$ superlattice. The primitive unit cell is indicated with a white square labelled "1". The $p(1 \times 4)$ unit cell is marked with the white square labeled "2" (LEED image taken by Guido Mariotto [8,138]). AES spectra for

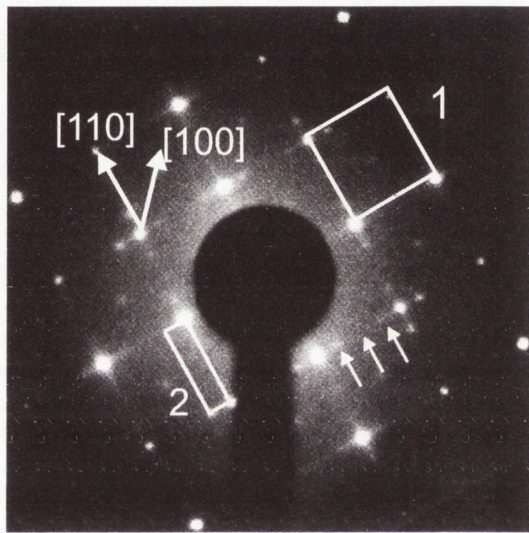


Figure 6.14: LEED pattern recorded for a $p(1 \times 4)$ surface reconstruction. The primitive unit cell is indicated with a white square labelled "1". The $p(1 \times 4)$ unit cell is marked with the white square labeled "2". The fractional order spots are indicated with white arrows. Reproduced from [138]

the $p(1 \times 4)$ reconstructed surface, typically showed surface contamination levels of $\leq 1.5\%$ for potassium and $\sim 6\%$ for calcium. The STM images showed well-defined trenches oriented along the $[110]$ and $[\bar{1}\bar{1}0]$ directions. The surface exhibits a two-fold symmetry since a rotation of the trenches by 90° was not observed on the same terrace but only on terraces separated by $2.1 \pm 0.2 \text{ \AA}$ high steps. We can therefore conclude that the surface is B-layer terminated. The periodicity of the trenches on the terraces varies from 20 to 60 \AA . As annealing time is increased, the separation between the trenches becomes smaller and more regular [8,9,138]. This is shown in the line profile of figure 6.15 a) obtained by Ciaran Seoighe on a natural crystal, where the trenches are equidistant with a $24 \pm 2 \text{ \AA}$ periodicity between them (see figure 6.15 b)).

The dynamics of this trench formation is discussed by Mariotto *et al.* [8,9,138], attributing the trenches to K and Ca segregation and to a reduction of the O/Fe ratio at the surface. The increasing density of the trenches as a function of annealing time can be explained in terms of a size accommodation model (see section 6.3.1). Continued annealing produces a Ca build-up on the surface to a point where the surface becomes saturated. To accommodate more Ca, the surface undergoes a gradual transformation resulting in the formation of trenches. This type of surface provides a greater surface area and correspondingly a larger number of surface sites to accommodate more Ca atoms with respect to the flat surface.

An insight into the segregation mechanism of Ca atoms at the $\text{Fe}_3\text{O}_4(001)$ surface is provided by atomically resolved STM images like the one shown in figure 6.15 c).

Atomic rows oriented along the $[110]$ direction exhibit a $6 \pm 1 \text{ \AA}$ periodicity, while adjacent rows are separated by $\sim 5 \text{ \AA}$, instead of the 6 \AA value

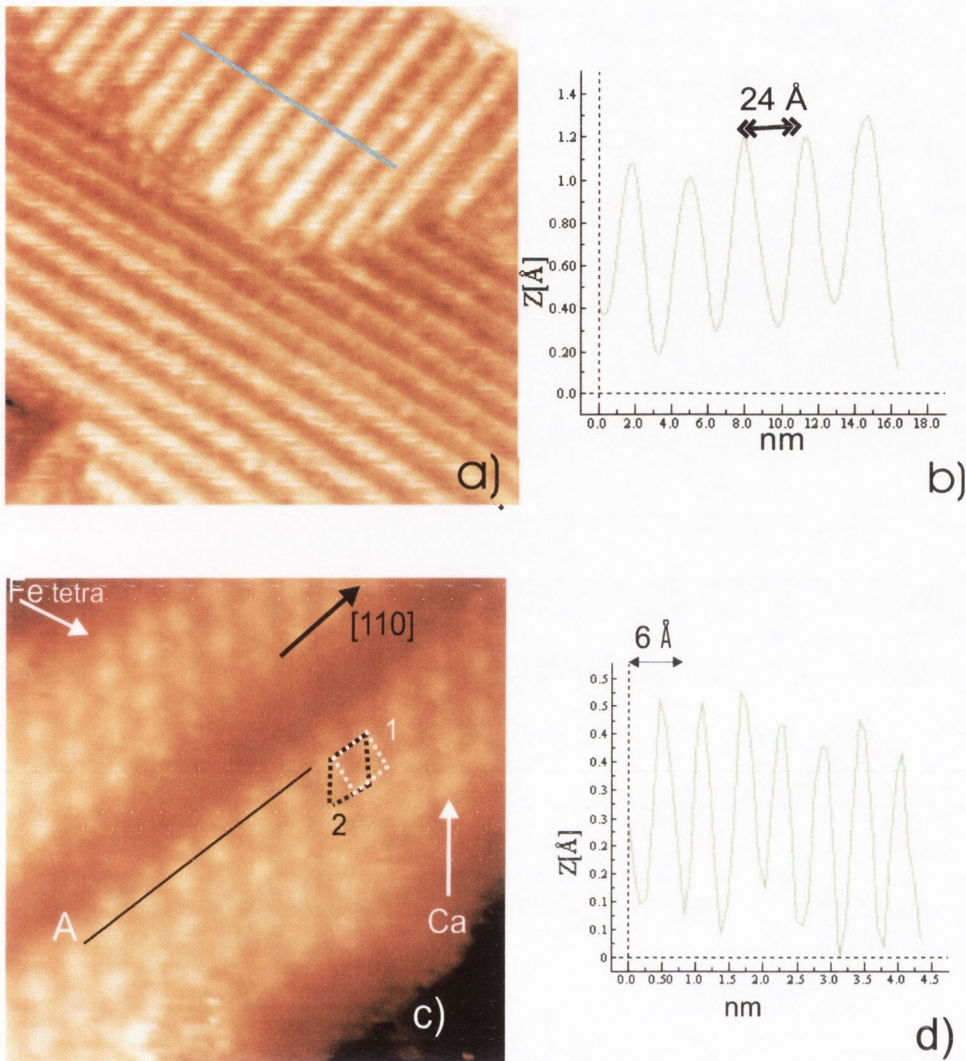


Figure 6.15: a) $(500 \times 500) \text{ \AA}^2$ STM image $I_t=0.1 \text{ nA}$, $V_b=1\text{V}$ taken with MnNi tip. Regular trenches can be clearly seen on the surface. b) Line profile corresponding to blue line in figure 6.15 a), shows a $24 \pm 2 \text{ \AA}$ periodicity between the trenches. c) $(70 \times 70) \text{ \AA}^2$ STM image taken with a MnNi tip, $I_t=0.1 \text{ nA}$, $V_b=1\text{V}$. The atomic rows exhibit a $6 \pm 1 \text{ \AA}$ periodicity along the $[110]$ direction. A $5 \pm 0.5 \text{ \AA}$ separation is observed between rows along the $[1\bar{1}0]$ direction. The $p(1 \times 1)$ superlattice is marked with a white square. d) Line profile along the $[110]$ direction in figure 6.15 c), showing a $6 \pm 1 \text{ \AA}$ periodicity. Reproduced from [91]

expected for a bulk terminated surface. The maxima on adjacent rows are shifted by $\sim 6 \text{ \AA}$ with respect to each other, giving rise to the superlattice in figure 6.15 c). The line profile in figure 6.15 d) shows a large corrugation of the rows along the $[110]$ direction. An average corrugation value of $\sim 0.4 \text{ \AA}$ average was measured. This value is approximately twice the value of the corrugation measured on rows of Fe ions on the clean octahedrally terminated $\text{Fe}_3\text{O}_4(001)$ surface. This large corrugation indicates that the atoms imaged on the narrow terraces are not Fe ions but, as indicated by the AES spectra, they are Ca or K atoms. It must be kept in mind that the clean and $p(1 \times 4)$ reconstructed surfaces were both scanned using the same type of tip (i.e. fabricated from MnNi alloy). Therefore, the difference in the corrugation cannot be ascribed to a tip effect, but is rather due to the different atomic species on the crystal surface.

Despite the fact that 1.5 % of potassium was detected by AES, we propose schematic models in figure 6.16 a) and b) to explain the observed surface structure explicitly in terms of Ca atoms segregating at the surface. Figure 6.16 a) shows the case when Ca ions replace every other Fe ions in octahedral coordination, while 6.16 b) illustrates the case of Ca ions occupying vacant interstitial sites in the octahedral cation sublattice.

This approach is taken because STM analysis of the surface shows the presence of a $\begin{pmatrix} 1 & 0 \\ 0.5 & 1 \end{pmatrix}$ incommensurate superlattice with an orthorhombic symmetry, which cannot be attributed to a potassium ferrite surface phase. The orthorhombic superlattice can be clearly seen in figure 6.15 c), with lattice parameters of $a \sim 3 \text{ \AA}$ and $b \sim 2.5 \text{ \AA}$. Since CaFe_2O_4 (Calcium ferrite) belongs to the P_{nam} space group (rhombohedral/ bipyramidal class) [144], we believe that a $\text{Ca}_{1-x}\text{Fe}_{2+x}\text{O}_4$ phase is present on the narrow terraces shown in figure 6.15 c). Three rows of Ca cations can be identified on each of the

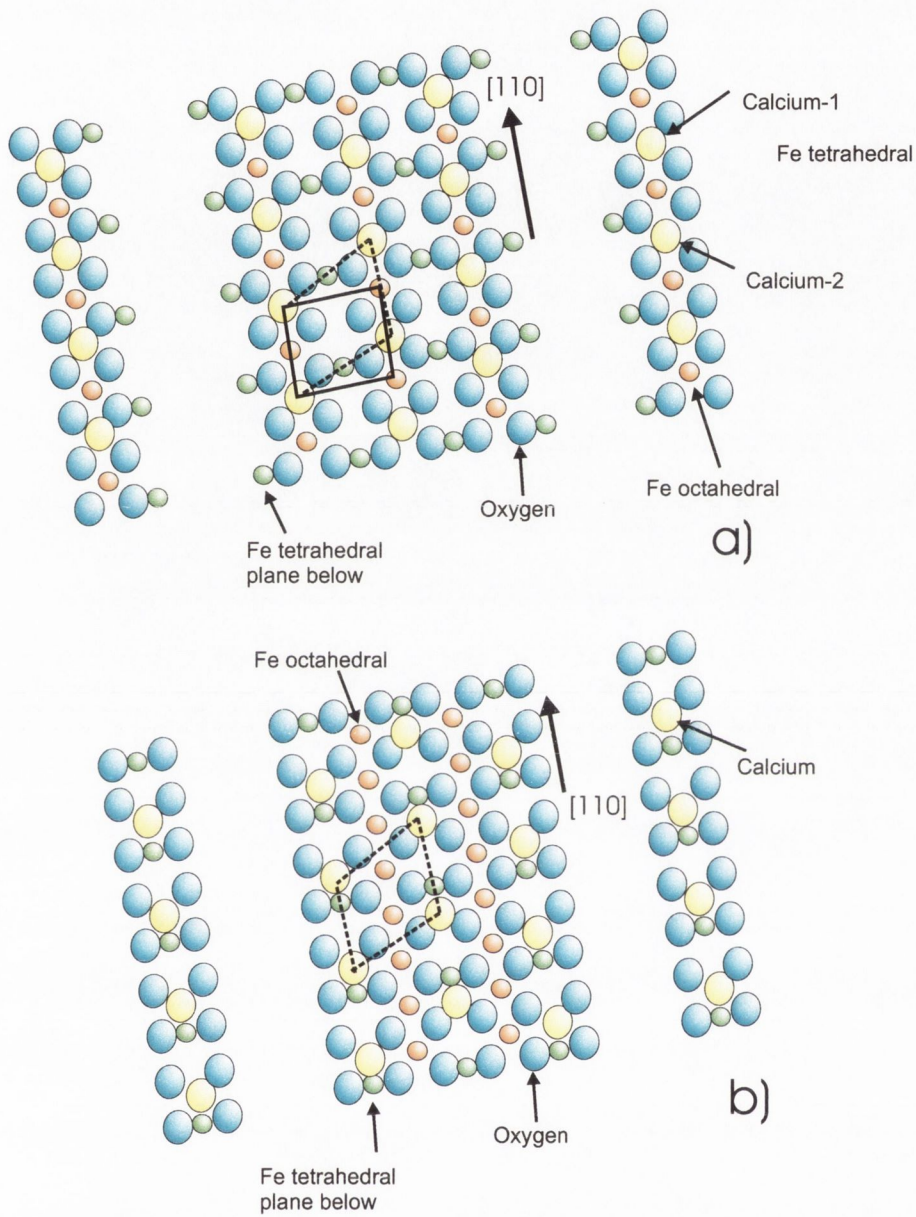


Figure 6.16: Two models of the atomic arrangement shown in the STM image 6.15 c). a) The Ca ions replace octahedral coordination Fe ions b) The Ca ions occupy vacant interstitial B-sites

narrow terraces shown in figure 6.15 c). On the sides of the Ca rows, less pronounced features can be observed. These features also form rows aligned along the [110] direction, with a $6 \pm 1 \text{ \AA}$ periodicity and a corrugation of $\sim 0.2 \text{ \AA}$. The periodicity and corrugation values indicate that these rows are composed of Fe ions in tetrahedral coordination. To check if our argument is sound, we have compared the concentration of Ca measured by AES with that predicted by our model, and we have found them in good agreement. A concentration of 4.7 % calculated from the model compares well with a 6 % concentration detected by AES.

Electron counting arguments show that oxygen vacancies in a *B*-layer would lower the polarity of the surface and make it more stable. The modified unit cell contains 3 Fe_{oct} atoms, 3 Ca_{oct} atoms and 12 O atoms and 4 missing oxygen atoms. An O creates 3 dangling bonds on neighbouring Fe atoms. A $0.90 e^-$ /unit cell are required to compensate the surface. This surface remains non-autocompensated, although it is more stable than the $p(1 \times 3)$ reconstructed surface or an octahedrally bulk-terminated one. The $p(1 \times 4)$ surface reconstruction was observed on numerous occasions and it was indeed found to be a highly stable state. Without disregarding the autocompensation model that was followed by many other authors to support their results, It is remarked that non-autocompensated polar-surfaces have been observed before. This is the case for the $\text{NiO}(111)/\text{NiO}(100)$ system [145], $\alpha\text{-Fe}_2\text{O}_3$ under certain preparation conditions [146, 147], $\text{Fe}_3\text{O}_4(001)$ [34] and other oxides for example.

Magnetite thin films

A wide range of surface reconstructions have been observed on thin $\text{Fe}_3\text{O}_4(001)$ films grown on $\text{MgO}(001)$, as explained in the literature review in the

introduction. To complete the study of the influence of contaminants on the surface of Fe_3O_4 , a 70-nm magnetite thin film was grown on polished-MgO (001) substrate by MBE and investigated by LEED/AES/STM/STS.

The preparation procedure adopted for the initial cleaning of the thin film was similar to that in section 5.3. Preliminary AES analysis confirmed the presence of contaminants such as carbon and nitrogen on the surface as well as a [O/Fe] ratio of 1.56. These contaminants were removed from the surface by light Ar^+ sputtering for 10 minutes at 500 eV. (typical $I_{\text{target}} \sim 7 \mu\text{A}$). The crystal was then annealed in an oxygen partial pressure (exposure ~ 3600 Langmuir). In order to avoid massive diffusion of Mg and other contaminants present in the substrate, the sample was annealed in UHV for long periods of time at rather low temperature of $300\text{-}400 \pm 50$ °C. Annealing the sample back and forward in an oxygen atmosphere and in UHV produced a sharp $(\sqrt{2} \times \sqrt{2})R45^\circ$ and p (1×1) LEED pattern. This effect has been also observed in single crystals of magnetite (001). Figure 6.17 shows a (2000×2000) Å² STM image of a contaminant free magnetite surface corresponding to a sharp $(\sqrt{2} \times \sqrt{2})R45^\circ$ LEED pattern. The thin film has been annealed for a total of 200 h at $300 - 400 \pm 50$ °C. STM has been performed every 13-15 hours of annealing. Figure 6.17 shows a STM image of a disordered surface, recorded after 180 hours of annealing in UHV. No terraces have been formed on the surface.

Voogt *et al.* [55] studied the influence of Fe_3O_4 grown on a MgO (001) cleaved and polished substrate by AFM. A rough surface without macrosteps was observed on the MgO (001) polished substrate. On the other hand, the opposite effect has been found for *in-situ* and *ex-situ* MgO (001) cleaved substrates. This, led to the initial conclusion that a polished MgO (001) substrate is not suitable for the growth of Fe_3O_4 . The latter result has been

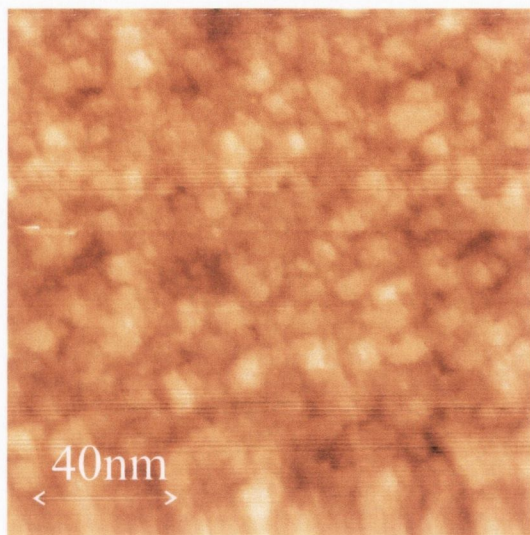


Figure 6.17: a) A $(2000 \times 2000) \text{ \AA}^2$ STM image of a disordered 70 nm Fe_3O_4 /polished-MgO (001) surface taken with a MnNi tip, $I_t=0.1 \text{ nA}$, $V_b=1V$.

proved wrong by other authors [53,60] who have employed polished MgO as substrates for their STM studies on Fe_3O_4 .

A 70 nm Fe_3O_4 thin film grown on a cleaved and polished MgO (001) substrate has been investigated by the author. No presence of macrosteps or terraced surface observed for either of them when annealing at $300\text{-}400 \pm 50^\circ\text{C}$.

An increase of the annealing temperature of the thin films to $500\text{-}600^\circ\text{C}$, on both substrates, led to diffusion of Mg to the surface. AES data are summarised in figure 6.18.

The number of annealing hours are plotted against the percentage of Ca and Mg diffused to the surface (on the horizontal and vertical axes respectively). LEED, AES and STM was performed after 3.5 hours of annealing. AES spectrum showed a high level of contamination ($[Ca]=0.5\%$ and $[Mg]=8\%$ atomic concentrations) on the surface. LEED data showed fractional order spots of $1/4$ and $1/3$ separation from the primary spots. This corresponds

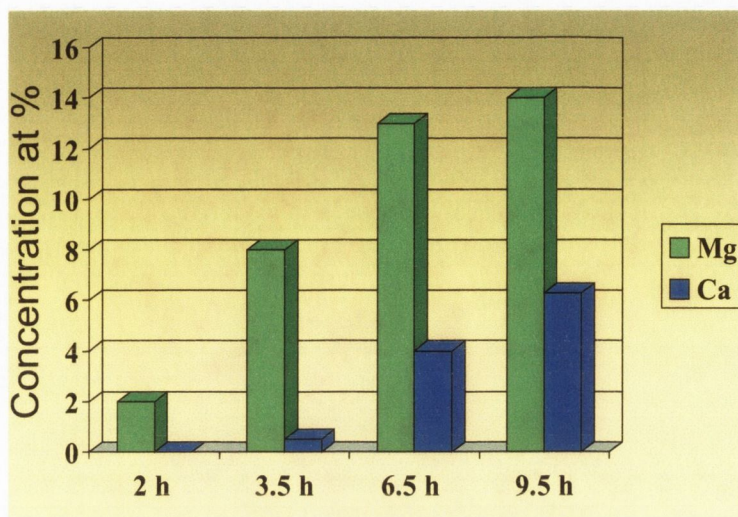


Figure 6.18: AES chart. The concentration of Ca and Mg diffused to the surface against annealing time at a temperature of 500-600 °C is presented.

to a distance of $\sim 24 \text{ \AA}$ and 18 \AA identified with a $p(1 \times 4)$ and $p(1 \times 3)$ superlattices respectively. Figure 6.19 a) shows a $(1000 \times 1000) \text{ \AA}^2$ STM image with step heights multiples of $2.10 \pm 0.2 \text{ \AA}$ which corresponds to the separation between planes in magnetite bulk. Although the square terrace definition has been lost, rounded terraces have formed on the surface.

These results differ with the ones obtained by *Chambers et al.* [58] where a 300 °C annealing temperature was used to obtain a terraced surface, although it could be attributed to the use of a thicker film. *Gaines et al.* [53] also observed a $(\sqrt{2} \times \sqrt{2})R45^\circ$ superlattice on a 100 nm magnetite thin film when high temperature annealing was used. This did not lead to diffusion of contaminants to the surface, contrary to our results. The annealing temperature of the crystal is critical if contaminants are avoided, although for films thinner than 100 nm, contaminants are hard to avoid if a terraced surface is to be obtained.

Figure 6.19 b) shows a $(1300 \times 1300) \text{ \AA}^2$ STM image taken on the same

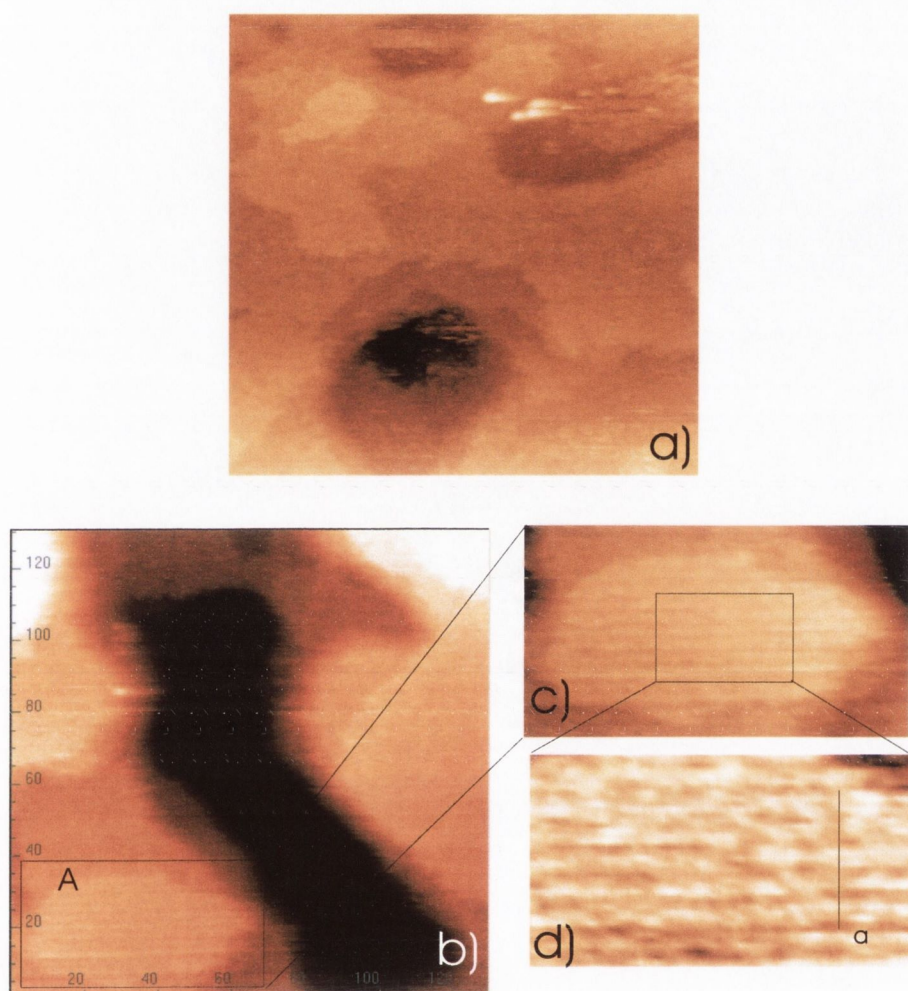


Figure 6.19: a) A $(1000 \times 1000) \text{ \AA}^2$ STM image taken with a MnNi tip, $I_t=0.1 \text{ nA}$, $V_b=1\text{V}$. Rounded terraces on the surface are formed due to the high temperature annealing. Neighboring terraces are separated by multiples of $2.1 \pm 0.2 \text{ \AA}$. b) A $(1300 \times 1300) \text{ \AA}^2$ STM image taken with a MnNi tip, $I_t=0.1 \text{ nA}$, $V_b=1\text{V}$. c) and d) A (700×700) and $(300 \times 300) \text{ \AA}^2$ STM images. A 24 \AA periodicity is found on the line profile marked as *a* in figure 6.19 d).

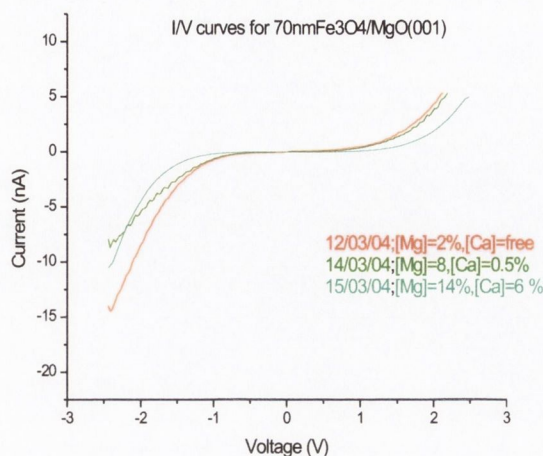


Figure 6.20: I/V curves for different concentration rates of Mg and Ca diffused to the surface.

scanning session as figure 6.19 a). Atomic rows running on top of the terrace marked as *A* can be seen. A zoom-in on these rows is shown in figure 6.19 c) and d). A line profile marked as *a* in figure 6.19 d) shows a $24 \pm 2 \text{ \AA}$ periodicity between the rows, which corresponds to a $p(1 \times 4)$ surface reconstruction.

Scanning tunneling microscopy (STS) measurements were performed at RT by recording an $I(V)$ curve at every point of a topographic scan which is obtained at a typical set point of $V = 1 \text{ V}$ and $I = 0.1 \text{ nA}$.

Figure 6.20 shows 3 Intensity/Voltage curves taken in the range of -2.50, 2.50 Volts for the 70 nm film at different levels of contamination. A conductivity gap of $\sim 1 \text{ V}$ is found for a 2 % Mg contaminated surface (red curve). When the amount of contaminants is increased on the surface (green and blue curves) the conductivity gap increases to a maximum of 2.5 V (blue curve). I/V curves show how at negative bias, when the contaminant level increases, there is a tendency of decreasing the electron tunneling from the

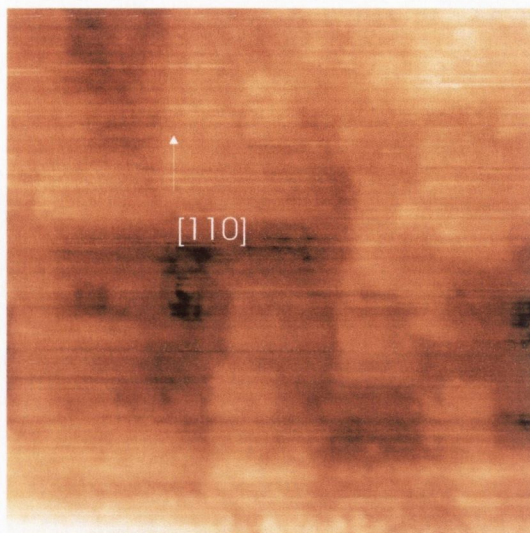


Figure 6.21: $(2000 \times 2000) \text{ \AA}^2$ STM image taken with a MnNi tip, $I_t=0.1$ nA, $V_b=1V$. STM image which shows that the terrace definition is almost completely lost for a highly contaminated $p(1 \times 1)$ mesh.

filled states of the sample to the empty states of the tip. This is due to the creation of a $Ca_{1-x}Fe_{2+x}O_4$ -like and $Mg_{1-x}Fe_{2+x}O_4$ -like insulator phase on the surface. The formation of a $Ca_{1+x}Fe_{2+x}O_4$ -like and $Mg_{1-x}Fe_{2+x}O_4$ -like phase on the surface, corroborated by STS results, is in agreement with the ball models proposed in sections 6.3.3 and 6.3.4.

6.4 $p(1 \times 1)$

Further annealing of the crystals brings the Ca concentration up to a value of 9.5 at % as shown by AES. No traces of any other contaminant are detected.

At this stage a $p(1 \times 1)$ LEED pattern was observed. Figure 6.21 shows a $(2000 \times 2000) \text{ \AA}^2$ STM image which shows that the terrace definition is almost completely lost.

6.5 Conclusions

We have studied the (001) surface of natural and synthetic Fe_3O_4 single crystals as well as the surface of Fe_3O_4 thin films grown on a MgO substrate using a range of surface sensitive techniques, AES, LEED, STM and STS. A detailed description of the preparation procedure leading to diffusion of contaminants to the magnetite surface is outlined. Diffusion of K and Ca bulk impurities and their surface segregation results in the formation of self assembled row structures. The main results can be summarized as follows:

1. The most common contaminants found on the surface of magnetite single crystals are Ca and K. Due to the high annealing temperatures, Ca and K ions diffuse from the bulk to the top most layers, being accommodated at the interstices of the magnetite unit cells (contaminant atomic concentration $< 1\%$). It is believed that the stress induced by contaminants breaks the long range $(\sqrt{2} \times \sqrt{2})R45^\circ$ order on the surface. The change of topography is a feasible argument to relax back the surface energy by means of shifting its reconstruction from a $(\sqrt{2} \times \sqrt{2})R45^\circ$ to a $p(1 \times n)$ with $1 < n < 4$.
2. Annealing of a contaminant free crystal in UHV induced segregation of Ca and K contaminants to the surface. For low concentrations (less than $\sim 2\%$) of contaminants, a $p(1 \times 2)$ surface reconstruction was observed. A $p(1 \times 3)$ reconstruction resulted after further annealing with an increase of the Ca and K on the surface. No reduction of the O/Fe ratio was observed. After long annealing sessions the $p(1 \times 3)$ reconstruction was replaced by the $p(1 \times 4)$ reconstruction. The O/Fe ratio has decreased as function of the annealing time. A concentration of Ca and K similar to the $p(1 \times 3)$ reconstruction was measured.

A $p(1 \times 4)$ reconstruction was also found on the surface of a 70 nm thin film grown on polished-/cleaved-MgO (001) substrate. STS results corroborates the insulator nature of a surface partially covered with a $\text{Mg}_{1-x}\text{Fe}_{2+x}\text{O}_4$ and $\text{Ca}_{1-x}\text{Fe}_{2+x}\text{O}_4$ phase. We can conclude that the surface reconstructions of Fe_3O_4 are induced on one hand by the contamination level on the surface and the O/Fe ratio on the other hand. For a high level of contamination a blurred $p(1 \times 1)$ LEED mesh was observe and STM images showed a surface where topographic features can hardly be distinguished.

To summarise, we have controlled the diffusion of alkaline and alkaline-earth metals to the surface which is translated in the formation of a range of nanostructures depending on the contaminations level. The preparation procedure and the presence of contaminants on the surface leads to a non-stoichiometric Fe_3O_4 surface. The $\text{Ca}_{1-x}\text{Fe}_{2+x}\text{O}_4$ or $\text{Mg}_{1-x}\text{Fe}_{2+x}\text{O}_4$ trenches and rows formed on the surface of magnetite are proposed as pre-patterned template for the formation of long one-dimensional molecular nanostructures. This type of direct forced-assembly using appropriate periodic superstructures on the nanoscale opens a variety of new possibilities for the ordered deposition of organic molecules on surfaces, and for guiding the growth of nanostructures in general. It also opens a wide field for basic surface studies, since very little is known at present about the adsorption properties of large organic molecules on well-defined surfaces.

Another possible avenue for future experiments could be related to self-assembly of magnetic structures such as evaporation of Fe and Cr on the patterned surface of magnetite not only for studying the modification of the electronic/magnetic properties of the substrate, but also to study the new properties of the nanoclusters grown on the magnetite substrate.

Chapter 7

Surface studies of Fe_3O_4 (110)

7.1 Introduction

In this chapter, a detailed study of the topography of the (110) surface is carried out. A comparison with research performed by other authors on this surface is outlined. The surface of a magnetite (110) single crystal and 50 nm $\text{Fe}_3\text{O}_4/\text{MgO}$ film have been investigated by AES, LEED, STM and STS. It is shown how a terraced surface can only be obtained by high temperature annealing of the crystal which leads to the formation of self-assembled nanostructures on a terraced surface. The latter has been identified with a Fe_3O_4 reconstructed surface. High annealing temperatures have been used for the preparation of the magnetite thin film, leading to segregation of Mg to the surface. The surface is also covered with self-assembled nanostructures. The self-assembled nanostructures are replaced by a well-defined terraced surface for the single crystal, when the surface of the crystal is highly exposed to oxygen gas. This change of topography is attributed to the change of the [O/Fe] ratio.

We demonstrate that the magnetite (110) surface is very sensitive to

[O/Fe] variations, and despite the fact that the surface is non-polar, it reconstructs under certain preparation conditions.

7.2 Sample preparation

A synthetic single crystal was grown by Prof. Y. M. Mukovskii (Moscow State Steel and Alloys Institute, Moscow, Russia) employing the floating zone technique. The crystal was characterized by four-point resistance vs. temperature measurements indicating a sub-stoichiometric crystal with a Verwey temperature of 110 ± 1 K. The crystal was mechanically polished using diamond paste with grain size down to $0.25 \mu\text{m}$ before being introduced into the UHV system. The experiments were carried out in the UHV system described in section 3. Magnetite thin films of 50 nm thickness were grown on a polished (110) oriented MgO single-crystal substrate using dc magnetron reactive sputtering from a 99.95 % purity Fe target in the presence of an argon-oxygen gas mixture. Structural characterisation of the sputtered $Fe_3O_4/MgO(110)$ was carried out in a multi-crystal high resolution x-ray diffractometer (HRXRD, Bede-D1, UK). In the triple-axis geometry, lattice constant variations ($\Delta a/a$) as low as 2×10^{-6} were detected.

7.3 Results and discussion

7.3.1 Formation of nanostructures

Single crystal

The first sample preparation attempt to obtain a contaminant-free magnetite (110) surface was similar to that described in section 5.3. A magnetite single

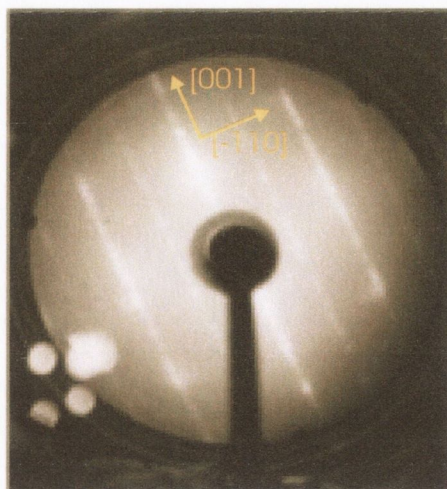


Figure 7.1: LEED pattern taken with a primary electron energy of 97 eV for a magnetite (110) surface. Blurred diffraction spots along the [001] direction are present whereas a defined 6 Å periodicity was determined on the $[\bar{1}10]$ direction.

crystal was Ar^+ ion etched followed by anneal in UHV at 900 ± 50 K for 15 hours.

This resulted in a contaminant free surface as shown by AES data, with a [O/Fe] ratio of 1.404. Figure 7.1 shows a LEED pattern typical of this Fe_3O_4 (110) surface. Blurred diffraction spots along the [001] direction are displayed. A $\sim 6 \pm 0.2$ Å periodicity was determined instead, on the $[\bar{1}10]$ direction in the real space.

STM and LEED were performed on the sample subsequent to every 12 hours anneal. The [O/Fe] ratio after 48 hours of annealing did not vary significantly. The LEED pattern still displayed blurred diffraction spots along the $[\bar{1}10]$ direction. STM of the surface, performed after a total number of 48 hours, still showed a disordered surface.

The crystal annealing temperature was then increased to 1100 ± 50 K for

1 hour. AES analysis showed presence of 4 % of Ca on the surface due to the high temperature annealing. Ca was removed with a light Ar^+ etching. Further annealing of the crystal at high temperature for 1.5 hours led to a reduction of the [O/Fe] ratio from 1.40 to 1.30. Traces of Ca were not found on the surface according to our AES data. A sharper rectangular LEED pattern was found (see figure 7.2 a)).

A $6 \pm 0.2 \text{ \AA}$ periodicity is measured along the $[\bar{1}10]$ direction in real space. Sharper diffraction spots along the [001] direction can now be seen. Fractional spots are at $1/3$ of the separation between the primary spots. Orange and yellow arrows mark the primary and fractional order spots respectively. These correspond to a separation of $\sim 9 \text{ \AA}$ and $\sim 24 \text{ \AA}$ for the primary and fractional order spots in real space. A schematic of the LEED pattern for this surface is presented in figure 7.2 b). A $\sim (25 \times 6) \text{ \AA}^2$ unit cell is identified with a (3×1) reconstruction. This is marked with an orange rectangle. The primitive unit cell, $(8.398 \times 5.937) \text{ \AA}^2$, is marked with a yellow rectangle in figure 7.2 b).

Figure 7.3 shows a $(1000 \times 1000) \text{ \AA}^2$ STM image of this surface. A terraced surface has been formed after a high temperature annealing. The edges of the terraces are aligned along the $[\bar{1}10]$ direction. Step heights are integer multiples of $1.5 \pm 0.1 \text{ \AA}$ corresponding to an A - B plane separation in magnetite (110) bulk.

A zoom-in of figure 7.3 is shown in figure 7.4 a). Atomic rows are running along the $[\bar{1}10]$ direction. A 24 \AA periodicity across the rows is found in the line profile marked as a (see line profile in figure 7.4 b)). Atomically resolved STM image of the nanostructures is shown in figure 7.4 c). Two sets of atomic rows can be distinguished running along the $[\bar{1}10]$ separated by $6 \pm 1 \text{ \AA}$ periodicity. The corrugation analysis shows that the two atomic rows

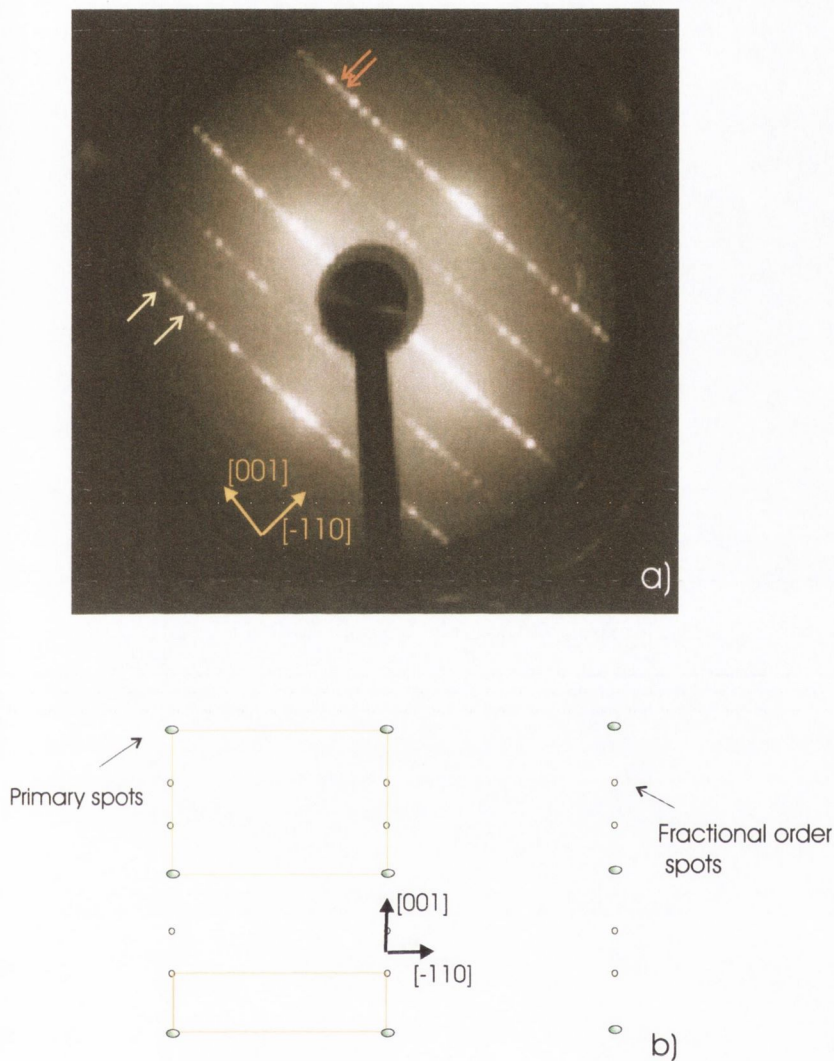


Figure 7.2: a) LEED pattern taken with a primary electron energy of 107 eV for a (110) surface. Primary and fractional order spots are marked with yellow and orange arrows respectively. b) Schematic of the LEED pattern observed. A $(8.398 \times 5.937) \text{ \AA}^2$ and a $(25 \times 6) \text{ \AA}^2$ unit cell are marked with an yellow and orange rectangle.

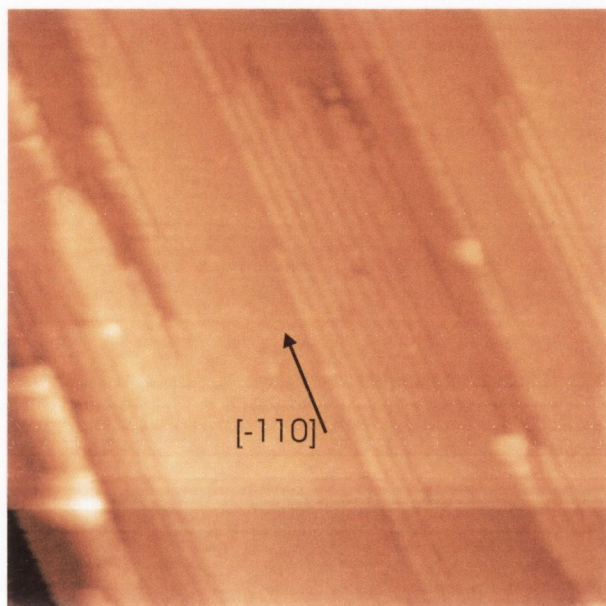


Figure 7.3: $(1000 \times 1000) \text{ \AA}^2$ STM image, $I_t=0.1 \text{ nA}$, $V_b=1 \text{ V}$ taken with a W tip. The terraced surface has been formed after high temperature annealing of the crystal.

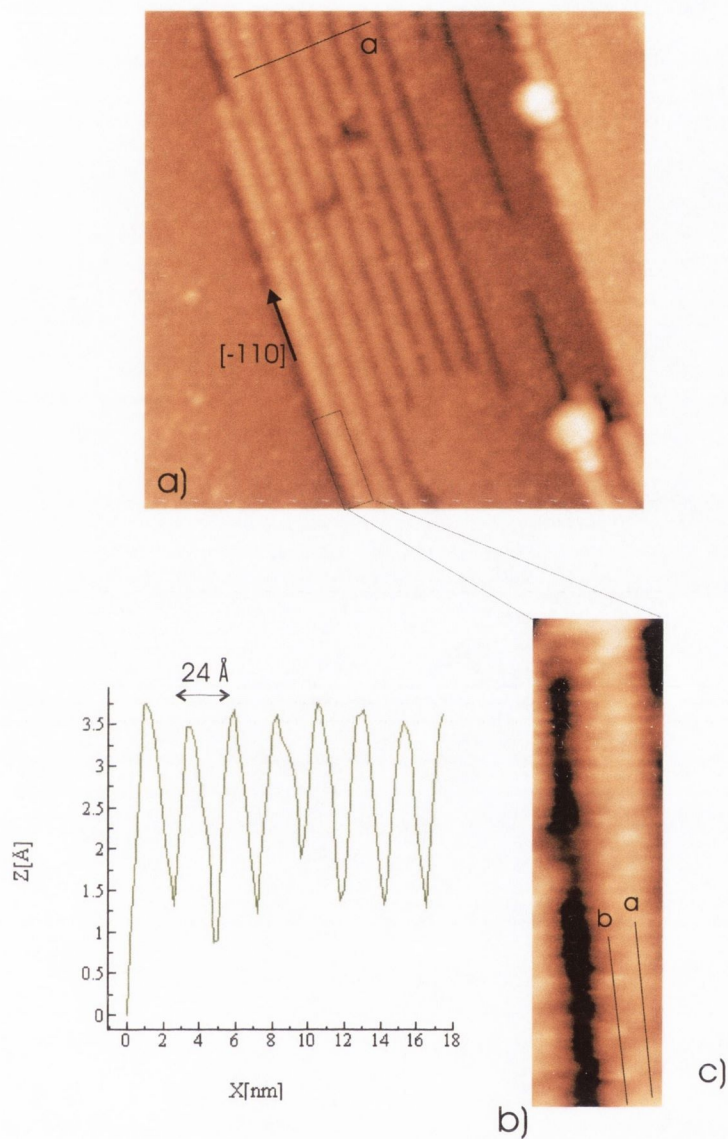


Figure 7.4: a) and b) (500×500) Å^2 STM image, $I_t=0.1 \text{ nA}$, $V_b=1 \text{ V}$ taken with a W tip and line profile marked as *a* respectively. Atomic rows are running along the $[\bar{1}10]$ direction. c) (330×130) Å^2 zoom-in STM image. Two set of atomic rows can be observed along the $[\bar{1}10]$ separated by $6 \pm 1 \text{ Å}$.

are on the same plane. The two atomic rows are marked as a and b in figure 7.4 c). A periodicity of $\sim 10 \text{ \AA}$ along the $[\bar{1}10]$ direction has been found.

50 nm of Fe_3O_4 on MgO (110)

A 50 nm magnetite thin film was used for this experiment. The thin film has been annealed at $1000 \pm 50 \text{ K}$ for 5 minutes. AES shows a high concentration of Mg on the surface. A 15 % coverage of Mg was found. A rectangular LEED pattern, similar to that found in figure 7.1 was obtained. Figure 7.5 a) shows a $(500 \times 500) \text{ \AA}^2$ STM image of the magnetite thin film obtained by Dr. Nikolai Berdunov. The areas inspected by STM were fully covered with rows separated by $\sim 24 \text{ \AA}$. A closer inspection of these rows is shown in figure 7.5 b). Although the rows are not atomically resolved as for the single crystal, two set of atomic rows can be distinguished on each rows. They are marked with black arrows. The atomic rows have a $\sim 6 \text{ \AA}$ periodicity along the $[001]$ direction and the rows are not in-phase along the $[\bar{1}10]$ direction. This is in good agreement with the results found for the single crystal.

7.3.2 Discussion

Two possible different surface terminations for magnetite (110) (A -or B terminated) have been described in section 2.2.3. As explained in section 2.2.4, the surface of magnetite (110) is non polar [48]. This means a bulk terminated magnetite (110) surface can be formed with small relaxations. A B -terminated surface is composed of octahedral irons separated by 3 \AA along the $[\bar{1}10]$ direction. A 3 \AA periodicity has not been found in our LEED or STM data. Therefore a B surface termination can be ruled out. An A surface termination is composed of octahedral irons separated by 6 \AA along the $[001]$ direction. These octahedral irons are not in-phase along the $[\bar{1}10]$ direction.

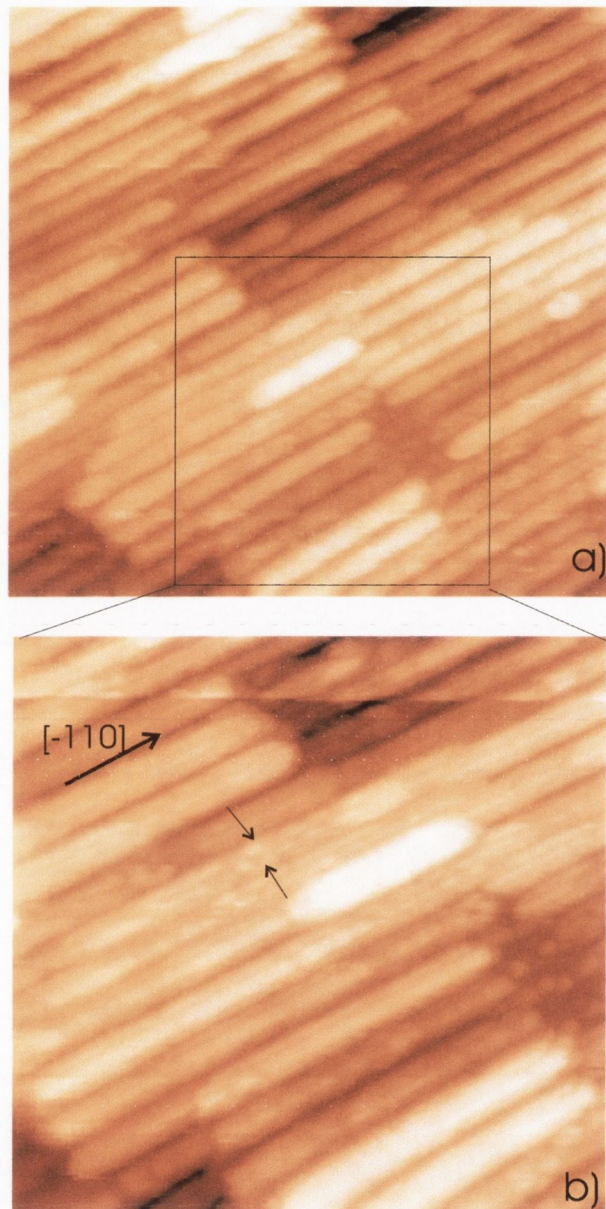


Figure 7.5: a) $(500 \times 500) \text{ \AA}^2$ STM image, $I_t=0.1 \text{ nA}$, $V_b=1 \text{ V}$ taken with a W tip. The surface is covered with rows separated by $\sim 24 \text{ \AA}$. b) $(300 \times 300) \text{ \AA}^2$ STM zoom-in. Two set of atomic rows can be distinguished running along the $[-110]$ and separated by $\sim 6 \text{ \AA}$ from each other. Reproduced from [148]

As demonstrated in chapter 6, as a result of exposing the magnetite surfaces to high temperatures, oxygen is desorbed from the surface. An A termination is more feasible for the surface reconstruction observed here if two unit cells are desorbed from the surface due to the annealing.

Traces of calcium have been regularly observed on the single crystal diffused from the bulk. Although it has been removed by light Ar^+ ion annealing as confirmed by our AES data, some calcium could remain on some localised areas of the surface undetectable by AES. The rows observed in figure 7.4 were not observed on the whole surface, just on some discrete areas. The same reconstruction has been observed on the thin films when Mg has diffused to the surface. We believe that the surface does not change phase to another iron oxide in the light of our LEED and STM results. None of the other three iron oxide phases, $Fe_{1-x}O$, $\gamma-Fe_2O_3$ or $\alpha-Fe_2O_3$ matches with the $\sim (6 \times 8.4) \text{ \AA}^2$ and $\sim (6 \times 24) \text{ \AA}^2$ periodicity found in our experiments. Therefore, it is assumed that the surface remains magnetite (110). It is concluded that the surface reconstruction observed is caused by a local change of the stoichiometry and the presence of contaminants on the surface of magnetite.

Figure 7.6 depicts a schematic of the reconstruction found. Ca ions, in the case of the single crystal, and Mg ions, in the case of the thin film, segregate to the surface via interstices by the same mechanism as that proposed in chapter 6. Ca and Mg may replace every second octahedral Fe on a A terminated magnetite (110) surface. These ions could also nucleate at every second interstice between the Fe ions on octahedral sites. The (1×3) reconstructed unit cell is marked with a dashed rectangle. This would induce the formation of a $Mg_{1-x}Fe_{2+x}O_4$ or $Ca_{1-x}Fe_{2+x}O_4$ insulator phase on the surface as occurred for magnetite (001).

Although our results are in contradiction to those found in reference

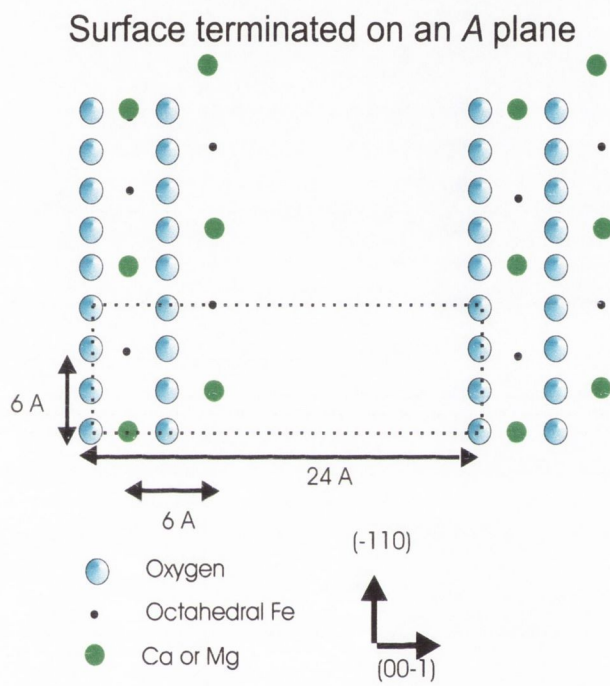


Figure 7.6: Schematic proposed for the (110) surface reconstruction found.

The (1×3) reconstructed unit cell is marked with a dashed rectangle.

[77, 78], they should not be disregarded since a different preparation procedure when cleaning the crystals was used there. *Jansen et al.* [78] carried out experiments on a 50 nm Fe_3O_4 (110) grown on a MgO substrate. As demonstrated in section 6.3.4, annealing of the thin films at such at 1100 ~ 50 K produces a massive diffusion of Ca and Mg to the surface, decorating the most top layer. The surface reconstruction found in reference [78] could be also formed by Mg atoms diffused to the surface.

STS results

Scanning tunneling spectroscopy was performed on the surface of the single crystal of magnetite (110). Figure 7.7 a) shows I/V curves for the range of [-2.5, 2.5] volts on two regions of the STM image shown in figure 7.7 b). STS data was recorded under the same conditions as those taken in section 6.3.4.

Area 1 shows a terrace where atomic order is not present. The latter has been also observed regularly on the surface of single crystals and thin films on magnetite (001). The cyan and black curves show two I/V curves on areas marked as 2 and 1 in figure 7.7, respectively. Two important features are highlighted. 1) The bigger conductivity gap on the nanostructure areas. 2) The low conductivity found on the nanostructured areas at negative bias. These two facts, are a good indication to corroborate the model proposed. The more insulating behaviour on the nanostructures shows the lack of Fe_{oct} ions (these irons favor electron hopping in magnetite [47]). This is in good agreement with the formation of $Mg_{1-x}Fe_{2+x}O_4$ or $Ca_{1-x}Fe_{2+x}O_4$ on the surface as proposed. A small tunneling current at negative bias is due to the lack of electrons available to tunnel from the sample to the empty states of the tip. This is due to a lack of oxygen anions (high density of filled states) as well as a lack of Fe_{oct} ions (lower density of empty states) . This has been

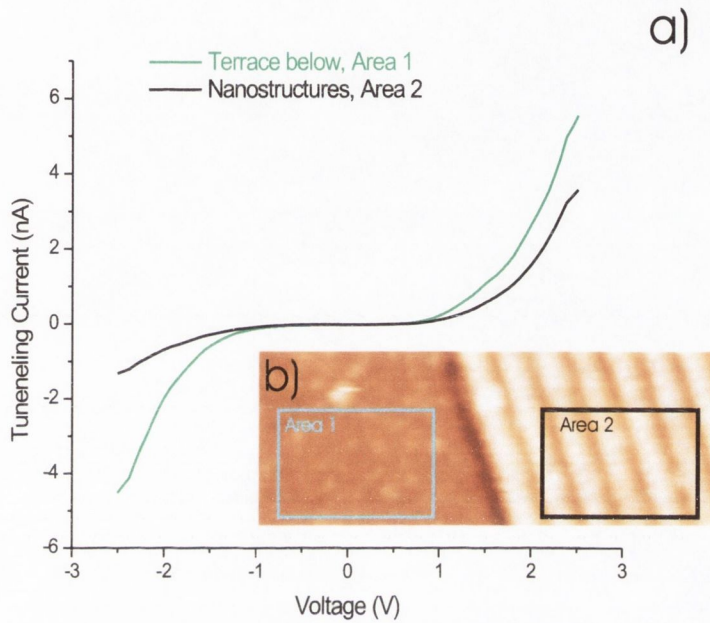


Figure 7.7: a) I/V curves for magnetite (110) surface. The cyan curve represents the I/V curve taken on a (110) surface, marked as area 1 in STM image b), where no atomic order is present. The black curve represents the I/V curve taken on the nanostructures marked as area 2. A bigger conductive gap representing the more insulating behavior on the nanostructures is highlighted

proposed in our model where Fe_{oct} and oxygen have been desorbed from the surface and Ca and Fe_{oct} ions form the nanostructures.

The nanostructures were called nanotrenches in chapter 6 when investigating the surface on Fe_3O_4 (001). A more interesting case is presented for magnetite (110) since a 90° rotation of the nanostructures is not feasible for this surface. All nanotrenches are oriented along the same direction in all terraces which eases evaporation processes.

7.4 Conclusions

The surface of a magnetite (110) single crystal and magnetite (110) grown on MgO have been investigated. It has been demonstrated that the morphology of the (110) surface of magnetite is highly sensitive to the treatment conditions which affect directly the [O/Fe] ratio of the surface and varies the presence of contaminants on the surface.

Annealing of the surface of magnetite at ~ 1100 K in UHV for short periods of time produced a re-organisation of the surface leading to a (6×8) \AA^2 and (24×6) \AA^2 periodicity as indicated by LEED and STM results. The (24×6) \AA^2 unit cell is identified with (3×1) superlattice. The nanostructures have been seen on both magnetite single crystals and thin films and their appearance has been attributed to change of the stoichiometry and diffusion of contaminants onto the surface. A model based on the formation of a $Ca_{1-x}Fe_{2+x}O_4$ or $Mg_{1-x}Fe_{2+x}O_4$ phase on the surface of magnetite is proposed.

As suggested in chapter 6, the nanotemplates found on the surface of (110) could be used for evaporation of different species compatible with their nanosizes.

Chapter 8

Summary

8.1 Conclusions

STM tips have been electrochemically etched from both antiferromagnetic and ferromagnetic materials, using a technique where the active etching region is physically restricted by a close-fitting section of teflon (PTFE) tubing. This technique produces sharp tips (typically 50-100 *nm* in diameter), with a low aspect ratio, making them very suitable for STM applications. Particular emphasis has been placed on the fabrication of tips from the antiferromagnetic materials Cr and MnNi, as it has been shown that these tips possess a number of advantages over ferromagnetic tips for spin-polarised STM applications. The implications of the tip preparation procedure on composition and magnetic order have been discussed for the MnNi binary alloy using XRD, AGFM and STS analysis. Their ability to provide SP-STM results for sample magnetisation in-plane has been proven. MnNi tips are used to obtain atomic resolution on the Fe₃O₄(001) surface and they have been used to resolve the atomic structure of the ($\sqrt{2} \times \sqrt{2}$)*R*45° reconstruction of the clean Fe₃O₄(001) surface. There is strong evidence for the interpretation of these

results in terms of a spin-polarised tunneling effect, where magnetic contrast is obtained between the Fe^{2+} and Fe^{3+} ions in the octahedrally terminated surface.

A contaminant free magnetite surface exhibits a $(\sqrt{2} \times \sqrt{2})R45^\circ$ superlattice. A *B*-terminated surface has usually been observed after annealing the sample in an oxygen atmosphere. However, a novel preparation procedure which leads to a co-existing *A* and *B*-surface termination after annealing the sample in a hydrogen atmosphere is described. Oxygen radicals are desorbed from the top most layer when reacting with hydrogen gas and the loss of Fe_{oct} cations occurs after further annealing in UHV. The surface preparation plays a critical role in determining the surface termination of magnetite (001).

Long annealing periods of a single crystal of magnetite in UHV induces segregation of Ca and K contaminants from the bulk to the surface. For low concentrations (less than $\sim 2\%$) of contaminants a $p(1 \times 2)$ surface reconstruction was observed. A $p(1 \times 3)$ reconstruction resulted after further annealing with an increase of the Ca and K on the surface. No reduction of the O/Fe ratio has been observed for this reconstruction. After long annealing times the $p(1 \times 3)$ reconstruction was replaced by the $p(1 \times 4)$ reconstruction. The O/Fe ratio has decreased as function of the annealing time. A concentration of Ca and K similar to the $p(1 \times 3)$ reconstruction was measured. We can conclude that the surface reconstructions of Fe_3O_4 are induced on one hand by the contamination level on the surface and on the other hand by the O/Fe ratio. For a high level of contamination a blurred $p(1 \times 1)$ LEED mesh was observed and STM images show a surface where topographic features can hardly be distinguished.

The topography and morphology of the non-polar surface of magnetite

(110) has been also studied. We have demonstrated that the (110) surface of magnetite is also highly sensitive to the treatment conditions which affects directly the [O/Fe] ratio of the surface. Nanorows separated by 24 Å periodicity have been observed along the [001] direction for a single crystal and a 50 nm thin film grown on MgO. These nanostructures are located in localised areas on the single crystal and were spread on the whole surface on the thin film. Their formation has been attributed to the presence of Ca and Mg on the surface.

8.2 Further work

8.2.1 Further characterisation of MnNi probes

To date, STM tips made of MnNi have been fabricated and characterised by Alternant gradient force magnetometer (AGFM), X-ray diffraction (XRD), Auger electron spectroscopy (AES) and Transmission electron microscope (TEM). It has also been proved by Scanning tunneling spectroscopy (STS) their ability to provide SP-STM measurements for an in-plane magnetisation sample. Although in this thesis their ability to provide SP-STM measurements has been shown, more conclusive claims can be made after the interpretation of the results which will be provided by Dr. S. McVitie and Prof. JN Chapman. These results are related to the further investigation of the magnetic order of the apex of the tip. It will be given by the Lorentz Microscopy where a transmission electron microscope (TEM) maps the stray magnetic field near the sample surface by monitoring the interaction of transmitted electrons with the field. More information about the local magnetisation direction of the apex of the tip (in plane/out of plane as discussed in section

4.3.4) will be obtained using a test sample such as Fe films on Au(111). Between 0.5 and 3 ML the magnetisation of the Fe film is out of plane as demonstrated by polar magneto Kerr effect (PMOKE) and AGFM [131,132]. If MnNi tips have a strong magnetization orientation out of plane, they could be ideal for resolving Bloch walls, step edges between terraces and samples with an out of plane magnetisation orientation at an *atomic level*.

8.2.2 Further characterisation of Fe_3O_4

Magnetite (001), (110) and (111) surfaces are a suitable test system to address fundamental questions such as metal-insulator transition dependency in low-dimensional materials with mixed valence or how the transition is affected by the fact that the surface of the sample is polar.

As future work, it is proposed to use spin-polarization STM to discriminate between the magnetic and electronic properties of the magnetite surface on an atomic scale and associate it with a possible charge ordering. To achieve spin-polarised contrast in tunneling tips will be made of the antiferromagnetic alloy MnNi, fabricated according to the technique that has been developed by the author. It will be also possible to apply an in-plane magnetic field in order to achieve spin contrast.

In chapters 6 and 7, trenches and protrusions on the surface of magnetite (001) and (110) have been imaged by STM and interpreted by a set of $p(1 \times n)$ with $1 < n < 4$ surface reconstructions. A further characterization of the properties of these surfaces is needed, *i.e.* a study of their transport properties. These highly ordered structures could be a starting point for the development of tailored magnetic surfaces. One could use these surfaces as nanotemplates for the deposition of carbon nanotubes, fullerenes and DNA molecules, whose sizes are compatible with the typical dimensions of our

nanotemplates. These templates could be also used for evaporation of other metallic materials for magnetic tunneling junction or magnetic self-assembly purposes.

Appendix A

AES calculations

As explained in section 3.2.4, part of the sample characterisation was performed by Auger electron spectroscopy (AES). The atomic concentrations of the elements on the surface of the crystals and thin films studied in this thesis have been calculated by equation A.1:

$$C_X = \frac{I_X/S_X d_X}{\sum_{\alpha} (I_{\alpha}/S_{\alpha} d_{\alpha})} \quad (\text{A.1})$$

where I_X is the peak-to-peak amplitude of the principle Auger transition measured for the element and S_X is the corresponding relative Auger sensitivity factor, taken from reference [149]. The main Auger transition peaks for pure elemental standards are marked in spectra also given in reference [149]. The summation is over one peak per element present on the surface. The scaling factor d_X is included so that concentrations may be determined from peaks measured under different conditions, this is given by:

$$d_X = L_X E_{M,X} I_{P,X} \quad (\text{A.2})$$

where L_X is the lock-in sensitivity, $E_{M,X}$ is the modulation energy and $I_{P,X}$ is the primary beam current.

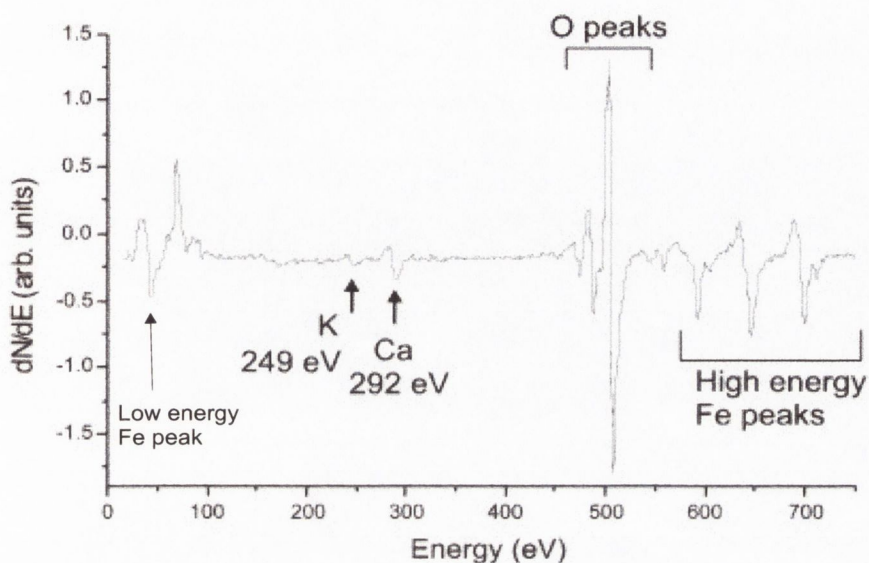


Figure A.1: a) The presence of K and Ca contaminants on the surface can be clearly seen on the AES spectrum. A Ca peak at 292 eV and a K peak at 249 eV are visible, corresponding to a $\sim 5.7\%$ and $\sim 1.5\%$ concentration in the near surface layers, respectively.

As an example of the atomic concentration calculations a contaminated magnetite (001) surface is used. The AES spectrum in figure A.1 corresponds to the $p(1 \times 3)$ surface reconstruction found in section 6.3.3.

In order to calculate the atomic concentration of the elements, equation A.1 is used. 4 different elements are present on the surface of Fe_3O_4 , Iron, oxygen, calcium and potassium. Since the low energy peaks are generally more susceptible to distortion by magnetic effects and localised specimen charging it is best to use peaks occurring above about 100 eV for quantitative analysis. Therefore, the Fe(703 eV) peak rather than the Fe (47) peak was chosen in this example. The other three components are Ca(292 eV), K(249

eV) and O(509 eV). The relative peak amplitudes for Fe(703 eV), Ca(292 eV), K(249 eV) and O(509 eV) were 8.18, 2.52, 1.42 and 30.25 respectively (in arbitrary units). The relative sensitivity factors from these peaks for a primary beam energy of 3 KeV are 0.2, 0.5, 0.85 and 0.5 respectively. The scale factor d_x is the same for all peaks and therefore cancels out. Application of equation A.1 to the Fe(703 eV) peak in this specimen yields:

$$[C]_{Fe} = \frac{8.18/0.20}{(8.18/0.20 + 30.25/0.50 + 1.42/0.85 + 2.52/0.5)} = 0.378 \quad (\text{A.3})$$

Similar calculations applying equation A.1 to the Ca, K and O peaks give, $[C]_{Ca} = 0.057$, $[C]_K = 0.015$ and $[C]_O = 0.559$.

There are several errors to these simple quantitative techniques. These are:

1. Matrix effects on the electron escape depths and backscattering factors. The dependence of Auger electron escape depth on the electronic structure of the host material may alter the depth of measurement in the specimen relative to that in a standard. Since the magnitude of the Auger signal is proportional to the number of atoms in the analysis volume, a larger escape depth will cause a corresponding increase in Auger signal.
2. Chemical effects can change the peak shape and thus lead to error when using peak-to-peak heights in the differential spectrum as a measure of the Auger signal.
3. Surface topography: Generally, a highly polished surface produces a larger Auger signal than a rough surface. This effect is minimised by determining concentrations from equation A.1 since surface roughness is expected to decrease all Auger peaks by nearly the same percentage.

Appendix B

LEED calculations

A detailed description of the LEED operation has been given in section ???. Using equation 2.20 and taking into account that magnetite has a cubic symmetry, equation 2.19 now reduces to:

$$\frac{a}{n} = \frac{h}{\sin\alpha\sqrt{2meE_{eV}}} = \frac{12.2643}{\sin\alpha\sqrt{E_{eV}}} \text{ \AA} \quad (\text{B.1})$$

where E_{eV} is the beam energy in eV.

The radii of curvature of the screen is 66 mm and its diameter, D_R is 104 mm. Using figure 3.6, it can be established that $\sin\alpha = d_R/66$. Using this result together with equation 3.3, we can reduce equation B.1 to:

$$\frac{a}{n} = \frac{7.783D_{photo}}{d_{photo}\sqrt{E_{eV}}} \text{ \AA} \quad (\text{B.2})$$

The lattice parameters of the contaminated magnetite (001) surface studied in section 6.3.3 are calculated as an example. Figure B.1 a) shows the LEED pattern displaying fractional order spots along the $[110]$ and $[1\bar{1}0]$ directions. The fractional order spots are marked with bright arrows and their separation is $1/3$ of the separation between the primary spots. A red arrow marks the measurement position. The arrow shown is twice the value d_{photo} .

The energy of the primary electron beam was 47 eV. The distance between successive spots along the [110] direction is 48.4 mm. The value of D_{photo} in this image is 143 mm. Using equation B.2 a lattice parameter of 5.5 Å is obtained for the [110] direction. Therefore, a 16.5 Å is the value that corresponds to the distance between the satellite spots in the real space. These values were identified in section 6.3.3 with a $p(1 \times 3)$ superlattice of unit cell $6 \times 18 \text{ Å}^2$.

The expected value along the [110] direction between the main primary spots is 5.9 Å. Therefore there is a 6 % error in the set up, related to the camera optics, the position of the sample on the magnetic drive and measurements of the LEED spots. Figure B.1 b) shows a schematic of the LEED pattern found in figure B.1 a). It shows the $p(1 \times 1)$ and $p(1 \times 3)$ surface structures in reciprocal space, whereas figure B.1 c) shows the interpreted pattern, together with STM data, in the real space. The $p(1 \times 1)$ and $p(1 \times 3)$ unit cells are marked with a red and black dashed square respectively.

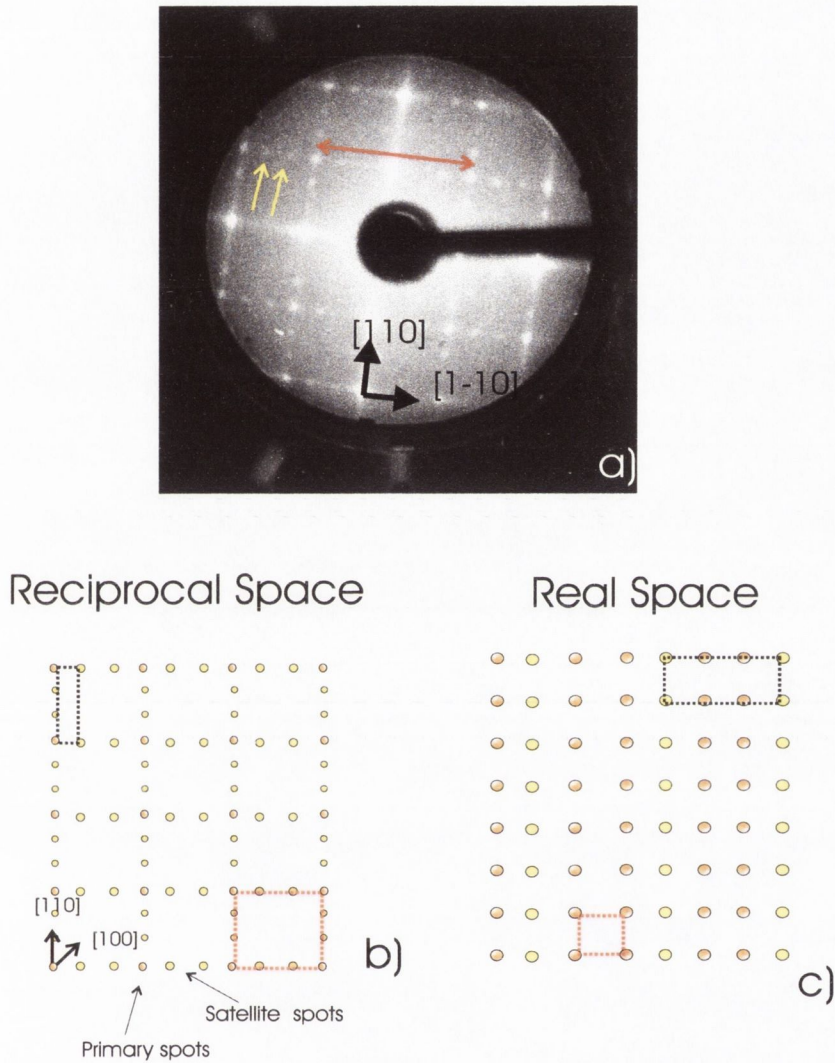


Figure B.1: a) LEED pattern taken with a primary electron energy of 47 eV. Fractional order spots around the primary spots are clearly seen along the $[110]$ and $[1\bar{1}0]$ directions. They are marked with yellow arrows. Their separation is $1/3$ of that between the integral order spots. b) and c) shows the $p(1 \times 1)$ and $p(1 \times 3)$ surface structures in reciprocal and real space. They are marked with a red and black dashed square respectively.

Appendix C

Polar and non-polar surfaces

As we have seen in section 2.2.4, surfaces are classified in three types according to reference [51]. Type 1 and 2 surfaces have a zero dipole moment μ in their repeat unit cell and thus stable potential. Type 3 have a diverging electrostatic surface energy, due to the presence of a net dipole moment, not only on the outer layers, but also on all the repeat units throughout the material. These type of surfaces are depicted in figure C.1.

As depicted in figure 2.9, magnetite (001) has an ionic charge ± 6 per layer unit cell throughout the crystal, making the surface energy diverge. It belongs to surface type 3 and it is polar. To cancel its polarity it needs an extra charge of ± 3 depending of surface termination. On the other hand, magnetite (110) has a net dipole moment zero perpendicular to the surface. Therefore it lies under the classification of a non polar surface.

A crystalline compound cut along a polar direction can be represented as in figure C.2

A simple analysis of a polar surface shows how the electrostatic contribution to the surface energy diverges. Each unit cell has a dipole moment of $\mu = \sigma R$. The electrostatic potential increases then as $\delta V = 2\pi\sigma R$ per

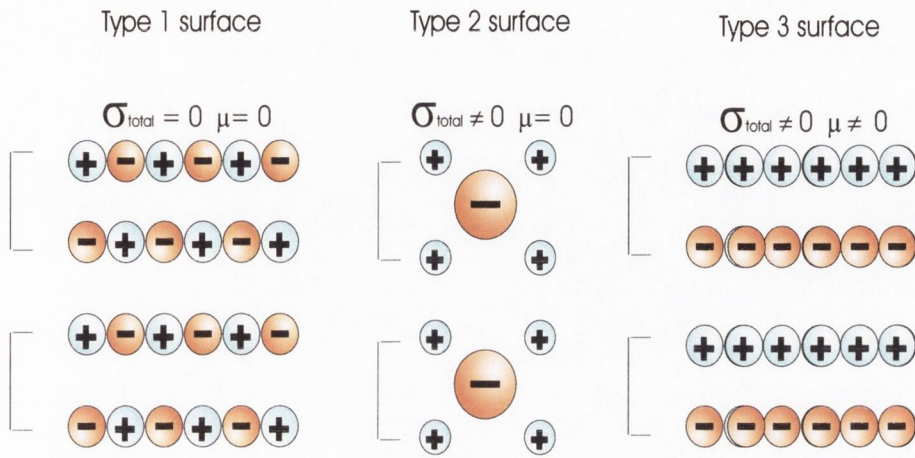


Figure C.1: Classification of surfaces according to Tasker [51]. σ and μ are the layer charge density and the dipole moment in the repeat unit cell perpendicular to the surface respectively.

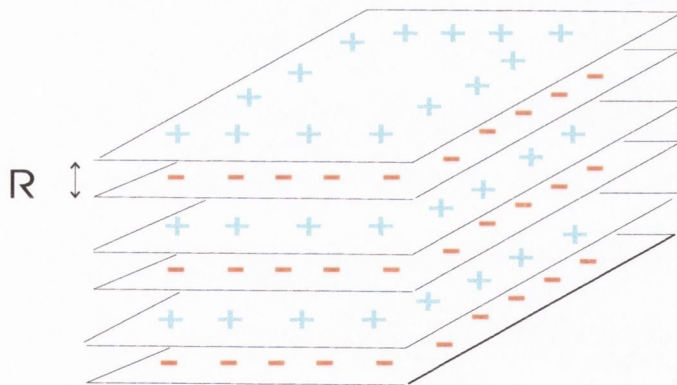


Figure C.2: representation of a crystalline compound cut along a polar direction. R represents the separation between layers in the crystal.

double layer (δV is of the order of a few tens of eV for MgO). The total dipole moment $M = N \sigma R$ of N bilayers is proportional to the slab thickness and the electrostatic energy amounts to $E = 2\pi NR \sigma^2$, which it is very large even for thin films (Thin films used by the author exceed 60 unit cells). It is clear then:

$$\lim_{N \rightarrow \infty} E = 2\pi NR \sigma^2 \rightarrow \infty \quad (\text{C.1})$$

creating surface instability.

To stabilised a polar surface such as magnetite (001), implies that either the charges or the stoichiometry in the surface layers are modified with respect to the bulk, and several scenarios would cancel the polarity:

1. One of several surface layers have a composition which differ from the bulk stoichiometry. This leads to the phenomenon of reconstruction. This effect has been seen on the contaminant free surface of magnetite (001) explained in chapter 5. The surface reconstructs in a $(\sqrt{2} \times \sqrt{2})R45^\circ$ and has a redistribution of charges.
2. Foreign atoms or ions, coming from the bulk to the surface or from residual atmosphere in the experiment set up, provide the charge compensation. This has been observed on the contaminated magnetite (001) and (110) where Mg, Ca and K has diffused to the surface.
3. On stoichiometric surfaces, charge compensation may result from an electron redistribution in response to the polar electrostatic field [150].

Despite the fact that the surface of magnetite (110) studied in chapter 7 is a non-polar surface, it has been seen that under high temperature annealing treatment, the surface reconstructs. Nevertheless this does not violate

Tasker's model since type 1 and 2 surfaces, even having a finite surface energy, can also, in some occasions, suffer a surface re-organisation as observed by the author.

Bibliography

- [1] A. Yanase and K. Siratori. *J. Phys. Soc. Jap.*, 53(31):2, 1984.
- [2] E.J.W. Verwey, P.W. Haayman, and R. Romeyn. *J. Chem. Phys.*, 15:181, 1947.
- [3] J. Y. T. Wei, N. C. Yeh, and R. P. Vasquez. *Phys. Rev. Lett.*, 79(25):5150, 1997.
- [4] E.J.W. Verwey and P.W. Haayman. *Physica*, 8:979, 1941.
- [5] P.A. Cox. *Transition Metal Oxides. An Introduction to their Electronic Structure and Properties*. Carendon Press, Oxford, 1995.
- [6] R. Aragon, R. J. Rasmussen, J.P. Shepherd, J.W. Koenitzer, and J. M. Honig. *J. Magn. Magn. Mater.*, 54-47:1335, 1986.
- [7] Guido Mariotto. *Surface reconstructions of Fe₃O₄ (001)*. PhD thesis, Physics Department. Trinity College Dublin, 2001.
- [8] S.F. Ceballos, G. Mariotto, K. Jordan, S. Murphy, C. Seoigue, and I.V. Shvets. *Surf. Sci*, 548:106–116, 2004.
- [9] G. Mariotto, S.F. Ceballos, S. Murphy, and I.V. Shvets. *Surf. Sci.* Accepted, May 2004.

- [10] D. Briggs and M. P. Seah. *Auger and X-ray Photoelectron Spectroscopy*, volume 1 of Practical Surface Analysis. Wiley, New York, 2 edition, 1990.
- [11] editor J.C. Vickerman. *Surface Analysis: The Principal Techniques*. Wiley, New York, 1997.
- [12] C. Julian Chen. *Introduction to scanning tunneling microscopy*. Cambridge University Press, Cambridge, 1994.
- [13] R. Wiesendanger. *Scanning Probe Microscopy and Spectroscopy*. Cambridge University Press, Cambridge, 1994.
- [14] J. Bardeen. *Phys. Rev. Lett.*, 6:57, 1961.
- [15] Landau L. D. and Lifshitz L. M. *Quantum Mechanics*. Pergamon press, Oxford, 3 edition.
- [16] J. A. Stroncio R. M. Feenstra and A. P. Fein. *Surf. Sci.*, 181:295, 1987.
- [17] T. K. Yamada, M. M. J. Bischoff, G. M. .M. Heijnen, T. Mizoguchi, and H. van Kempen. *Phys. Rev. Lett.*, 90 (5):056803, 2003.
- [18] P. Poddar, T. Fried, and G. Markovich. *Phys. Rev. B*, 65:172405.
- [19] J. Y. T. Wei and N. C Yeh. *J. Apl. Phys.*, 83 (11):7366, 1998.
- [20] J. A. Stroscio, R. M. Feenstra, and A. P. Fein. *Phys. Rev. Lett.*, 57 (20):2579, 1986.
- [21] J. A. Stroncio, D. T. Pierce, A. Davies, and R. J. Celotta. *Phys. Rev. Lett.*, 75 (16):2960, 1995.

- [22] Maartin Bischoff. *Chemical Identification in Scanning tunneling microscopy by detection of element-specific localised surface states*. PhD thesis, Katholieke Universiteit Nijmegen, Nijmegen, 2002.
- [23] T. K. Yamada, M. M. J. Bischoff, T. Mizoguchi, and H. van Kempen. *Surf. Sci.*, 516:179–190, 2002.
- [24] M. M. J. Bischoff, T. Yamada, A. J. Quinn, and H. van Kempen. *Surf. Sci.*, 501:155–167, 2002.
- [25] V. A. Ukraintsev. *Phys. Rev. B*, 53:11176–11185, 1996.
- [26] M.A. Van Hove, V.H. Wienberg, and C.-M. Chan. *Low-Energy Electron Diffraction*. Volume 6 of Springer Series in Surface Science. Springer-Verlag, Berlin.
- [27] Carol E. Diebel, Roger Proksch, Colin R. Green, Peter Neilson, and Michael M. Walker. *Nature*, 406:299–302, 2000.
- [28] D. Bürgler., G. Tarrach, H.J. Güntherodt, R. Wiesendanger, I.V. Shvets, and J.M.D. Coey. *Europhys. Lett.*, 19(2):141, 1992.
- [29] G. Güntherodt, R.J. Gambino, R. Wiesendanger, H.J. Güntherodt, and R. Ruf. *Phys. Rev. Lett.*, 65:247, 1990.
- [30] M. Johnson and J. Clarke. *J. Appl. Phys.*, 67:6141, 1990.
- [31] R. Koltun, M. Herrmann, G. Güntherodt, and V.A.M. Brabers. *Appl. Phys. A*, 73:49–53, 2001.
- [32] A. Kubetzka, M. Bode, O. Pietzsch, and R. Wiesendanger. *Phys. Rev. Lett.*, 88:057201, 2002.
- [33] A.A. Minakov and I.V. Shvets. *Surf. Sci.*, 236:L377, 1990.

- [34] R. Wiesendanger, I.V. Shvets, D. Bürgler, G. Tarrach, H.J. Güntherodt, J.M.D. Coey, and S. Gräser. *Science*, 255:583, 1992.
- [35] K. Jordan, G. Mariotto, S.F. Ceballos, S. Murphy, and I.V. Shvets. *In preparation*.
- [36] R.M. Cornell and U. Schwertmann. *The Iron Oxides*. VCH Verlagsgesellschaft mbH, first edition edition, 1996.
- [37] R. W. G. Wyckoff. *Crystal structures*. Second edition edition, 1964.
- [38] S. F. Alvarado, M. Erbudak, and P. Munz. *Phys. Rev. B*, 14:2740, 1976.
- [39] Z. Szotek, W. M. Temmerman, A. Svane, L. Petit, G.M. Stocks, and H. Winter. *Phys. Rev. B*, 68 (5):054415, 2003.
- [40] M. Imada, A. Fujimori, and Y. Tokura. *Rev. Mod. Phys.*, 70:1039, 1998.
- [41] M. Iizumi and G. Shirane. *Solid State Commun.*, 17:433, 1975.
- [42] J. M. Zuo, J. C. H. Spence, and W. Petuskey. *Phys. Rev B*, 42:8451, 1990.
- [43] J. Yoshida and S. Iida. *J. Phys. Soc. Jpn.*, 42:230, 1977.
- [44] S. Iida, K. Mizushima, M. Mizoguchi, K. Kose, K. Kato, K Yanai, N. Goto, and S. Yumoto. *J. Appl. Phys.*, 53:2164, 1982.
- [45] M. Mizoguchi. *J. Phys. Soc. Jpn.*, 44:1501, 1978.
- [46] M. Mizoguchi. *Jor. Phys. Soc. Jap.*, 70(8):2333–2344, 2001.

- [47] G. Mariotto, S. Murphy, and I. V. Shvets. *Phys. Rev B*, 66:245426, 2002.
- [48] C. Noguera. *J. Phys. Cond. Matter*, 12 (31):367–410, 2000.
- [49] M.D. Pashley. *Phys. Rev. B*, 40(15):10481, 1989.
- [50] J.P. LaFemina. *Crit. rev. in surf. chem.* 3(297), 1994.
- [51] P.W. Tasker. *J. Phys. C. Solid State Phys.*, 12:4977, 1979.
- [52] G. Tarrach, D. Bürgler, T. Schaub, R. Wiesendanger, and H. Güntherodt. *Surf. Sci.*, 285(1), 1993.
- [53] J.M. Gaines, P.J.H. Bloemen, J.T. Kohlhepp, C.W.T. Bulle-Lieuwma, R.M. Wolf, R.M. Reinders, R.M. Jungblut, P.A.A. van der Heijden, J.T.W.M. van Eemeren, J. aan de Stegge, and W.J.M. de Jonge. *Surf. Sci.*, 373(85), 1997.
- [54] S. A. Chambers, S. Thevethasan, and S. A. Joyce. *Surf. Sci.*, 450:L273, 2000.
- [55] F. C. Voogt, T. Fujii, P.J.M. Smulders, L. Niesen, M.A. James, and T. Hibma. *Phys. Rev. B*, 60:11193, 1999.
- [56] B. Stanka, W. Hebenstreit, U. Diebold, and S. A. Chambers. *Surf. Sci.*, 49:448, 2000.
- [57] F. C. Voogt, T. Hibma, G. L. Zhang, M. Hoefman, and L. Niesen. *Surf. Sci.*, 1508:331–333, 1995.
- [58] S. A. Chambers and S. A. Joyce. *Surf. Sci.*, 420:111, 1999.
- [59] Y. J. Kim, Y. Gao, and S. A. Chambers. *Surf. Sci.*, 371:358, 1997.

- [60] J.F. Anderson, M. Kuhn, H. Diebold, K. Shaw, P. Stoyanov, and D. Lind. *Phys. Rev. B*, 56:9902, 1997.
- [61] K. A. Shaw, E. Lochner, and D. M. Lind. *J. Appl. Phys.*, 87:1727, 2000.
- [62] S. K. Shaikhutdinov, W. Weiss, and R. Schögl. *Appl. Surf. Sci.*, 161:497, 2000.
- [63] L. P. Zhang and M. Li. U. Diebold. *Surf. Sci.*, 242:412–413, 1998.
- [64] H. Nörenberg and J. H. Harding. *Surf. Sci.*, 473:151, 2001.
- [65] Hla S.W., Braun K. F., and Rieder K. H. *Phys. Rev. B*, 67(20):201402, 2003.
- [66] Lorente N., Hedouin M. F. G., Palmer R. E., and Persson M. *Phys. Rev. B*, 65(15):155401, 2003.
- [67] Gu C. Z., Braun K. F., and Rieder K. H. *Chin. Phys.*, 11(10):1042–1046, 2002.
- [68] Bouju X. and Devel M. Girard C. *Appl. Phys. A-Mat. Sci. Proc.*, 66(2):S749–S752, 1998.
- [69] Toda Y. and Yanagi H. *Appl. Phys. Lett.*, 69:2315, 1996.
- [70] Crone B., Dodabalapur A., Lin Y. Y., Filass R. W., Bao Z., LaDuca A., Sarpeshkar R., Katz H. E., and Li W. *Nature*, 403:521, 2000.
- [71] J. Simon and J. J. Andre. *Molecular Semiconductors*. Springer, Berlin, 1985.
- [72] J. J. Cox, S. M. Bayliss, and T. S. Jones. *Surf. Sci.*, 425:326, 1999.

- [73] G. Ginev, T. Riedl, R. Parashkov, H.-H. Johannes, and W. Kowalsky. *J. of Phys.:Cond. Mat.*, 15:2611, 2003.
- [74] E. Umbach, K. Glöckler, and M. Sokilowski. *Surf. Sci.*, 402-404:20, 1997.
- [75] M. Stöhr, M. Gabriel, and R. Röller. *Surf. Sci.*, 507-510:330, 2002.
- [76] C. Joachim, J. K. Gimzewski, and A. Aviram. *Nature*, 408, 2000.
- [77] R. Jansen, V.A.M. Brabers, and H. van Kempen. *Surf. Sci.*, 328:237–247, 1995.
- [78] R. Jansen, H. van Kempen, and R.M. Wolf. *J. Vac. Sci. Technol. B*, 14 (2):1173, 1996.
- [79] Y. Oda, S. Mizuno, S. Todo, E. Torikai, and K. Hayakawa. *Jpn. J. Appl. Phys.*, 37:4518, 1998.
- [80] A. Quinn. *Development of an ultra-high vacuum scanning tunneling microscope*. PhD thesis, Physics Department. Trinity College Dublin, July 1996.
- [81] J. Osing. *Studies towards spin sensitive scanning tunneling microscopy*. PhD thesis, Physics Department. Trinity College Dublin, October 1998.
- [82] S. Murphy. *Surface studies of the Fe/Mo(110) and Fe/W(100) epitaxial systems*. PhD thesis, Physics Department. Trinity College Dublin.
- [83] VAT Vacuum Products Ltd. 235 Regents Park Road, Finchley, London N3 3LG, UK.
- [84] Physical electronics Inc. (formaly Perkin-Elmer). 6509 Flying Cloud Drive, Eden.

- [85] Vacuum Generators. Maunsell Road, Castleham Industry Estate, Hastings, East Sussex BN8 6SJ, UK.
- [86] Caburn MDC Ltd. The Old Dairy, The street, Glynde, East Sussex BN8 6SJ, UK.
- [87] Pfeiffer Vacuum GmbH. Emmeliusstrasse, K-35614, Asslar.
- [88] Saes Getters G.B. Ltd. 5 Southern Court, South St, Reading, Berkshire RG1 4QS U.K.
- [89] Leybold Inficon Inc. Two Technology Place, East Syracuse, NY 13057-9714 U.S.A.
- [90] Thermo Vacuum Generators. Maunsell Road, Castleham Ind. Est. Hastings TN38 9NN, England.
- [91] Ciaran Seoighe. *Surface studies of magnetite (001)*. PhD thesis, Physics Department. Trinity College Dublin, 2000.
- [92] IRCON Inc. 7301 Norh Caldwell Av. Niles, Illinois 60648. U.S.A.
- [93] PSP vacuum technology. Unit 8 heather close, Lyme green bussines park, Macclesfield SK11 OLR, U.K.
- [94] Stanford Research Systems. 1290-D Reamwood Av., Sunnyvale, California, 94089 U.S.A.
- [95] S.H. Pan. *Piezo Electric Motor*. International patent publication No WO93/19194, 1993. International bureau, Worl Intellectual Property Organisation.
- [96] G. Mariotto, M. D'Angelo, and I.V. Shvets. *Rev. Sci. Instrum.*, 79(9), 1999.

- [97] G. Mariotto, M. D'Angelo, Y. Kresnin, and I.V. Shvets. *Appl. Surf. Sci.*, 145:530, 1999.
- [98] Omicron. Limberger Str. 75 D-65232 Taunusstein Germany.
- [99] Nanotec Electronica. c/ Padilla, 3 1.D 28006-Madrid.Spain.
- [100] A. Melded. *J. Vac. Sci. Technol B*, 9:601, 1990.
- [101] M. Fotino. *Appl. Phys. Lett.*, 60:2935, 1992.
- [102] T. Iijima and K. Yasada. *Jpn. J. Appl. Phys.*, 27:1546, 1988.
- [103] R. Zhang and D. G. Ivey. *J. Vac. Sci. Technol B*, 14:1, 1996.
- [104] Y. Nakamura, Y. Mera, and K. Maeda. *Rev. Sci. Instrum.*, 70:3373, 1999.
- [105] G. A. Fried, X. D. Wang, and K. W. Hipps. *Rev. Sci. Instrum.*, 64 (64):1495, 1993.
- [106] L. Huang and Y. H. Lee. *Rev. Sci. Instrum.*, 64:3022, 1993.
- [107] M. O. Watanabe and T. Kinno. *Appl. Surf. Sci.*, 76-77:353, 1994.
- [108] A. J. Nam, A. Teren, T. A. Lusby, and A. J. Melmed. *J. Vac. Sci. Technol B*, 13:1556, 1995.
- [109] K. Dickmann, F. Demming, and J. Jersch. *Rev. Sci. Instrum.*, 67:845, 1996.
- [110] W. Wulfhekel and J. Kirshner. *Appl. Phys. Lett.*, 75:1944, 1999.
- [111] W. Wulfhekel, H. F. Ding, and J. Kirshner. *J. Appl. Phys.*, 87:6475, 2000.

- [112] O. Pietzsch, A. Kubetzka, M. Bode, and R. Wiesendanger. *Phys. Rev Lett.*, 84:5212, 2000.
- [113] S. Heinze, M. Bode, A. Kubetzka, O. Pietzsch, X. Nie, S. Bluger, and R. Wiesendanger. *Science*, 288:1805, 2000.
- [114] A. Kubetzka, O. Pietzsch, M. Bode, and R. Wiesendanger. *Phys. Rev. B*, 63:140407, 2001.
- [115] D. Wortmann, S. Heinze, P. Kurz, G. Bihlmayer, and S. Blugel. *Phys. Rev. Lett.*, 86:4132, 2001.
- [116] H. Ding, W. Wulfhek, C. Chen, J. Barthel, and J. Kirschner. *Mater. Sci. Eng. B*, 84:96, 2001.
- [117] M. Bode, M. Getzlaff, and R. Wiesendanger. *Phys. Rev. Lett.*, 81:4256, 1998.
- [118] M. Bode, O. Pietzsch, A. Kubetzka, S. Heinze, and R. Wiesendanger. *Phys. Rev. Lett.*, 86:2142, 2001.
- [119] M. Cavallini and F. Biscarini. *Rev. Sci. Instrum.*, 71:4457, 2000.
- [120] R. Wiesendanger, H.-J. Güntherodt, G. Güntherodt, R. Gambino, and R. Ruf. *Phys. Rev. Lett.*, 65:247, 1990.
- [121] I.V. Shvets, R. Wiesendanger, D. Bürgler, G. Tarrach, H.-J. Güntherodt, and J.M.D. Coey. *J. Appl. Phys.*, 71:5489, 1992.
- [122] S. Murphy, J. Osing, and I.V. Shvets. *J. Magn. Magn. Mater.*, 686:198–199, 1999.
- [123] S. Murphy, J. Osing, and I.V. Shvets. *Appl. Surf. Sci.*, 497:144–145, 1999.

- [124] J. Kasper and J. Kouvel. *J. Phys. Chem. Solids*, 11:231, 1959.
- [125] Sakuma A. *J. Mag. Mag. Mat.*, 187:105–112, 1998.
- [126] W.B. Pearson, K. Brun, and A. Kjekshus. *Act. Chem. Scand.*, 19:477, 1965.
- [127] L. Pal, E. Kren, G. Kadar, P. Szabo, and T. Tarnoczi. *J. Appl. Phys.*, 39:538, 1968.
- [128] D. Briggs and M.P. Seah. *Practical Surface Analysis: Ion and Neutral Spectroscopy*. Wiley, New York, 1992.
- [129] D. J. Monsma and S. S. P. Parkin. *Appl. Phys. Lett.*, 77:720, 2000.
- [130] J. J. Versluijs, M. Bari, and J. M. D. Coey. *Phys. Rev. Lett.*, 87:026601, 2001.
- [131] C. Chappert, P. Bruno, B. Bartenlian, P. Beauvillain, A. Bounouh, R. Megy, and P. Veillet. *J. Mag. Mag. Mat.*, 148:165–166, 1995.
- [132] A. Gündel, A. Morrone, J. E. Schmidt, L. Cagnon, and P. Allongue. *J. Mag. Mag. Mat.*, 226-230:1616–1617, 2001.
- [133] G. Mariotto, S. Murphy, and I.V. Shvets. *Phys. Rev. B*, 66:245426, 2002.
- [134] M. Seo, J. B. Lumsden, and R. W. Staehle. *Surf. Sci.*, 50:541, 1975.
- [135] V. S. Smentkowski and J. T. Yates. *Surf. Sci.*, 232:113, 1990.
- [136] P. W. Anderson. *Phys. Rev. B*, 102:1008, 1956.
- [137] I.V. Shvets, G. Mariotto, K. Jordan, N. Berdunov, R. Kantor, and S. Murphy. *Phys. Rev B*. Submitted.

- [138] G. Mariotto, S.F. Ceballos, S. Murphy, N. Berdunov, C. Seoighe, and I. V. Shvets. *Phys. Rev. B*, 70:035417, 2004.
- [139] 2700 Rydin Road, Unit D, Richmond, CA 94804, USA.
- [140] OSPrey Plasma Source. Oxford Scientific, UK.
- [141] A. P. Sutton and R. W. Balluffi. *Interfaces in Crystalline Materials*. Oxford University Press, 1996.
- [142] WebElements Mark Winter. <http://www.webelements.com>.
- [143] David R. Lide. *Handbook of Chemistry and Physics*. CRC, 82 edition, 2002.
- [144] P.M. Hill, H. S. Peiser, and J. R. Rait. *Acta Cryst.*, 9:981, 1956.
- [145] O. Warren and P. Thiel. *J. Chem. Phys.*, 100:659, 1994.
- [146] A. Barbieri, W. Weiss, M. V. Hove, and G. Somorjai. *Surf. Sci.*, 302:259, 1994.
- [147] Q. Guo and P. Moeller. *Surf. Sci.*, 340:L999, 1995.
- [148] S.F. Ceballos, N. Berdunov, K. Jordan, G. Mariotto, S. Murphy, and I.V. Shvets. In preparation.
- [149] L.E. Davis, N.C. MacDonald, P.W. Palmberg, G.E. Riach, and R.E. Weber. *Handbook of Auger Electron Spectroscopy*. Physical Electronic Industries, Minnesota, second edition, 1976.
- [150] A. Wander, F. Schedin, P. Steadman, A. Norris, R. McGrath, T.S. Turner, G. Thornton, and N. M. Harrison. *Phys. Rev. Lett.*, 86:3811, 2001.